# RESOURCE ALLOCATION AND PERFORMANCE OPTIMIZATION IN ROF-BASED FIBER-WIRELESS ACCESS NETWORKS

A Dissertation
Presented to
The Academic Faculty

By

Shuyi Shen

In Partial Fulfillment
of the Requirements for the Degree
Doctor of Philosophy in the
School of Electrical and Computer Engineering

Georgia Institute of Technology

May 2021

**RESOURCE ALLOCATION AND PERFORMANCE OPTIMIZATION IN**

**ROF-BASED FIBER-WIRELESS ACCESS NETWORKS**

Approved by:


Dr. Matthieu R. Bloch
School of Electrical and Computer Engineering
*Georgia Institute of Technology*

Dr. Douglas M. Blough
School of Electrical and Computer Engineering
*Georgia Institute of Technology*

Dr. Mary Ann Weitnauer
School of Electrical and Computer Engineering
*Georgia Institute of Technology*

Dr. Shiwen Mao
Department of Electrical and Computer Engineering
*Auburn University*

Dr. John R. Barry
School of Electrical and Computer Engineering
*Georgia Institute of Technology*


Date Approved: April 21, 2021

*To my family and friends*.

# ACKNOWLEDGEMENTS

I re-discovered myself in the Ph.D. odyssey and found what I fear most is fear itself. I would like to take this opportunity to express my gratitude to those who made this dissertation possible with their help and encouragement.

I would like to thank my advisor, Prof. Gee-Kung Chang, who has mentored and inspired me with his exceptional intellectual scope, research acumen, and uncompromising effort for excellence. It is his continuous guidance, patience, and extraordinary thoughtfulness that kept my Ph.D. study on the right track. Beyond research and academics, his enthusiasm and energy in both research and life will always be motivational to me in the future. It is my greatest honor and pleasure to work with him as his student.

The next thank goes to my dissertation committee members. I would like to thank Prof. John Barry and Prof. Matthieu Bloch for giving the best digital communication and coding theory lectures which laid a solid foundation for my research. I would like to thank Prof. Matthieu Bloch, Prof. Mary Ann Weitnauer, Prof. John Barry, Prof. Douglas Blough, and Prof. Shiwen Mao for serving on my dissertation committee and providing valuable feedback that greatly improved the quality of this work.

I would like to thank Dr. Jun Shan Wey for mentoring and inspiring me as an exemplary women researcher. I would like to thank Dr. Junwen Zhang for helping me establish my first optical experimental testbed and being an instructive post-doc mentor. I would like to thank Dr. Steve Jia, Dr. Bernardo A. Huberman, Jeffrey Finkelstein for their inspiration and all the opportunities that they have made possible in my research and career.

I am appreciative to the colleagues and staff in the FiWIN research group, for being supportive teammates and friends. Thanks to Dr. Daniel Guidotti, Dr. Jhih-Heng Yan, Dr. You-Wei Chen, Dr. Chin-Wei Hsu, Dr. Jing Wang, Dr. Lin Cheng, Dr. Mu Xu, Dr. Feng Lu, Yahya M. Alfadhli, Qi Zhou, Shuang Yao, Rui Zhang, Shang-Jen Su, Muhammad S. Omar, Patricia A. Dixon, Raquel Plaskett, Angel Greenwood, as well as many other graduate students, visiting scholars, and staff members.

Lastly, I would like to thank my family and friends for all their love, encouragement, and support. Most importantly, thanks to my parents for their unconditional love and support, they taught me love and persistence, without which I could not survive the Ph.D. journey.

# TABLE OF CONTENTS

# LIST OF TABLES

# LIST OF FIGURES

# LIST OF SYMBOLS AND ABBREVIATIONS

| | |
|---|---|
| 3GPP | 3rd Generation Partnership Project |
| 5G NR | The fifth-generation New Radio |
| AI | Artificial intelligence |
| ANN | Artificial neural network |
| APD | Avalanche photodiode |
| AR | Augmented reality |
| A-RoF/D-RoF | Analog/Digital radio over fiber |
| AWGN | Additive white *Gaussian* noise |
| BER | Bit-error rate |
| CA | Carrier aggregation |
| CAPEX | Capital expenditures |
| CD | Chromatic dispersion |
| CFO | Carrier frequency offset |
| CM | Cable modem |
| CMTS | Cable modem termination system |
| CO | Central office |
| CP | Cyclic prefix |
| COMBO | The European Union project on the convergence of fixed and mobile broadband access networks |
| CU | Central unit |
| CW | Continuous wave |
| DC | Direct current |
| DFT | Discrete Fourier transform |

| | |
|---|---|
| DML | Direct modulated laser |
| DOCSIS | Data-over-Cable Service Interface Specification |
| DRL | Deep reinforcement learning |
| DSB | Double sideband |
| DSF | Dispersion shifted fiber |
| DSP | Digital signal processing |
| DU | Distributed unit |
| ECL | External-cavity laser |
| ED | Envelope detector ED |
| EDFA | Erbium doped fiber amplifier |
| eMBB | Enhanced mobile broadband |
| E-PON | Ethernet passive optical network |
| FBMC | Filter bank multi-carrier |
| FDM | Frequency division multiplexing |
| FEC | Forward error correction |
| FFT | Fast-Fourier transform |
| FH I/II | Fronthaul I/II |
| FTTC/B/H | Fiber to the curb/building/home |
| GFDM | Generalized frequency division multiplexing |
| G-PON | Gigabit-capable passive optical network |
| HA | Horn antenna |
| HARQ | Hybrid automatic repeat request |
| HFC | Hybrid fiber-coaxial |
| HPF | High pass filter |
| ICI | Inter-carrier interference |

| | |
|---|---|
| i.i.d | Independent and identically distributed |
| IM-DD | Intensity modulation and direct detection |
| IoT | Internet of things |
| IP | Internet protocol |
| ITU | International Telecommunication Union |
| LDPC | Low density parity check |
| LO | Local oscillator |
| LTE | Long-Term Evolution (4G) |
| MAC | Media access control layer |
| ML | Machine learning |
| MMSE | Minimum mean square error |
| mMTC | Massive machine-type communication |
| mmWave | Millimeter wave |
| MPA | Message passing algorithm |
| MZM | Mach-Zehnder modulator |
| NG-EPON | Next-generation Ethernet passive optical network |
| NOMA | Non-orthogonal multiple access |
| OBE | Out-of-band energy minimization |
| OC | Optical coupler |
| OCDM | Optical code division multiple access |
| OCS | Optical carrier suppression |
| OFC | Optical frequency comb |
| OFDM | Orthogonal frequency division multiplexing |
| OMA | Orthogonal multiple access |
| OOK | On-off keying |

| | |
|---|---|
| OSSB | Optical single sideband |
| PA | Power amplifier |
| PAM | Pulse amplitude modulation |
| PAPR | Peak-to-average-power ratio |
| PBC | Polarization beam combiner |
| PC | Polarization controller |
| PD | Photodetector |
| PDM | Polarization division multiplexing |
| PDMA | Pattern division multiple access |
| PD-NOMA | Power-domain non-orthogonal multiple access |
| PH | Photonic heterodyne |
| PHY | Physical layer |
| PIC | Parallel interference cancellation |
| PON | Passive optical network |
| PSD | Power spectral density |
| QoS | Quality of service |
| QPSK | Quadrature phase shift keying |
| RAN | Radio access network |
| RE | Resource element |
| ROP | Received optical power |
| RP | Roll-off period |
| RRM | Radio resource management |
| RRU | Remote radio unit |
| RTT | Round trip time |
| SC-QAM | Single-carrier quadrature amplitude modulation |

| | |
|---|---|
| SIC | Successive interference cancellation |
| SIR | Signal-to-interference and ratio |
| SMF | Single-mode fiber |
| SNR | Signal-to-noise ratio |
| SSBI | Signal-signal beating interference |
| SVM | Support vector machine |
| TDM | Time division multiplexing |
| TFL | Time-frequency localization |
| TIA | Transimpedance amplifier |
| TTI | Transmission time interval |
| TWDM-PON | Time- and wavelength-division multiplexed passive optical network |
| UAG | Universal access gateway |
| UFMC | Universal filtered multi-carrier |
| urLLC | Ultra-reliable low latency communications |
| VR | Virtual reality |
| WDM | Wavelength division multiplexing |
| WOLA | Weighted overlap and add |
| ZF | Zero forcing |

# SUMMARY

Wireless and wireline networks provide ubiquitous communication coverage for life and work in modern society. With the high growth rate of mobile traffic, radio access networks (RAN) supporting high capacity, low latency, robust transmission, and massive connections are anticipated. Advanced RANs are largely enabled by the optical networks behind, which provide high-bandwidth and low-loss transmission. Particularly, in the fifth-generation New Radio (5G NR) of mobile networking, new spectrum resources such as millimeter wave (mmWave) bands are adopted to expand bandwidth. Hence, advanced technologies such as radio-over-fiber (RoF), photonic-assisted generation techniques are intensively studied for the implementation of mmWave in the fiber-wireless access networks. For fixed access networks, operators have built and deployed fixed fiber and cable networks everywhere to service broadband residential and commercial customers, providing in-place fiber infrastructure and last-mile connections to the customers.

Radio and fixed access networks have evolved independently from one another with different topologies and protocols, whereas fundamental technologies such as transmission formats are shared across the two systems. Both radio and fixed access networks are facing challenges such as achieving higher capacity and lower latency. On the one hand, to maximize resource utilization, fixed-mobile convergence is desirable, which aims to utilize the existing fixed fiber resources as mobile x-haul for ubiquitous coverage of next-generation mobile services. On the other hand, to improve performance, fiber-wireless integrated networks are in needs of advanced access technologies and improved resource management.

The objective of the dissertation is to study and demonstrate RoF-based access technologies to improve the system performance of fiber-wireless networks. RoF-based wireless overlay over fixed access networks, advanced waveforms and multiple access schemes, and intelligent scheduling of fiber-wireless networks are the three key topics of the dissertation. Advanced RoF technologies and systems will be investigated and implemented in the dissertation. Furthermore, considering the importance of mmWave in future fiber-wireless networks, photonic-assisted mmWave generation schemes will be extensively utilized for the demonstration and verification of the systems proposed. The dissertation will cover approaches and resources including 1) infrastructure components such as fiber networks, interface equipment, etc.; 2) spectrum resources such as mmWave frequencies, spectrum-efficient waveforms and digital signal processing (DSP), advance access schemes and multiplexing methods; 3) intelligent scheduling and resource allocation using artificial intelligence (AI) technologies.

In the dissertation, we will cover networks including RANs, hybrid fiber-coaxial (HFC), and passive optical networks (PON). The architectures, key features, DSP technologies will be introduced and explained. Major in-place fiber infrastructure and last-mile wireline connections to the customers are primarily owned by fixed access networks. While in the urban area, it is expected that 5G should have ubiquitous coverage and hence requires densified cell deployment. The challenge is that the cost can be prohibitive to roll out the fiber plant required for dense cell deployment. The goals of facilitating next-generation RAN deployment and maximizing the capability of fixed networks have raised the incentives to re-use the existing fixed fiber resources for future RANs, achieving fixed-mobile convergence. In the dissertation, two schemes to provide RoF-supported wireless

overlay over fixed networks are proposed and demonstrated. Based on photonic-assisted mmWave generation schemes, the two schemes tackle the problem by exploiting two resource dimensions that were previously left unused to provide wireless overlay: one scheme is to utilize the previously idle local oscillator (LO) laser via frequency division multiplexing (FDM), the other scheme utilizes the additional orthogonal optical polarization, achieving polarization division multiplexing (PDM) with polarization-tracking-free operation. In both works, we demonstrate co-delivery of fixed and mobile services using the proposed architectures with minimum alteration to the existing networks. Comprehensive interference analysis is also studied theoretically and experimentally. Both schemes can provide potential solutions for enhancing fiber and spectrum utilization, achieving fixed-mobile convergence.

Radio and fixed access networks are facing the challenge to support data-demanding users and latency-sensitive traffic with limited infrastructure and bandwidth. In response to the challenges, topics including carrier aggregation, interference control, new waveforms, advanced decoding algorithms have drawn much attention from both sides. Two orthogonal frequency-division multiplexing (OFDM) based access schemes will be analyzed and demonstrated: windowed OFDM and pattern division multiplexing access (PDMA). Windowed OFDM is theoretically and experimentally compared with other OFDM-based waveforms in terms of spectrum efficiency and DSP complexity improvements, etc. It is demonstrated and evaluated in both mmWave wireless access and long-range optical transmission. We show that windowed OFDM can provide suppressed out-of-band leakage and improved carrier-frequency-offset resistance by applying low-complexity short perfect reconstruction windows, enabling spectrum-efficient carrier-

aggregation. Whereas PDMA is a symbol-level non-orthogonal multiple access (NOMA) scheme. For enhanced receiver-side decoding, a modified message passing algorithm (MPA) is developed and implemented for PDMA. A PDMA system integrated with MPA is experimentally demonstrated in a multi-user mmWave radio access system that uses RoF mobile fronthaul, showing improved decoding performance compared to conventional NOMA schemes. The application of PDMA in grant-free low-latency uplink access is also studied and experimentally verified.

The RANs in 5G NR and beyond are envisioned to be service-oriented, supporting multiple users and various applications with different quality-of-service (QoS) requirements. In addition to the capacity and speed requirements, latency becomes an important performance benchmark, especially for time-sensitive data traffic. To envision next-generation fiber-wireless access networks, it is desirable to integrate AI technologies into system design. We propose and evaluate a deep reinforcement learning (DRL) based scheduler operating with both latency and channel condition awareness for service-oriented multi-user mmWave RANs. The DRL scheduler is verified using experimentally collected RoF-mmWave channel conditions and variations, as well as the implementation of service flows with different QoS requirements. The DRL scheduler can operate adaptively with channel variations and jointly optimize bit error rate and latency performance. The proposed DRL-based scheduling and resource allocation is demonstrated as a promising AI-based technique that is applicable to post-5G RANs.

# CHAPTER 1 INTRODUCTION AND BACKGROUND

## 1.1 Motivation

Ever since the groundbreaking publication of Claude Shannon's paper on information theory [1], human civilization has entered a rapidly developing stage substantiated by the revolution of communication efficiency and reliability. Alexander G. Bell invented the first commercial wireline telephone services in the 1870s and created the first telephone company, the Bell Telephone Company, which later evolved into American Telephone & Telegraph (AT&T) and is still one of the world's largest phone companies nowadays [2]. Later, together with the advances in semiconductor technology, wireless and digital communications became the key innovation thrusts in the information revolution in the 1990s. Ever since then, wireless and wireline communications exist in every corner of people's daily lives and work. When we are commuting or traveling, we rely on navigation applications enabled by cellular mobile networks. At work, broadband wireline networks such as optical networks or hybrid fiber-coaxial (HFC) provide high-speed and reliable wireline communication among different entities. In the year 2020 to 2021, we are trapped at home due to the coronavirus disease 2019 (COVID-19) pandemic. For most of us living in the United States, the connections to the outside world rely on the small cable modems tapped from HFC networks. We can enjoy our safe but limited 'freedom' of walking around the apartment while watching news through mobile phones connected to Wi-Fi.

Radio and fixed access networks play important yet different roles in modern communications. According to Cisco visual networking index forecast [3], global Internet Protocol (IP) traffic will increase at a compound annual growth rate of 26% from 2017 to

2022, in which fixed traffic will grow at 24% and mobile traffic grows at 46%. By 2022, wired devices will account for 29% of IP traffic and Wi-Fi and mobile devices will account for 71%, as shown in Figure 1.1. With the nearly doubled growth rate of mobile traffic compared to fixed traffic, high-performance radio access networks (RANs) supporting high capacity, low latency, robust transmission, and massive connections are anticipated. Advanced RANs are largely enabled by the optical networks behind which provide high bandwidth and low-loss transmission. Particularly, in the fifth-generation New Radio (5G NR) of mobile networking, new spectrum resources such as millimeter wave (mmWave) bands are adopted to expand bandwidth. Hence, advanced technologies such as radio-over-fiber (RoF), photonic-assisted mmWave generation techniques are intensively studied for the implementation of mmWave in the fiber-wireless access networks. Architecture-wise, rapidly increasing traffic volumes are driving the deployment of small cell, which incurs economical pressure for 5G fiber infrastructure rollout. On the other hand, fixed access networks have built and deployed HFC networks everywhere to service broadband residential and commercial customers, providing in-place fiber infrastructure and last-mile connections to the customers. Moreover, technologies such as fiber-deep are employed in fixed access networks to extend the fiber penetration and coverage. To maximize fiber

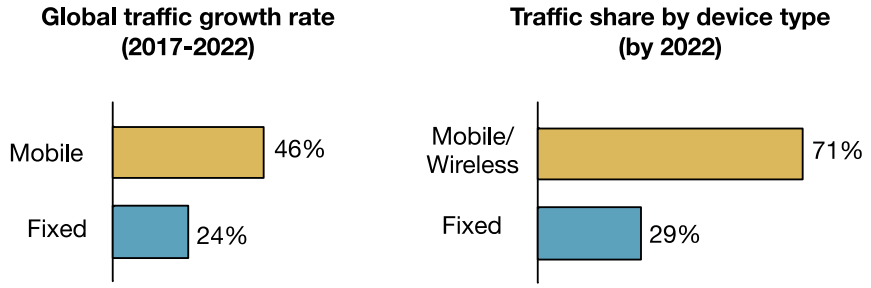


Figure 1.1 Forecast and trends of radio and fixed access networks, 2017 - 2022 [3].

resource utilization, it is desirable to exploit the potential to support mobile services utilizing the existing fixed access networks.

Radio and fixed access networks have evolved independently from one another with different topologies and protocols, whereas fundamental physical (PHY) layer technologies such as digital transmission formats and waveforms are still shared across the two systems. In practice, fixed access networks such as passive optical networks (PON) and HFC have high peak data rates but relatively low average data rates, with extensively deployed fiber infrastructure to support large number of users. Digital transmission formats such as on-off keying (OOK) and pulse amplitude modulation (PAM) are used for the transport in fixed access networks. For RANs, fiber connections between central units (CUs) and distributed units (DUs) are not as dense as fixed networks but require low latency and constant high sustainable data rates [4]. An example would be common public radio interface (CPRI) deployed as the digital mobile fronthaul. Advances of access technologies are also progressing concurrently in both fixed and radio access networks. Orthogonal frequency-division multiplexing (OFDM) has been implemented in mobile networks, Wi-Fi, HFC, etc. OFDM-based waveforms with enhanced performance have been intensively investigated for the next-generation mobile networks in the past few years. Therefore, it is essential to study advanced waveforms and multiple access schemes for performance enhancement of RoF-based fiber-wireless access networks.

In the past few years, the investigation and discussions of latency-related topics has drawn much attention, in addition to the capacity and speed that people used to primarily focus on. As a huge number of customers are increasingly using data-demanding and latency-sensitive applications across platforms, both the radio and fixed networks are

facing the challenges of achieving low latency. More and more stringent latency requirements can be observed in both networks. For example, in 4G Long-Term Evolution (LTE), the latency is around ~20ms for uplink transmission [5], whereas the 5G user-plane latency requirement is much shortened, which is 4ms for broadband traffic and 1ms for time-sensitive traffic [6]. On the other hand, operations such as priority queue is proposed in HFC to improve system latency, due to the latency requirement of various applications and the expectation for HFC to serve as mobile x-haul [5], [7]. In addition, to realize service-oriented networks which support multiple users and various applications with different quality-of-service (QoS) requirements, efficient scheduling and resource allocation algorithms are desired in fiber-wireless networks [8].

To envision for next-generation fiber-wireless access networks, integrating artificial intelligence (AI) into system design has drawn great interest from both academia and industry. From the aspects of signal processing, machine learning (ML) methods such as support vector machine (SVM) and artificial neural network (ANN) are employed in the demodulation and decoding process to supplement conventional digital signal processing (DSP) algorithms [9], [10]. AI-based technologies can also find broad applications in system resource management. In [11], SARSA reinforcement learning (RL) is utilized to realize proactive interference avoidance in a mmWave-over-fiber mobile fronthaul. In [12] and [13], deep reinforcement learning (DRL) is employed for intelligent resource block (RB) allocation in a mobile backhaul. In these systems, resource allocation and optimization that costs complex computation in conventional systems can be improved using AI-based schemes. In fact, AI is one of the key words in the vision of 6G technologies [14]. Investigation and implementation of AI technologies will thus be an important topic

of the dissertation, with a particular focus on improving scheduling and resource allocation efficiency via DRL technologies.

The objective of the dissertation is to study and demonstrate RoF-based access technologies to improve the system performance of fiber-wireless networks. RoF-based wireless overlay over fixed access networks, advanced waveforms and multiple access schemes, and intelligent scheduling of fiber-wireless networks are the three key topics of the dissertation. Motivated by the aforementioned technologies, the dissertation will cover approaches and resources including 1). Infrastructure components such as fiber networks, interface equipment, etc.; 2) spectrum resources such as mmWave frequencies, spectral-efficient DSP, interference cancellation technologies, etc.; 3) advance access schemes such as new waveforms and multiplexing methods; 4) intelligent scheduling and resource allocation based on DRL.

## 1.2 Background and Challenges

### *1.2.1 Overview of Fiber-Wireless Networks and Fixed-Mobile Convergence*

In the dissertation, three types of access networks will be discussed: radio access networks (RAN), hybrid fiber-coaxial (HFC), and passive optical networks (PON). In the section, the architecture and key features of the networks will be introduced and explained. The similarities and differences of their DSP technologies will also be elaborated and compared.

As shown in Figure 1.2, the fiber mobile fronthaul of RAN consists of central units (CUs), distributed units (DUs), and the optical to radio frequency (RF) conversion is

achieved in remote radio units (RRUs). The architecture is defined in Next-Generation Fronthaul Interfaces (NGFI) [15], [16]. Based on NGFI architecture, the concept of functional split is proposed for 5G, where the originally centralized DSP function blocks are distributed across CUs, DUs and RRUs [17]. There are various optical transmission schemes for the interface between CUs, DUs and RRUs. On the one hand, digital RoF (D-RoF) such as CPRI has been widely implemented for the mobile fronthaul in RANs [18]. In D-RoF, the output waveforms are digitized and re-synthesized using digital modulation formats for fiber transmission and will be decoded at the receiver. On the other hand, analog-RoF (A-RoF) is widely investigated as it can provide high spectral efficiency and achieve DSP-free RRU design. In A-RoF, the RF waveforms are directly converted to the optical domain at the DUs. Hence it only requires optical-to-electrical conversion in the RRUs without involving DSP to extract the RF waveforms for later antenna transmission. Based on 3rd Generation Partnership Project (3GPP) 5G Release-16 (Rel-16), 5G RANs will support two wireless frequency bands. One is Frequency Range 1 (FR1) that includes sub-6 GHz frequency bands, the other is FR2 that includes frequency bands from 24.25GHz to 52.6GHz (mmWave bands) [19], [20]. One advantage of A-RoF is that it can support the photonic-assisted generation of mmWave, which is particularly desirable for the 5G FR2 scenarios.

Different from RANs that provide wireless access to the users, HFC and PON belong to fixed access networks, as shown in Figure 1.2. HFC is the access network deployed mainly by the cable industry. In HFC, the fiber plant is deployed between cable

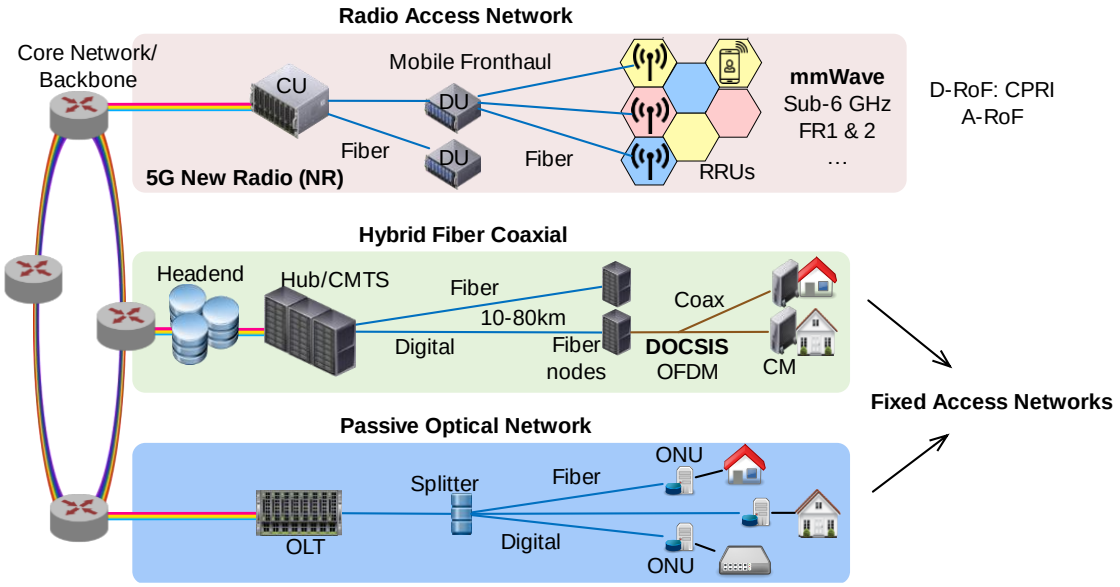


Figure 1.2 Overview of access networks: RAN for mobile networks, HFC and PON for fixed access networks.

modem termination system (CMTS) and fiber nodes in the field. In legacy generations of HFC, RF-over-glass (RFoG) which is one type of A-RoF technologies is used over the HFC fiber networks. RFoG is subject to issues such as increased noise floor due to optical beating interference and stringent requirements of linear amplifiers. Therefore, digital fiber connection is proposed and implemented for the latest generation of HFC. The concept of digital fiber belongs to D-RoF, in which modulation formats such as OOK and PAM can be utilized. After fiber transmission at the fiber nodes, RF signals are generated following the Data Over Cable Service Interface Specification (DOCSIS) and to be received by cable modems (CMs). Since DOCSIS 3.1, OFDM has become the modulation format for cable transmission [21]. Different from the hybrid networks of HFC, PONs are all-optical networks. From the optical line terminal (OLT) to the optical network unit (ONU), digital transmission formats are utilized. For the multiplexing schemes, there are time-division

multiplexing (TDM), frequency-division multiplexing (FDM), and wavelength-division multiplexing (WDM), etc.

As shown in Figure 1.2, there is wireline connection between the user-end and a remote node in both HFC and PON. While in RAN, users access the network through wireless links. In fact, major in-place fiber infrastructure and last-mile wireline connections to the customers are owned by fixed access networks. Reports show that HFC are the most widely deployed networks in North America and Europe. For example, HFC passes 93% of households in the United States [22]. Moreover, recently both HFC and PON are actively re-structuring and upgrading the fiber plants to achieve densified coverage and penetrate further out towards the end-users. In HFC, the idea of fiber deep is proposed, which is to split fiber nodes and pull fiber closer to the customer premises. In PON, fiber to the curb/building/home (FTTC/B/H) are also intensively investigated to achieve denser user coverage.

With the completion of the 5G standalone specification (3GPP Release 15 and 16), a lot of research attentions go to the study of the suitable infrastructure for 5G RANs. In the urban area, it is expected that 5G should provide ubiquitous coverage and hence requires densified cell deployment. The challenge is that the cost can be prohibitive to roll out the fiber plant required by the dense cell deployment [5]. The current trend in fixed access networks is to penetrate further out towards the end-users, such as fiber deep in HFC and FTTC/B/H in PON. The goals of facilitating next-generation RAN deployment and maximizing the capability of fixed networks have raised the incentives to re-use the existing fixed fiber resources for future RANs, namely, to achieve fixed-mobile convergence.

Many attempts have been made to drive fixed-mobile convergence. In the architectural recommendation reported by COMBO, the European Union project on the convergence of fixed and mobile broadband access networks, concepts such as universal access gateway (UAG) are proposed for functional convergence. In COMBO, WDM-based architecture is considered as the fiber-optic solution for 5G RAN deployment, taking the stringent 5G timing and latency requirements into account [4]. In the report released by International Telecommunication Union Telecommunication Standardization Sector (ITU-T) on 5G wireless fronthaul requirements in PON context, cases of TDM-PON and WDM-PON for 5G mobile fronthaul are discussed and analyzed, with the considerations of 5G function split and scheduling coordination between fixed and mobile networks [17]. These methods are important initiatives of mobile services over fixed networks. However, on the one hand, some of them require complex scheduling interface design between two systems [5][23], on the other hand, high deployment cost has delayed the implementation of WDM-PON which is considered as the optimal solution [23], [24]. Consequently, it is desirable to find a solution to re-use the fiber infrastructure efficiently without overhauling the fixed networks and to avoid the complexity, latency, and bandwidth limitations due to the interface design.

RoF-supported wireless overlay over fixed networks enabling the co-transmission of digital and analog signals will be studied in the dissertation. As a solution for the fixed-mobile convergence to enhance fiber utilization, RoF-supported wireless overlay facilitates the photonic-assisted generation of mmWave signals which is essential for future-proof RANs. To share the fiber infrastructure, it is important to reduce the influence of the additional wireless services on fixed services. Instead of sharing the capacity, RoF-

supported wireless overlay is able to utilize previously unoccupied dimensions and idle resources, which minimizes the influence on the existing services.

### *1.2.2 mmWave in RAN and Photonic-Assisted Generation Schemes*

There are three main uses defined for 5G NR: enhanced mobile broadband (eMBB) to provide high capacity; ultra-reliable low latency communications (urLLC) for mission-critical applications with low latency and robust transmission; massive machine-type communication (mMTC) supporting tremendous connectivity and Internet of Things (IoT) [17]. mmWave frequencies providing wide bandwidth are employed in 5G RANs to support eMBB operations. In 3GPP 5G specifications, mmWave bands from 24.25GHz to 52.6GHz are selected as FR2 for 5G NR [20]. To facilitate future enhancements to NR beyond 52.6GHz, 3GPP also envisions deployment scenarios for carriers from 52.6GHz to 114.25GHz [25]. Compared to conventional frequency bands, one feature of mmWave band is the high directivity. As a result, antenna misalignment or obstacles in mmWave links can cause severe degradation, adding more channel dynamics to next-generation RANs. High Friss path loss is another feature of mmWave band. In particular, the unlicensed frequency band around 60GHz exhibits high path loss due to oxygen absorption, which makes it a key enabler for 5G small-cell deployment [26].

A conventional method to generate mmWave is through electrical generation, as shown in Figure 1.3(a). With an RF carrier operating at the mmWave frequency and a mixer, the baseband signal is upconverted to the mmWave frequency band for following amplification and wireless transmission. The electrical generation scheme has simple structure and hence it is easier for system integration. However, the cost of high-frequency

electrical devices can be prohibitive, and the system capacity can be restricted due to the limited bandwidth of electrical devices.

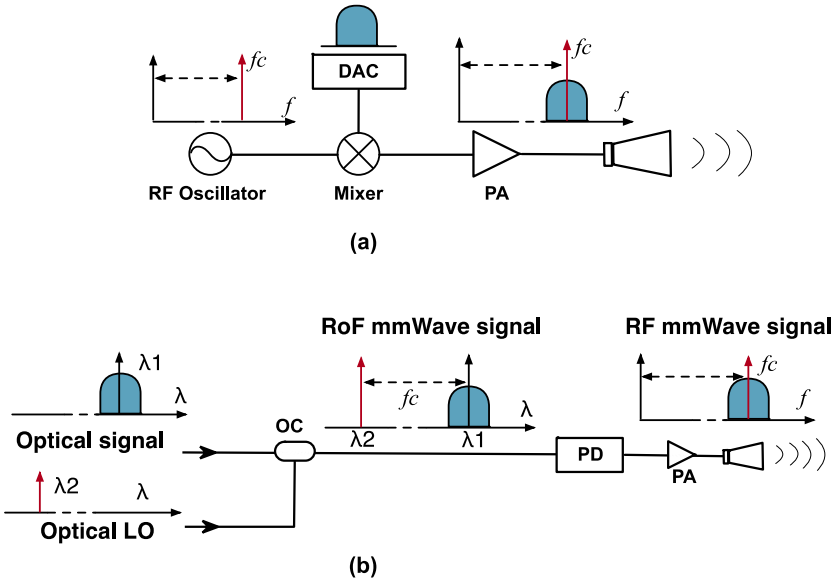


Figure 1.3 The principle of: (a) electrical generation of mmWave; (b) photonic-assisted generation. (DAC: digital to analog converter; PA: power amplifier; OC: optical coupler.)

Photonic-assisted mmWave generation schemes have been proposed and demonstrated to overcome the bottleneck of electrical-based bandwidth-limited generation schemes [27]. Figure 1.3(b) shows the principle of a typical photonic-assisted mmWave generation scheme. There will be one desired optical signal and one local oscillator (LO) at certain mmWave frequency away from each other in the transmitter (Tx) side. At the receiver (Rx) side, the two optical signals will beat with each other and a photodetector (PD) will capture the resulted RF signal at the mmWave frequency. By using optical devices, photonic-assisted mmWave generation schemes can utilize fiber infrastructure and overcome the bottleneck of electrical-based bandwidth-limited generation schemes. One challenge of the photonic-assisted scheme is network symmetry, as it requires laser sources

in the transmitter. In the uplink direction, it can be hard to integrate laser sources to compact user equipment.

The photonic-assisted mmWave generation schemes have been intensively investigated for the applications in next-generation RANs to provide ultra-high capacity. In [28] and [29], optical external modulation methods such as optical carrier suppression (OCS) and optical frequency comb (OFC) were used to realize mmWave transmission for mobile fronthaul at V-band (40-75GHz). Moving to higher frequency bands, >40 Gbps wireless transmissions at W-band (75-110GHz) have been demonstrated in [30] and [31], combining technologies including OCS, heterodyne detection techniques, and DSP in coherent optical transmissions. At D-band (110-170GHz), a record-breaking data rate of 1Tbps is achieved by photonic remote heterodyning [24].

### *1.2.3 Advanced OFDM-Based Waveforms and NOMA*

Faced with the explosive demand for data throughput and restricted by limited spectrum resources, pursuing advanced PHY technologies to improve system performance has always been one of the most important endeavors for various fiber-wireless networks. Cell densification and carrier aggregation are important approaches in 5G to boost the throughput and provide the coverage for massive devices [26]. Carrier aggregation is employed not only in 5G but also in fixed access networks such as HFC. In fact, channel bonding is one of the new features of DOCSIS 3.1 [32]. The implementation of carrier aggregation requires waveforms with high spectral efficiency and low out-of-band emission. The deployment of small cells requires the control of user interference, DSP complexity, and cost per cell [33].

Modulations with higher spectral efficiency to enhance capacity have been investigated and employed in various access networks. For optical access networks, PAM4 and OFDM are considered to replace OOK with improved spectral efficiency [34]. In DOCSIS 3.1, single-carrier quadrature amplitude modulation (SC-QAM) has been upgraded to OFDM to achieve higher spectral efficiency [32]. In 5G waveform investigation, advanced waveforms such as filter bank multi-carrier (FBMC) [35], universal filtered multi-carrier (UFMC) [36], and weighted overlap add (WOLA) [37], have been widely researched and discussed. Waveforms with high spectral efficiency and low out-of-band leakage are the key enablers for intensive carrier aggregation. FBMC and UFMC provide higher spectral efficiency with greatly improved out-of-band emission suppression but requiring much higher complexity of transmitters and receivers than conventional OFDM. On the other hand, WOLA which is advocated by Qualcomm, provides significant out-of-band leakage suppression but requires an extra roll-off period in the time domain. In the dissertation, windowed OFDM with short perfect reconstruction filters to provide high spectral efficiency and low DSP complexity will be studied as one promising next-generation waveform.

As mentioned in section 1.2.2, one important technical approach of 5G NR is to utilize the abundant bandwidth provided by mmWave bands. Considering both Friss propagation loss and atmospheric absorption loss in multi-user systems, mmWave links can exhibit dynamic channel characteristics. To achieve high capacity under such complex link conditions can be a daunting task for conventional orthogonal multiple access (OMA) systems employed in current RANs and other wireless access networks [38]. Moreover, next-generation mobile data communication is anticipated to be service-oriented

networks [8]. Use cases such as traffic safety, infrastructure protection, and industrial applications based on IoT require low latency, an increased number of connected devices, and higher access flexibility. In response to these challenges, non-orthogonal multiple access (NOMA) has been investigated for 5G and next-generation RANs to exploit under-utilized power resources and increase the number of user equipment (UE) [39], [40].

In NOMA, power is considered as the third dimension on top of the time and frequency dimensions [38], [41]-[43]. When users are experiencing disparate channels in the networks, which are common in both fixed and wireless access networks, conventional OFDM access (OFDMA) has to sacrifice spectral efficiency to serve users with low signal-to-noise ratio (SNR) with low QAM orders. To solve the issue, NOMA is considered to fully utilize channel capacity by exploiting power domain multiplexing. In 3GPP Release 16, various OFDM-based NOMA schemes are discussed and compared, including conventional power-domain NOMA (PD-NOMA), NOMA using bit-level, symbol-level, resource-mapping patterns, and codebook-based NOMA [43].

For NOMA receiver process, successive interference cancellation (SIC) is used in conventional PD-NOMA, but it is susceptible to error propagation which makes current user decoding highly dependent on precedent correctly decoded users [44]. Therefore, advanced parallel interference cancellation (PIC) for NOMA receiver is proposed and studied in the dissertation, which decodes all active users simultaneously thereby avoiding the order-related error propagation of SIC and improving decoding accuracy. Among various PIC methods, one approach is the iterative message passing (belief propagation) which is a mature decoding process that has been used in low-density parity-check (LDPC) decoders [42].

### *1.2.4 Scheduling and Resource Allocation in Fiber-Wireless Networks*

Due to emerging applications such as virtual reality (VR) and augmented reality (AR) that may require end-to-end latency as low as 1ms, fiber-wireless access networks are anticipated to upgrade and support low-latency services. Therefore, research topics regarding improvements of scheduling and resource allocation schemes are drawing more attention recently. The concepts of scheduling and resource allocation are used interchangeably in many research papers. However, strictly speaking the definition of scheduling is to assign the priority of packets or requests, whereas resource allocation is to decide the physical assignment or mapping of resource elements (REs) to users or requests. The convention of using the two terms interchangeably is also kept in the dissertation.

Generally, the downlink latency of a system is small and manageable, usually within several round-trip time (RTT). It is also easy to monitor as the scheduler always has the control of the downlink scheduling process. Whereas the challenges of achieving low latency exist in the uplink, since the arrivals of user data are stochastic. A classic uplink scheduling process is depicted in Figure 1.4. The structure of request-grant cycle is widely adopted by various radio and fixed access networks. In a PON network, the central office (CO) can be an OLT; in a HFC network, the CO can be a CMTS; in a 5G RAN, the CO can be a CU or DU, all are where a scheduler may exist. During the scheduling process, at each transmission time interval (TTI), users will firstly request transmission opportunities before actual data transmission. The scheduler will process the requests and then distribute the uplink grants. Not all requests can be satisfied especially when the traffic load is heavy, which may cost additional queuing delay. The users will then prepare and send the data packets in the allocated REs. Upon receiving the uplink packets the scheduler will check

the error rate of the received packets which determines whether re-transmission (re-tran) is required. The scheduler may send Hybrid automatic repeat request (HARQ) or NACK accordingly. The overall latency consists of several parts, for instance, the propagation delay as indicated by Figure 1.4 at point b which is primarily influenced by the transmission distance; the scheduler processing delay as indicated by Figure 1.4 at point c which can be affected by the duration of TTI ; and queuing delay as indicated by Figure 1.4 at point f, which may be impacted by traffic load; etc.

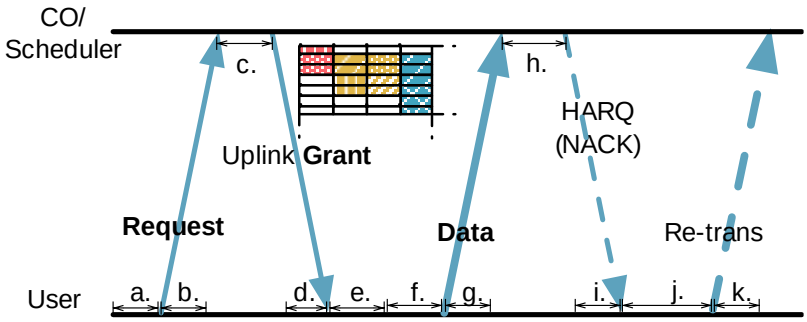


Figure 1.4 The request-grant cycle in uplink scheduling.

Many schemes and solutions are proposed to achieve low latency in various networks. Methods such as pre-scheduling and puncturing jump out of the box of the request-grant structure. In pre-scheduling, or sometimes referred to as grant-free uplinks, some REs are reserved for certain applications or requests with high priorities, so that immediate uplink transmission opportunities are available when new requests arrive. The drawback of the pre-scheduling scheme is that the pre-allocated REs may be wasted. Whereas puncturing is proposed in 3GPP proposals, which is to puncture the eMBB traffic by urLLC traffic. The scheme gives a higher priority to urLLC traffic which bypasses the request-grant mechanism. The major pitfall is that, after multiplexing, all traffic (i.e., urLLC and others) will traverse the same fronthaul without any QoS awareness [45].

Within the frame of request-grant-based scheduling, there are also several methods proposed to achieve low latency. One type of the methods is to shorten the duration of TTIs. For example, in 5G mobile networks, flexible OFDM numerologies and frame structures are standardized to reduce TTI [46]; in PON, a flex-frame architecture is proposed for gigabit-capable PON (G-PON) to reduce latency [47]. Another intensively studied area is to use AI technologies to optimize the scheduling strategy. In [48], an intelligent bandwidth allocation is proposed for next-generation Ethernet PON (NG-EPON) using reinforcement learning. In the dissertation, DRL will be utilized to optimize the scheduling process of RoF-mmWave RANs. Most of the previous DRL-related works are validated with only simulation results, whereas the DRL-based resource allocation in the dissertation will be demonstrated with experimental results, taking the advantages of the RoF-mmWave testbed implemented in the dissertation.

## 1.3 Dissertation Organization

The objective of the proposed research is to study and demonstrate RoF-based access technologies to improve the system performance of fiber-wireless networks. RoF technologies and systems will be investigated and implemented throughout the dissertation. Furthermore, considering the importance of mmWave in future fiber-wireless networks, photonic-assisted mmWave generation schemes will be extensively utilized for the demonstration and verification of the systems proposed in the dissertation. Figure 1.5 illustrates the approaches and the topics. The dissertation will mainly cover three aspects of the approaches and resources that can be leveraged in fiber-wireless networks. Firstly, there are various infrastructure components that can be utilized. The features of fiber such as lightwave wavelengths and polarizations, as well as the interface equipment such as

optical sources, local oscillators, and photodetectors, will be explored to provide extra capacity on top of the existing systems. Moreover, it will take the advantages of architecture evolutions such as fiber deep in HFC and small cell in 5G for further performance enhancement. Spectrum is another important resource to be discussed in the dissertation. As introduced in section 1.2.2 and 1.2.3, mmWave will be implemented in future-proof RANs, together with the idea of carrier aggregation, wider bandwidth and hence larger capacity will be expected, which will require interference control and advanced DSP techniques. The two aspects of infrastructure components and spectrum resources aim to optimize system performance in the PHY layer, whereas the third aspect, scheduling and resource management, targets to improve the resource allocation of fiber-wireless networks in both the PHY and media access control (MAC) layers. AI technologies such as DRL are proved to be effective in tackling real-time decision-making problems, which have made breakthroughs in the field of resource management. As

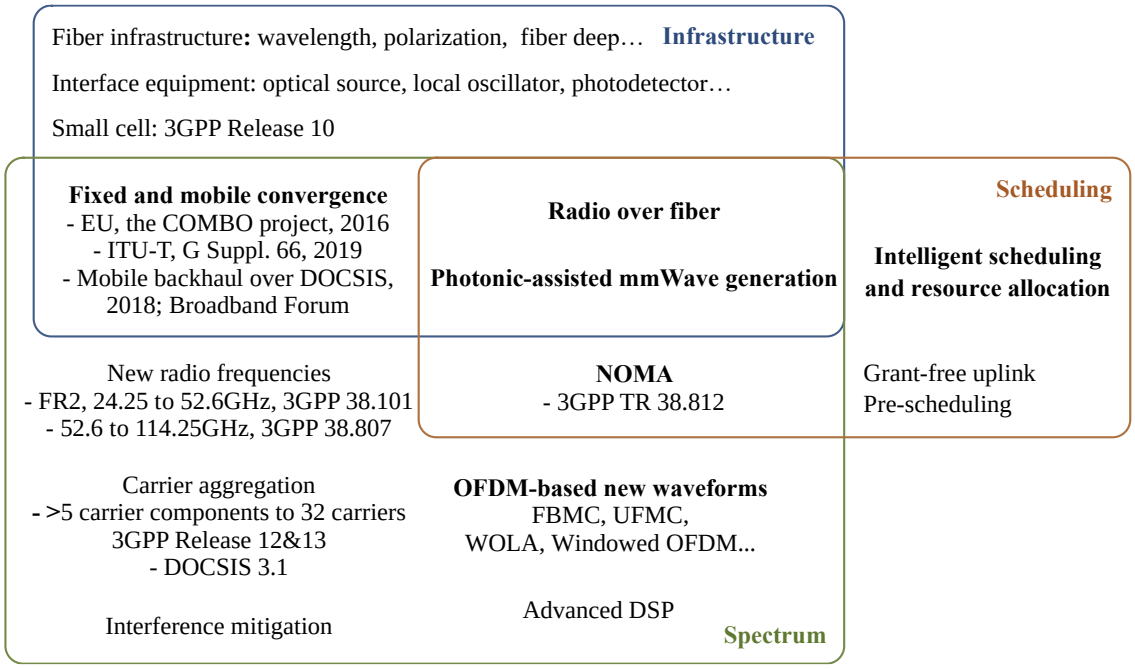


Figure 1.5 Topics covered by the dissertation.

introduced in section 1.2.4, schemes to improve scheduling efficiency such as grant-free uplinks and AI-assisted intelligent scheduling will be covered in the dissertation.

The parts highlighted in bold in Figure 1.5 are the core topics that will be presented and demonstrated. In CHAPTER 1, we have introduced the motivation and background knowledge of RoF-based fiber-wireless networks, as well as basic concepts and approaches that will be used throughout the dissertation. In CHAPTER 2, two schemes to provide RoF-supported wireless overlay over fixed networks will be demonstrated. The schemes fall into the category of fixed-mobile convergence, which will involve the two PHY aspects of infrastructure components and spectrum resources. Despite that there have been a lot of previous research on fixed-mobile convergence done by various industry communities and standard bodies (see section 1.2.1), the two schemes proposed tackle the problem by exploiting two resource dimensions that were previously left unused: one scheme is to utilize the previously idle local oscillator (LO) laser via frequency division multiplexing (FDM), the other scheme utilizes the additional orthogonal optical polarization, achieving tracking-free polarization division multiplexing (PDM). The operation principles will be presented theoretically. The gain of the wireless overlays as well as and the penalty caused by the interference will be analyzed and evaluated with experimental demonstration of RoF wireless overlays using photonic-assisted mmWave generation schemes. In CHAPTER 3, two important OFDM-based access schemes will be demonstrated: windowed OFDM and pattern division multiplexing access (PDMA). In the work of windowed OFDM, the operating principle will be introduced. It will also be compared with other OFDM-based advanced waveforms in terms of spectrum efficiency and DSP complexity improvements. The applications customized for different requirements of radio and fixed networks will be

demonstrated as well. In the work of PDMA, which is a symbol-level NOMA scheme, the mathematical principle of PDMA will be introduced. A modified message passing algorithm (MPA) is developed and implemented to enhance the decoding performance of PDMA, the principle of which is also elaborated in the chapter. For the applications, we will show that PDMA can support grant-free uplinks for low-latency services, with experimental demonstration in a multi-user mmWave radio access system using RoF mobile fronthaul. In CHAPTER 4, a channel and latency aware radio resource allocation algorithm based on DRL is proposed and evaluated for service-oriented multi-user mmWave RANs. The framework and design of the DRL algorithm, the implementation details of the component modules of the system will be illustrated. In particular, the mmWave channel and variations utilized are experimentally collected via the RoF-mmWave testbed. The evaluation of the DRL system and the performance comparison with conventional scheduling rules are also presented and analyzed. At last, we summarize the technical contributions of the dissertation in CHAPTER 5. Future research opportunities are also discussed in this chapter.

# CHAPTER 2 ROF-SUPPORTED WIRELESS OVERLAY OVER FIXED ACCESS NETWORKS

As illustrated in section 1.2.1, fixed access network is an attractive option for 5G x-haul as it is a low-cost alternative compared to pulling new fiber. RoF-supported wireless overlay over fixed networks is a solution among various schemes to achieve fixed-mobile convergence. RoF-based mobile fronthaul is able to support wireless signals at both FR1 (sub-6GHz) and FR2 (mmWave frequencies). Different from other schemes to share part of the resources (wavelengths, frequencies, time slots) with the wireless services, the proposed RoF-supported wireless overlay aims to exploit the previously unused resource dimensions of the networks. By utilizing new resource dimensions, RoF-supported wireless overlay will not occupy the capacity of the fixed services. The challenge, however, is to reduce the interference from the wireless overlay to the existing fixed services.

In this chapter, RoF-based multiplexing technologies of wireless overlay over fixed networks are presented to support the co-transmission of digital and analog signals. The digital signals are designated for fixed services which mainly uses digital modulation formats such as OOK and PAM, while the analog signals are A-RoF OFDM signals suitable for the RoF transmissions. Two resource dimensions that were previously left idle are investigated. Based on the photonic-assisted generation of mmWaves shown in Figure 1.3(b), one scheme is to modulate the previously idle local oscillator (LO) laser with digital data to realize frequency division multiplexing (FDM) for hybrid RoF transmission. This work takes the advantages of the inherent frequency difference between fixed systems and mmWave wireless systems. The other scheme is to utilize the additional orthogonal optical wireless overlay, achieving polarization division multiplexing (PDM). Polarization

tracking is a challenging issue in conventional PDM schemes. An advanced system design is proposed to bypass the polarization tracking process. Both schemes can achieve co-delivery of hybrid digital and analog signals for fixed and mobile services, providing potential solutions for enhancing fiber utilization and achieving fixed-mobile convergence.

## 2.1 W-Band/Baseband Co-Transport with Data-Carrying Remote LO

A typical architecture of PON networks is shown in Figure 2.1(a). Optical signals are generated and delivered with intensity modulation and direct detection (IM-DD), in which baseband digital signals such as OOK and PAM4 are modulated to an optical carrier then directly detected and captured by a low-frequency (< 60GHz) PD after single-mode fiber (SMF) transmission. According to widely employed stands, the PON signals usually occupy bandwidth smaller than 50GHz, such as 2.5Gbps GPON, 10 Gbps symmetrical 10G-PON, and a recent single-wavelength 50Gbps time- and wavelength-division multiplexed PON (TWDM-PON) [49]. Whereas in A-RoF mobile fronthaul, it is beneficial to provide mmWave transmission especially with photonic-assisted generation. A classic system architecture to realize mmWave wireless transmission is via photonic heterodyne (PH) detection at the receiver as shown in Figure 2.1(b), where a LO is used to beat with the optical carrier modulated by the wireless signal. For mmWave operating at V-band and W-band (> 60GHz), there is inherent system frequency difference between RoF and PON networks. For future-proof fixed-mobile convergence schemes, it is necessary to support mmWave bands, while fixed networks can use digital signals locating in baseband simultaneously.

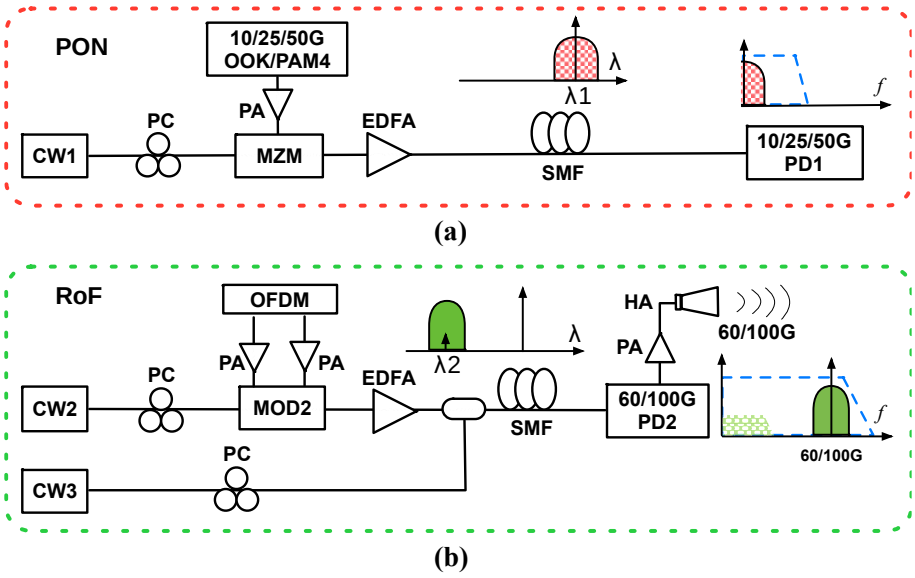


Figure 2.1 Architecture diagrams of: (a) an IM-DD PON system; (b) RoF system supporting mmWave. (CW: continuous wave; PC: polarization controller; MZM: Mach–Zehnder modulator; EDFA: Erbium doped fiber amplifier.)

In this work, an FDM-based scheme is proposed to realize the co-transmission of analog mmWave signals for mobile communications and baseband digital signals for fixed transport, by implementing a data-carrying remote LO. The system architecture is shown in Figure 2.2. Due to the inherent FDM of two streams of signals, no extra devices other

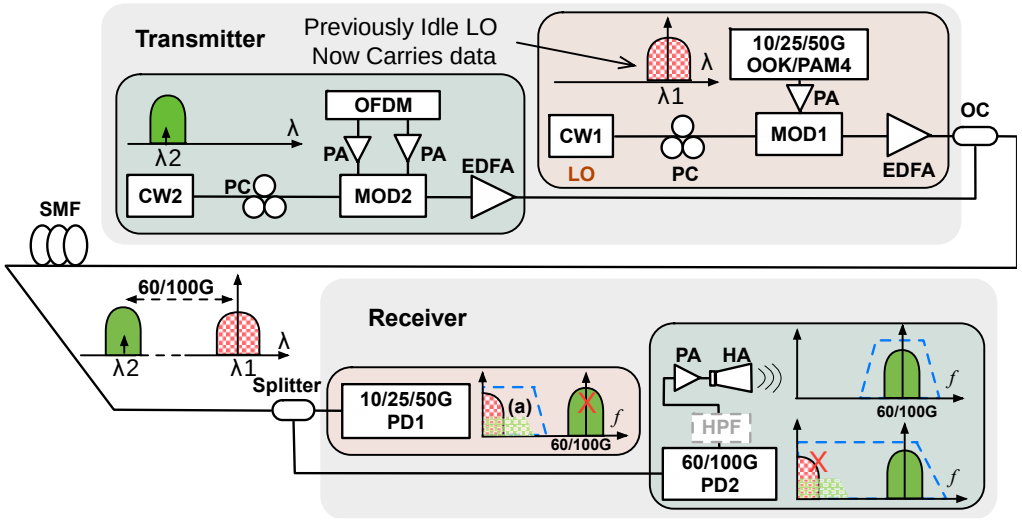


Figure 2.2 Schematic diagram of the FDM co-transmission system (MOD: modulator; OC: optical coupler.)

than an optical splitter are needed at the receiver side to separate two signals. In this work, co-delivery of net 35.39Gbps OFDM signal at 85GHz over 1m wireless distance and 10.9Gbps OOK signal over 5km standard single-mode fiber (SMF) was experimentally demonstrated. This work has been published in *Optical Fiber Conference (OFC) 2020* [50].

### *2.1.1 Operating Principles*

As shown in Figure 2.2, in the proposed architecture previously idle LO is modulated with digital signal for fixed services, becoming a remote LO. No extra devices at the receiver other than an optical splitter are needed to separate different branches. The separation of mmWave and baseband signals is achieved by the inherent frequency difference of the two systems. For the wireless branch as shown in the green receiver block in Figure 2.2, the horn antenna (HA) following PD2 has the operating bandwidth at corresponding mmWave frequencies, which serves like a high pass filter (HPF) that removes the unwanted baseband signal. As a result, the output wireless signal after the antenna contains only mmWave component that can be transmitted for next-stage wireless communications. An HPF can be applied after PD2 to improve the efficiency of the following electrical power amplifier (PA). For the fixed branch, a low-bandwidth, low-cost PD1 is utilized to convert the optical signal to the electrical domain, the same receiver structure widely used in IM-DD systems. PD1 will reject mmWave components while reserving the desired baseband signal for following transmissions in the fixed networks.

Particularly, at PD2, analog signals carried by $\lambda_2$ relies on the strong carrier component of $\lambda_1$ to achieve effective optical beating and to up-convert to the mmWave band, since the carrier component of OFDM signal is suppressed in the generation process.

Let $E_1$ and $E_2$ denote the optical intensity of $\lambda_1$ and $\lambda_2$, respectively, *m* denotes the modulation depth. The OFDM signal modulated onto $\lambda_1$ is $p(t)$ so the corresponding optical signal is $S_1(t) = E_1 e^{j\omega_1 t+\phi_1} \cdot p(t)$. For OOK signal $q(t)$, the corresponding optical signal can be expressed as $S_2(t) = (1 + mq(t))E_2 e^{j\omega_2 t+\phi_2}$. At the receiver after optical coupler (OC), the two signals will beat with other to generate the desired signals and also interference. Let $c_1 = S_1$ , and $S_2 = c_2 + c_3$ in which $c_2 = E_2 e^{j\omega_2 t+\phi_2}$ and $c_3 = mq(t)E_2 e^{j\omega_2 t+\phi_2}$. After the PD with the square law detection ($I_{PD} = \gamma|E|^2$), the resulted electrical signal can be expressed as:

$$\begin{aligned} I &= \gamma\left|S_1 + S_2\right|^2 = \gamma\left|c_1 + c_2 + c_3\right|^2 \\ &= \gamma(\left|c_1\right|^2 + \left|c_2\right|^2 + \left|c_3\right|^2 + 2Re\left\{c_1 c_2^*\right\} + 2Re\left\{c_3 c_1^*\right\} + 2Re\left\{c_2 c_3^*\right\}) \end{aligned} \quad (1)$$

In Equation (1), the term $2\,\mathrm{Re}\left\{c_1 c_2^*\right\} = 2E_1E_2\,\mathrm{Re}\{p(t)e^{j(\omega_1-\omega_2)t+\phi_1-\phi_2}\}$ is the desired signal at the mmWave band which is dependent on $E_1$ and $E_2$, while the term $2Re\left\{c_1^* c_3\right\} = mE_1E_2q(t)\,\mathrm{Re}\left\{p^*(t)e^{j(\omega_2-\omega_1)t+\phi_2-\phi_1}\right\}$ is the interference that is dependent on $E_1$, $E_2$, and *m*. Similarly, $2\,\mathrm{Re}\left\{c_2 c_3^*\right\} = 2mE_2^2q(t)\,\mathrm{Re}\left\{e^{j(\phi_2-\phi_3)}\right\}$ is the desired signal at the baseband, which is dependent on $E_2$ and *m*, while the term

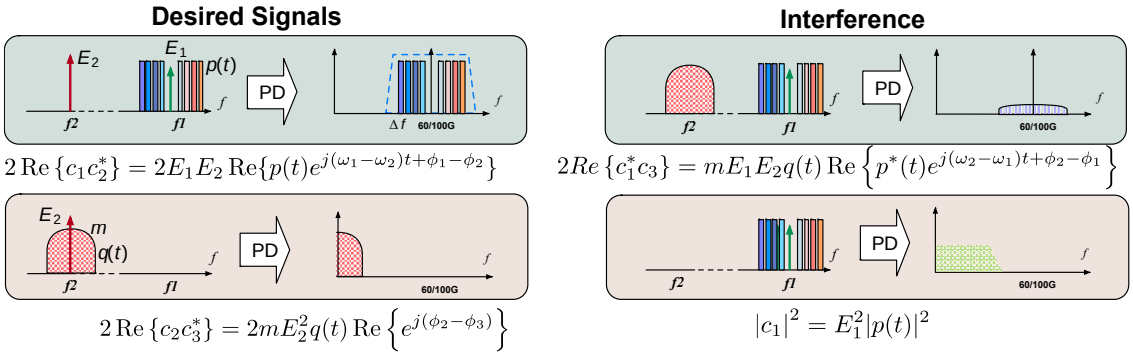


Figure 2.3 Desired signals and interference after optical beating and photodetection.

$|c_1|^2 = E_1^2|p(t)|^2$ and is the interference that is dependent on $E_1$. This is the signal-signal beating interference (SSBI) of the analog signal originally carried by $\lambda_2$, as illustrated at position (a) in Figure 2.2. The rest of the terms in Equation (1) are not taken into account as they are either just direct current (DC) component or not significant component comparatively. The process is visualized in Figure 2.3. Based on the analysis, to optimize reception of the desired signals and suppress the interference, high $E_2$ of carrier $\lambda_2$, comparatively low $E_1$, and relatively small modulation depth *m* at modulator 1 (MOD1) are preferred. The optimal operation is implemented in the demonstration.

### *2.1.2 Experimental Setup*

The experimental setup is shown in Figure 2.4, the wavelengths of two external modulated lasers (ECLs) were $\lambda_1 = 1550.47\ nm$ (ECL1) and $\lambda_2 = 1549.78\ nm$ (ECL2) for the fixed and the wireless branches, respectively, providing 85GHz W-band carrier. 12GBaud OOK signal generated by an arbitrary waveform generator (AWG, 12GSa/s, 7.5GHz 3dB bandwidth) is modulated to ECL1 via a Mach–Zehnder modulator (MZM) after electrical amplification. The MZM is biased at the quadrature point. The net rate of OOK signal is 10.9Gbps excluding training. Analog OFDM signal with net rate of 35.39Gbps is generated by another AWG with sampling rate of 63GSa/s (20GHz 3dB bandwidth) and modulated to ECL2 by an I/Q-modulator. Two arms of the I/Q modulator are biased at the null point with 90-degree phase difference. Each optical signal is amplified by an Erbium doped fiber amplifier (EDFA) and then combined by an OC for transmission over 5km SMF. The optical power of ECL1 carrying OOK signal is 15dBm, and the optical power of ECL2 carrying OFDM is 1dBm. The optical spectrum of the combined signal is shown in Figure 2.4(a).

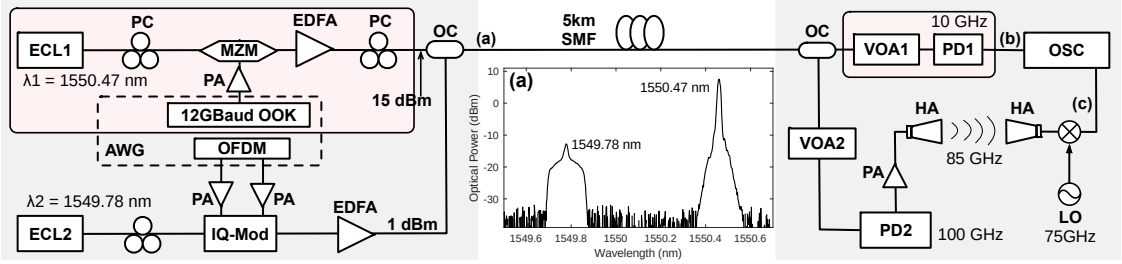


Figure 2.4 Experimental setup of the co-transmission system (Inset: the optical spectrum at position (a)). © OSA 2020.

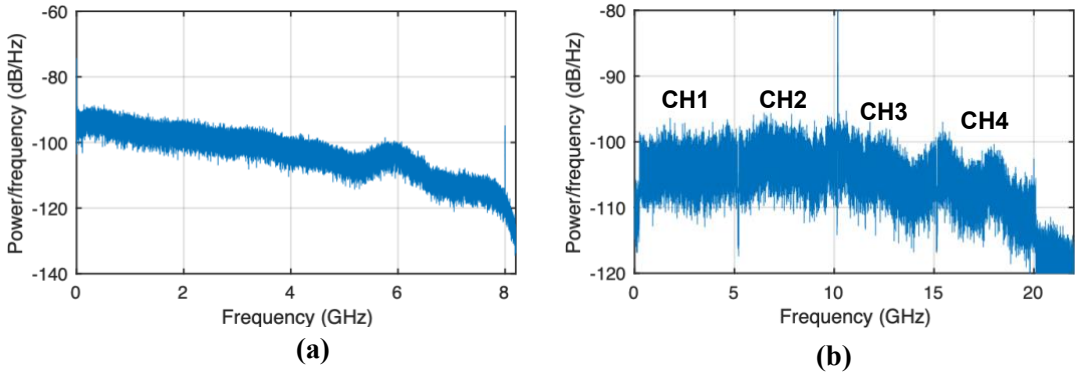


Figure 2.5 Power spectrum of (a) baseband OOK signal at position (b) in Figure 2.4. (b): W-band OFDM signal at position (c). © OSA 2020.

At the receiver, a PD1 with 10GHz bandwidth is used for OOK signal detection. Variable optical attenuators (VOA) are used to adjust the received optical power (ROP) before PD. In a real-world application, the output signal of PD1 can be used for the following fixed network transmission. For the wireless branch, a PD2 with 100GHz bandwidth is used to detect the W-band OFDM signal, followed by a PA. The OFDM signal is then transmitted and received by a pair of W-band HAs over 1m wireless distance. Before captured by an OSC (80GSa/s, 25GHz 3dB bandwidth), the W-band signal is down-converted to around 10GHz intermedia frequency by a mixer with a 75GHz electrical LO.

For the fixed branch, OOK signal is pulsed shaped by the square-root raised cosine filter with roll-off factor of 0.1, occupying 6.6GHz bandwidth. Its power spectrum is plotted in Figure 2.5(a). For the OFDM signal, four bands (CH1, 2, 3, 4) supporting

multiple users are transmitted, the subcarrier spacing is $2^{10} \times 15\ kHz = 15.36\ MHz$, the bandwidth per band is 4.9GHz, quadrature phase shift keying (QPSK) was used for each band, providing total net data rate of 35.39Gbps over 19.91GHz bandwidth. The power spectrum of the OFDM signal is shown in Figure 2.5(b).

### *2.1.3 Experimental Results and Evaluation*

Figure 2.6(a) shows the BER performance versus ROP of the RoF wireless branch in back-to-back (B2B) and over-5km SMF scenarios. Results of CH2, CH4 and overall BER are selected for illustration. Overall BER can pass the 7% hard-decision forward error correction (HD-FEC) threshold $3.8 \times 10^{-3}$ with -5dBm sensitivity. Similarly, Figure 2.6(b) show the BER performance versus ROP of the fixed branch delivering the OOK signal. Experimental results show -13dBm sensitivity at FEC threshold with the given experimental setup and devices.

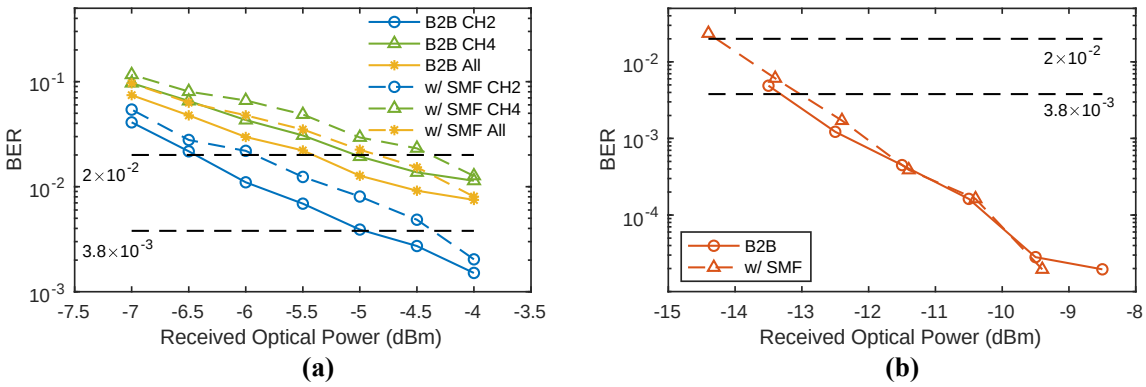


Figure 2.6 BER versus ROP for (a) OFDM signal; (b) OOK baseband signal in B2B and over-SMF scenarios. © OSA 2020.

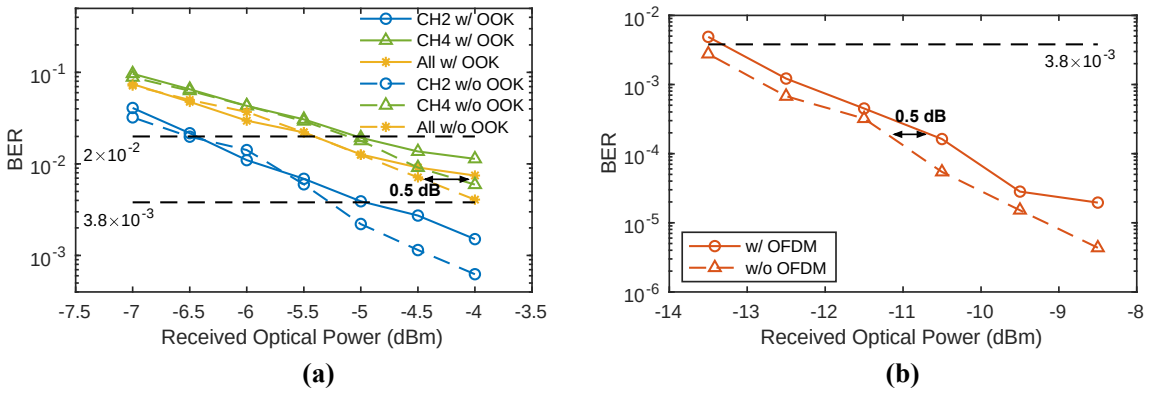


Figure 2.7 BER versus ROP for (a) OFDM signal with and without OOK signal; (b) OOK signal with and without OFDM signal. © OSA 2020.

Figure 2.7(a) demonstrates the BER performance vs ROP of the wireless branch with and without interference from the fixed branch. During the measurement, the output of the AWG generating OOK signal is switched off for the interference-free case. Similar results are found for the fixed branch. 0.5dB penalty from the wireless branch is measured as shown in Figure 2.7(b).

The variation of the BER performance with respect to the optical power fluctuation of the other branch is also investigated for both OFDM and OOK signals. As shown in Figure 2.8(a), overall BER of the W-band OFDM signal degrades from $5.9 \times 10^{-3}$ to $1.7 \times 10^{-2}$ as the optical power of OOK carrier decreased from 16.3dBm to 11.8dBm (over a range of 5.5dB), due to decreasing LO power available to the OFDM signal for upconversion. While for the baseband OOK signal, BER degraded from $2.17 \times 10^{-6}$ to $3.8 \times 10^{-3}$ as the optical power of the OFDM signal increases from 2dBm to 8dBm (over a range of 6 dB). As analyzed in section 2.1.1, the fixed branch is primarily influenced by the SSBI of the OFDM signal which increases with its optical power. Overall, both branches are able to tolerate optical power fluctuation of the other branch over a range of at least 5.5dB.

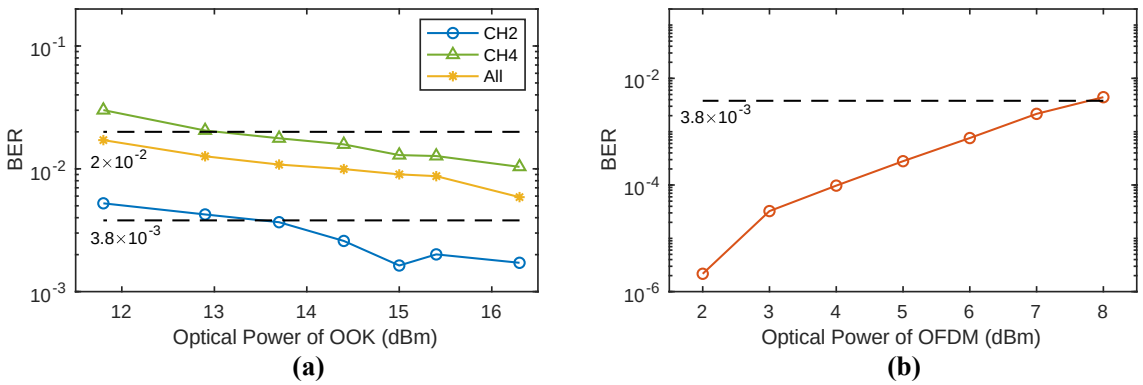


Figure 2.8 BER variation: (a) OFDM signal with varied optical power of OOK signal; (b) OOK signal with varied optical power of OFDM signal. © OSA 2020.

### *2.1.4 Summary*

By modulating digital baseband signal to the previously idle LO, the proposed architecture can enable hybrid transmission of the mmWave wireless signal and the baseband digital signal. Due to the inherent FDM of two signals, no extra devices other than an optical splitter are needed at the receiver side to separate two signals. In this work, co-delivery of 35.39Gbps W-band OFDM signal at 85GHz over 1m wireless distance and 10.9Gbps OOK signal over 5km SMF was experimentally demonstrated. For both fixed and mobile transmissions, the sensitivity penalty caused by the interference from the other branch is as low as 0.5dB. Both branches are able to tolerate optical power fluctuation of the other branch over a range of at least 5.5dB with BER below FEC threshold.

## 2.2 Polarization-Tracking-Free PDM

In order to facilitate 5G deployment and maximize the capability of fixed networks, it is desirable to achieve efficient unification of the fixed and mobile network [51], [52]. Many attempts have been made to drive fixed-mobile convergence. One of the main challenges for HFC-mobile convergence is the latency limitation based on DOCSIS in the

HFC network. In 2018, CableLabs and Cisco have demonstrated low-latency LTE over DOCSIS using commercial platforms [5]. These methods are important initiatives of mobile service over fixed networks, but most of them require interface design between two systems. Consequently, sharing the fiber infrastructure as well as delivering fixed and mobile services independently becomes a desirable solution to avoid the complexity, latency, and bandwidth limitations in the interface design. The scheme studied in the section is to utilize the orthogonal polarization, which potentially doubles the spectral efficiency. In conventional PDM, polarization-orthogonal lightwaves, polarization-tracking techniques and DSP are required for successful demodulation, most of which are complicated and impractical for fixed access networks.

In this section, a polarization-tracking-free PDM is proposed to overlay 5G over fixed fiber networks for fixed-mobile convergence, as shown in Figure 2.9. The work has been published in *Photonics Technology Letters* [53]. The polarization-tracking-free PDM demultiplexing is achieved by removing the optical carrier of the opposite polarization through an optical filter instead of complicated DSP. This convergence system based on the proposed PDM scheme requires the same communication spectrum occupancy as the

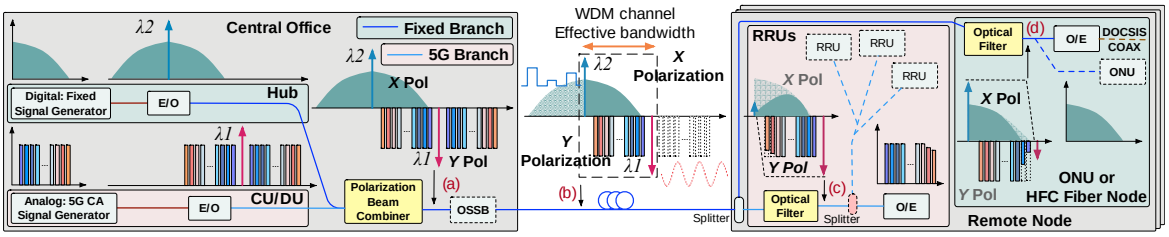


Figure 2.9 Schematic diagram and operating principles of the PDM system. (E/O: electrical to optical conversion). © IEEE 2018.

original fixed network. Therefore, it can be effectively scaled up to a WDM network which is widely deployed in current fixed access networks.

### *2.2.1 Operating Principles*

The operating principles of the proposed polarization-tracking-free PDM system are illustrated in Figure 2.9. Two lasers generate the optical carriers for 5G and fixed networks. The spectrum encompassed by two optical carriers is the effective bandwidth of the PDM system, as shown at in Figure 2.9, point (b). Two optical signals are combined and aligned to two orthogonal polarizations through a polarization beam combiner (PBC). Frequency overlap exists between two optical signals owing to PDM. After the PBC, optical single sideband (OSSB) can be applied to filter out the redundant sidebands. Here OSSB can be achieved by a tailored optical filter or simply by the bandwidth confined by one WDM channel.

In conventional PDM systems, complicated DSP is required to separate two polarizations. However, in this system only the desired optical signal is reserved and extracted after photo-detection, by suppressing the optical carrier on the opposite polarization. For example, the optical carrier of the fixed branch is filtered out to extract the 5G signal. Losing a major part of the optical carrier, the residual optical signal of the fixed branch only outputs weak noise-like electrical signal at the PD as indicated by Figure 2.9, point (c) and (d). It is worth noting that the power of such noise-like electrical signal is proportional to the residual power of its filtered optical carrier. With an appropriate small guard band, the proposed tracking-free design can relax the alignment accuracy of the optical filtering and still provide high isolation for PDM demultiplexing. The trade-off

exists between the width of the guard band and wavelength alignment. As the wavelength of the optical filter deviates, the guard band is supposed to be widened to avoid failure in PDM demultiplexing, which can be quantified by signal-to-interference and ratio (SIR), the power ratio between the desired signal and the interference from the undesired signal. The width of guard band is jointly dependent on the steepness of the optical filter and the alignment accuracy. Assume frequency difference of $\Delta f_1$ is needed for the given roll-off of the optical filter to achieve the carrier suppression associated with the targeted SIR, and the allowed frequency misalignment is $\pm\Delta f_2$, then the guard band should be larger than $\Delta f_1 + 2 \times \Delta f_2$. In the experiment, more than 20dB suppression of the opposite optical carrier can be obtained, meaning that the SIR of the desired electrical signal can achieve more than 20dB. As a result, the system can separate two polarizations with satisfying SIR without complicated polarization tracking.

In the proof-of-concept experiment, without losing generality PAM4 is applied for the fixed branch. For the 5G branch, the PDM system serves as the link fronthaul I (FH I) between the CU/DU and RRUs defined in NGFI [16]. In this work, A-RoF OFDM is employed. It is worth noting that the modulation formats on both polarization states are independent. The hybrid digital and analog transmissions employed in this experiment exemplify the capability of the proposed PDM system. In the experiment, in order to focus on the fiber infrastructure sharing achieved by the proposed polarization-tracking-free PDM scheme, transmissions of both the fixed and 5G branches terminate at the remote nodes. Further delivering of the 5G branch optical signal to each RRUs and their spectrum assignment will not be included here.

### *2.2.2 Experimental Setup*

The experimental setup is shown in Figure 2.10. The wavelengths of two ECLs are 1548.978nm (ECL1) and 1548.720nm (ECL2) for the 5G and fixed network, respectively, encompassing effective bandwidth of 33GHz. The electrical digital and analog signals are modulated to the optical carriers through two MZMs. The optical filtering mentioned in section 2.2.1 to obtain single-sideband signals is skipped in this experiment due to limited optical filters. Instead, the optical filters in the receiver which are used to reject opposite optical carriers for PDM demultiplexing will take over this duty and inherently achieve the OSSB operations. This modification will not significantly impair the performance of the overall system. The spectrum of two light sources carrying signals is plotted in Figure 2.10(a). Figure 2.10(b) gives an example spectrum when the optical filter in the transmitter is applied and out-of-band sidebands are filtered out, providing a clean spectrum within the PDM channel. After the PBC, the hybrid optical signal is transmitted over 20km SMF. At the receiver, i.e., the remote node, the hybrid optical signal is first amplified by an EDFA and then split into two branches. In each branch, an optical interleaver functioning as an optical band-stop filter passes the hybrid PDM signal, with its notch aligned to the wavelength of the opposite optical carrier. The spectra of the filtered optical signals are plotted in Figure 2.10(c) and (d). Optical-carrier suppressions can achieve 30dB and 20dB in the 5G and the fixed branches, respectively. A PIN PD (u2t XPDV2120) with 50GHz bandwidth is used to detect the optical signal and the output electrical signal is captured by an oscilloscope for offline DSP and analysis.

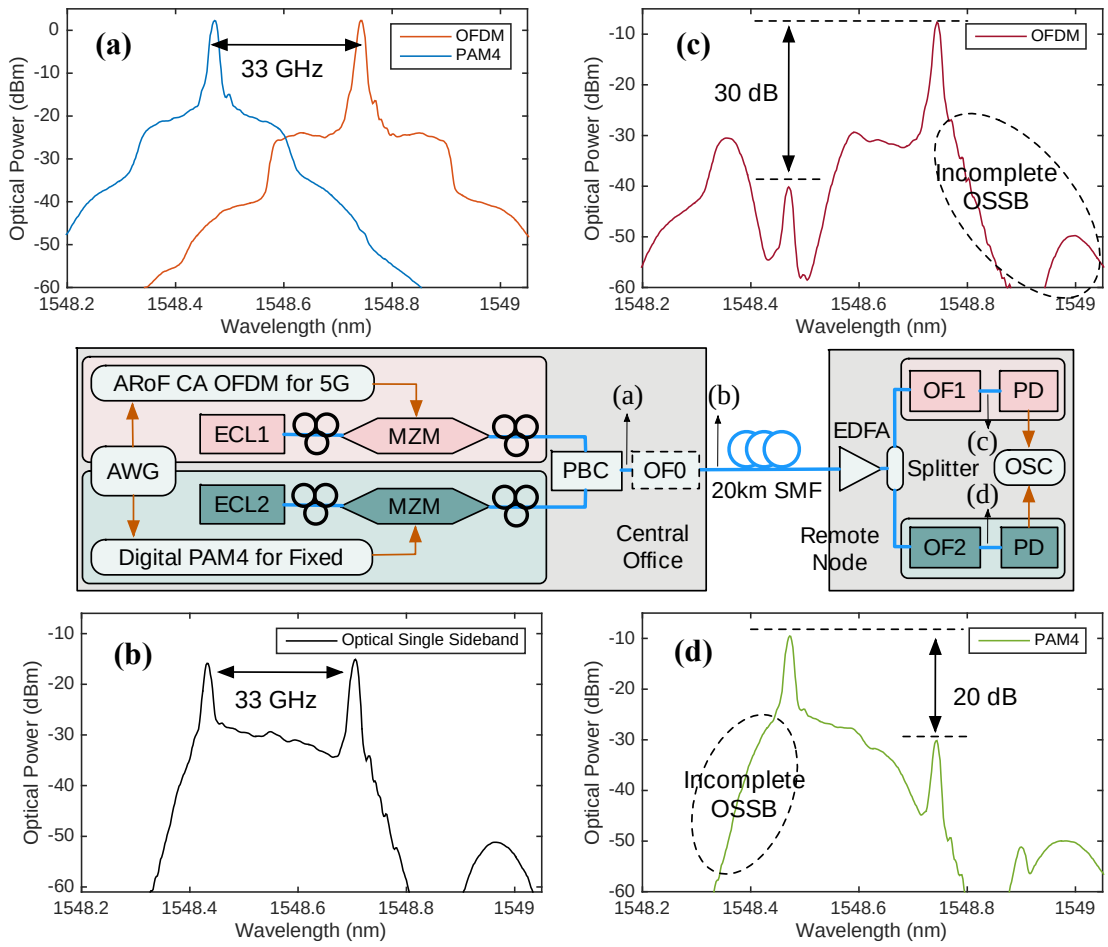


Figure 2.10 Experimental setup of the PDM system and optical spectra at the corresponding positions. © IEEE 2018.

In the 5G/analog branch, carrier-aggregation (CA) OFDM signal is transmitted. The multiband OFDM signal consisting of 34 bands spans from 400MHz to 20.8GHz. The subcarrier spacing is 30MHz. Each band has 18 payload subcarriers and the OFDM guard band comprises 2 subcarriers. The modulation format of each subcarrier is 16QAM, hence the data rate of the OFDM signal is 73.44Gbps. Frequency-domain one-tap zero-forcing (ZF) equalization is applied in the OFDM demodulator after Fast-Fourier Transform (FFT) and cyclic prefix (CP) removal to recover the signal. In the fixed/digital branch, PAM4 signal is transmitted. The baud rate of the PAM4 signal is 35GBaud, providing a data rate of 70Gbps. Nyquist filtering is used to pulse-shape the PAM4 symbol, with the PAM4

signal occupying 17.5GHz electrical bandwidth. Minimum-mean-square-error (MMSE) equalizer is used in the PAM4 receiver to recover the signal. Both the OFDM and PAM4 signals are generated by an AWG (Keysight, M8195A, 20GHz 3dB bandwidth) and captured by an oscilloscope (Keysight, DSOZ254A, 25GHz physical bandwidth). It is worth noting that it is the limited bandwidth of AWG that constrains the overall data rate. With a wider available bandwidth of AWG and oscilloscope, the overlap of two polarizations would be wider and higher data rate can be delivered by the PDM system. In the experiment, the sampling rate of AWG is 60GSa/s, the sampling rate of the oscilloscope is 80GSa/s. The received signal is first down-sampled and then down-converted (only for the 5G branch) to the baseband. For both fixed and mobile signals, Volterra equalization is applied before other equalization process to mitigate the non-linearity.

### *2.2.3 Experimental Results*

In the experiment, BER versus the ROP of the PDM system is measured for both branches. The transmission scenarios with and without 20km SMF and the multiplexing scenarios with and without PDM for each branch are measured. For the scenario without PDM, all setups remain the same as that with PDM except that the opposite polarization is disconnected from the PBC. Furthermore, the crosstalk between polarizations is also investigated. In the crosstalk measurement, the ROP of the desired optical power is fixed and the optical power of the other branch is varied.

For the digital/fixed branch, 70Gbps data rate is achieved over 20km SMF. The power spectral density (PSD) of the PAM4 signal retrieved by the oscilloscope is shown in Figure 2.11(a). From Figure 2.11(b), BER of the fixed branch achieved below the HD-

FEC threshold at $3.8 \times 10^{-3}$ after 20km SMF. For 20km SMF scenario, the receiver sensitivity is around 1dBm, which can be improved by using PD with the transimpedance amplifier (TIA) or an avalanche photodiode (APD). Compared to the results in the B2B transmission, there is 4dB penalty of sensitivity, mainly due to the incomplete OSSB filtering during the polarization demultiplexing process shown in Figure 2.10(d). On the other hand, the BER performance of the digital branch with and without PDM is shown in Figure 2.11(c). It can be seen that PDM has induced 4dB sensitivity penalty. This penalty mainly results from the residuals of the opposite polarization, which not only shares the EDFA gain and ROP quota but also induces the noise-like beating signal. To investigate the crosstalk, Figure 2.11(d) plots the influence of the analog branch to the digital branch on BER. It can be seen that the BER variation of the digital branch is less than one order of magnitude when ROP of the analog branch varies from 4.5dBm to -8.5dBm, proving the stability of the proposed PDM system.

For the analog/5G branch, data rate of 73.44Gbps is achieved. The PSD of the 5G CA OFDM signal captured by the OSC is shown in Figure 2.11(e). For the OFDM signal, BER of channel 2, 19, 34 (CH2, 19 and 34) are selected for illustration without losing generality. The penalty due to fiber transmission is more prominent for inner bands as shown in Figure 2.11(f), as the outer bands suffer more from low SNR hence penalty due to fiber transmission is less significant in comparison. The other reason is SSBI induced by incomplete OSSB. Similarly, when comparing the BER with and without PDM, inner bands present greater penalty caused by PDM as shown in Figure 2.11(g). In the investigation of the influence of the digital branch to the analog branch, it can be seen from Figure 2.11(h) that the BER of each channel varies within one order of magnitude except

for the extreme case, given the ROP of the digital branch fluctuating over 13dB (-8.2dBm to 4.8dBm).

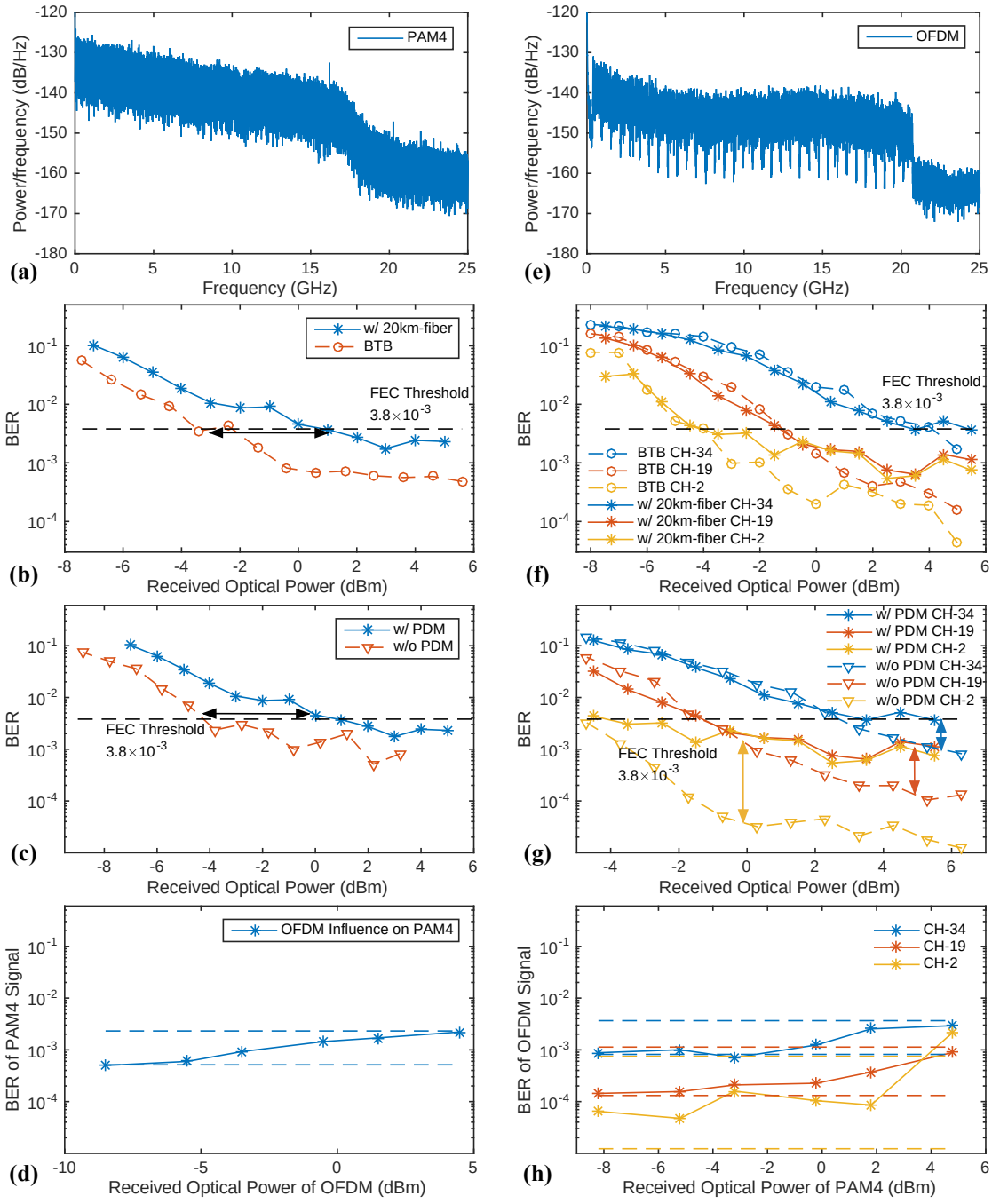


Figure 2.11 Fixed (PAM4) branch: (a) PSD. BER versus. ROP: (b) with and without SMF; (c) with and without PDM; (d) crosstalk. Wireless (OFDM) branch: (e) PSD. BER versus ROP: (f) with and without SMF; (g) with and without PDM; (h) crosstalk. © IEEE 2018.

### *2.2.4 Summary*

It has been demonstrated in this work that the proposed polarization-tracking-free PDM system is capable of supporting the co-transmission of digital and analog signals for fixed and wireless services, providing 70Gbps data rate over 20km SMF for each polarization. Regarding the crosstalk issue, it has been shown that the BER variation of one polarization can maintain within one order of magnitude with the optical power of the opposite polarization changing over 13dB ROP, proving the desirable and stable operation of the system. In comparison with a regular non-PDM system, the additional devices needed to implement the proposed PDM system are mainly passive devices such as PBC and optical filters, yet successfully bypassing the complicated polarization-tracking DSP required in conventional PDM systems. These devices are added in the central office and remote nodes requiring no changes in the fiber access networks, avoiding the high cost to pull extra fiber. The proposed PDM system is spectrum-efficient and WDM-compatible.

# CHAPTER 3 ADVANCED ACCESS TECHNOLOGIES FOR PERFORMANCE OPTIMIZATION

Radio and fixed access networks have many differences on various aspects, yet both face common challenges and aim to adopt cutting-edge technology innovations. For example, a wireless access network usually operates under channels that are complicated by severe multi-path effect and limited bandwidth, while a fixed access network is normally required to support long-distance fiber transmission with wider available bandwidth. Applications of advanced access technologies can be seen in 5G NR, PON and HFC. In NR, FH I is the link between DU and RRU and is close to end-users, supporting latency-sensitive services. A-RoF can be used in FH I to provide low-latency services, which requires the FH I waveforms to have the same performance as 5G wireless waveforms. In PON, advanced waveforms can provide large capacity and multi-user access, which are expected by high-speed broadband access. In HFC, bandwidth limitation of coax cable and long fiber access distance of 10-80km (as shown in Figure 1.2) requires access technologies with high spectral efficiency and long-distance transmission capability.

Radio and fixed access networks are facing the challenge to support data-demanding users with limited infrastructure and bandwidth resources. In response to the challenges, issues including carrier aggregation, interference control, spectrum efficiency, advanced decoding algorithms have drawn much attention from both sides. In this chapter, we mainly investigate two important OFDM-based access technologies: windowed OFDM and pattern division multiplexing access (PDMA). In the dissertation, the principles of the

technologies will be studied, as well as the applications customized for different requirements from radio and fixed access networks.

## 3.1 Windowed OFDM

To enhance capacity, modulations with higher spectral efficiency have been investigated and deployed in various access networks. In DOCSIS 3.1, QAM has been upgraded to OFDM to achieve higher spectral efficiency. Optical code division multiple access (OCDM) and NOMA have been proposed for flexible PON access[38], [54]. In 5G waveform research, advanced waveforms such as FBMC [35], UFMC [36], generalized frequency division multiplexing (GFDM) [55], and WOLA [37] have been widely studied and discussed.

Carrier aggregation and cell densification are important approaches to boost the throughput. In 5G, mmWave, small cell is one of the key technologies to support the capacity explosion. It is anticipated that more than 100 femtocells can be deployed within $1km^2$. With such densely deployed access units, it is crucial to control the signal processing complexity and cost of the A-RoF links connecting DUs and RRUs. Carrier aggregation is employed not only in 5G but also in other access networks such as HFC. In fact, channel bonding is one of the new features of DOCSIS 3.1. In addition, for HFC and PON that have in-place coax and fiber infrastructure, with limited bandwidth and high capital expenditures (CAPEX) to pull new fiber, it is desirable to implement the waveforms with high spectrum efficiency to exploit the capability of the networks.

To mitigate the interference caused by out-of-band leakage and inter-carrier interference (ICI) is critical for carrier aggregation. In the small-cell structure, interference

suppression will become even more challenging, due to issues such as greater carrier frequency offset (CFO) owing to deployment of mmWave frequencies. To realize cell densification, it is important to improving cell performance while controlling cell cost with low DSP complexity. Out-of-band leakage reduction facilitates efficient carrier aggregation, and CFO resistance relaxes the DSP burden in high-frequency bands. In this section, windowed OFDM for mobile fronthaul and fixed optical access will be introduced and demonstrated, achieving reduced out-of-band leakage and improved CFO suppression with low-complexity DSP and no additional overhead. The related works are published in *OFC 2018* [56], [57].

### *3.1.1 Operating Principles*

Waveforms such as FBMC and UFMC suppress out-of-band emission by applying filters to each subcarrier or subsets of subcarriers. The filtering involves convolution process whose computational complexity is $O(N \log N)$, in which *N* is the OFDM block length, resulting in excess DSP complexity. Windowed OFDM suppresses the out-of-band leakage by introducing windowing process in the transmitter and dual windowing in the receiver. The windowing is a time-domain multiplication process whose computational complexity is $O(N)$. The windowing is applied after upsampling in the transmitter and the dual windowing is applied before the downsampling in the receiver. In comparison, WOLA also introduces windowing in the OFDM DSP. In WOLA, both prefix and suffix are required for the weighting process as the roll-off period (RP), which results in longer OFDM symbol length and consumes more time-domain resources [37]. In contrast, windowed OFDM utilizes prototype filters which are short perfect reconstruction filters that require no extra overhead [58].

In conventional OFDM with CP, the prototype filter is in the shape of a rectangular [59], with filter length *L* equaling to the length of the data block *N*, as shown in Figure 3.1(a). The windowed OFDM studied in this chapter is based on short perfect reconstruction pulses. The length of a short perfect reconstruction filter is shorter than or equal to the length of each data block. Two design criteria are considered for the prototype filters used in windowed OFDM in order to achieve out-of-band leakage suppression. One is minimization of the out-of-band energy, and the other is maximization of the time-frequency localization. Based on these criteria, two types of filters are designed: time-frequency localization (TFL) and out-of-band energy minimization (OBE) filters. From [59], the closed-form expressions of rectangular filters (for conventional OFDM), TFL and OBE filters are:

$$\gamma_{RECT}[i] = \begin{cases} 1 & 0 \leqslant i \leqslant N-1 \\ 0 & otherwise \end{cases}$$
$$\widetilde{\gamma}_{RECT}[i] = \begin{cases} 1 & \Delta \leqslant i \leqslant N-1 \\ 0 & otherwise \end{cases} \tag{2}$$

$$\gamma_{TFL}[i] = \widetilde{\gamma}_{TFL}[i] = \begin{cases} \sin\left(\frac{(2i+1)\pi}{4\Delta}\right) & 0 \leqslant i \leqslant \Delta-1 \\ 1 & \Delta \leqslant i \leqslant M-1 \\ \sin\left(\frac{(2(\Delta-i)+1)\pi}{4\Delta}\right) & M \leqslant i \leqslant N-1 \\ 0 & otherwise \end{cases} \tag{3}$$

$$\gamma_{OBE}[i] = \widetilde{\gamma}_{OBE}[i] = \begin{cases} \cos\left(\tilde{a} + \tilde{b}\frac{(2i+1)\pi}{2\Delta}\right) & 0 \leqslant i \leqslant \Delta-1 \\ 1 & \Delta \leqslant i \leqslant M-1 \\ \cos\left(\tilde{a} + \tilde{b}\frac{(2i+1)\pi}{2\Delta}\right) & M \leqslant i \leqslant N-1 \\ 0 & otherwise. \end{cases} \tag{4}$$

where *i* is the time domain sample index; $\Delta = N - M$, $\Delta$ is the CP length, *N* is the length of the data block, *M* is the FFT size, $\tilde{a}$ and $\tilde{b}$ are constants given in [59]. For each type of filters, there are the filters used on the transmitter side ($\gamma_{RECT}$, $\gamma_{TFL}$, and $\gamma_{OBE}$) and dual filters in the receiver side ($\widetilde{\gamma}_{RECT}$, $\widetilde{\gamma}_{TFL}$, and $\widetilde{\gamma}_{OBE}$). Their filter shapes are plotted in Figure 3.1(a), with *M* = 2048 and $N = M \times (1 + \frac{1}{4}) = 2560$. Figure 3.1(b) shows the frequency response of the three filters. In OFDM, the frequency response of each subcarrier will follow the frequency response of its prototype filter. From Figure 3.1(b) it can be seen that the sidelobe amplitudes of TFL and OBE filters decrease faster than rectangular filter. Fast decay of side lobes provides TFL- and OBE-windowed OFDM symbol with smaller out-of-band leakage

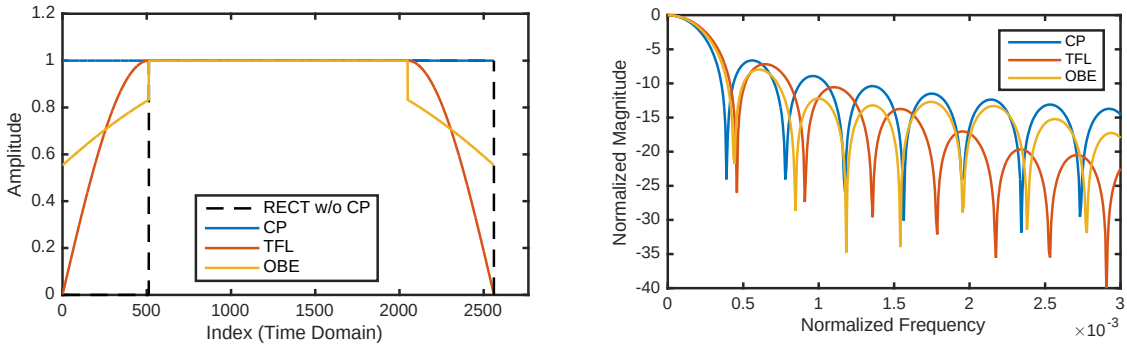


Figure 3.1 Time-domain pulse shapes of conventional rectangular windows with (blue) and without CP (black dashed), TFL (red) and OBE windows (yellow); (b) Frequency response. © OSA 2018.

Compared to conventional CP OFDM, the windowed OFDM requires only one additional windowing step, which is to multiply a time-domain window to shape the OFDM symbol as shown in Figure 3.2(a). While for WOLA, extra window prefix and suffix on top of CP, namely, the RP (*W*), will be added to the OFDM symbol as indicated in Figure 3.2(b). Furthermore, overlap-and-add is applied here in the signal generation to

keep the length of one OFDM symbol to be *CP + N + W*, instead of simply concatenating in windowed and CP OFDM. The spectra of single-band windowed, WOLA and CP OFDM are presented in Figure 3.2(c), from which it can be seen that TFL and WOLA can achieve 20dB out-of-band emission reduction in comparison with CP OFDM. When compared to WOLA, windowed OFDM can achieve comparable out-of-band leakage suppression without requiring extra overhead.

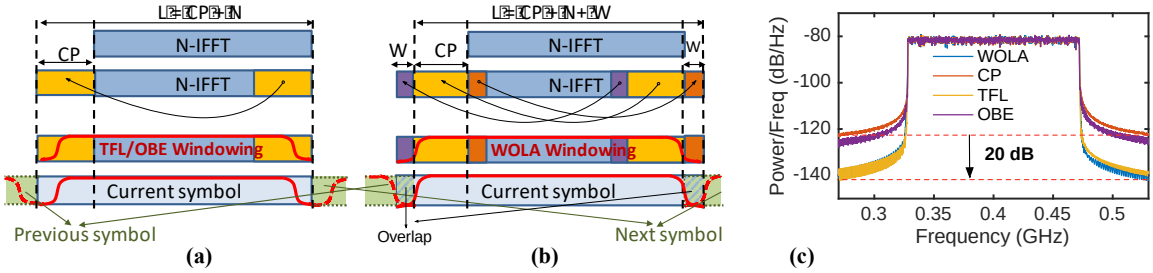


Figure 3.2 Block structure (a) of windowed OFDM; (b) WOLA. (c) Spectra of different single-band OFDM-based signals. © OSA 2018.

The advantages of windowed OFDM are amplified when it comes to high-capacity multiband transmission. In LTE, 2MHz guard band is reserved for 18MHz payload bandwidth; similarly, in DOCSIS 3.1, at least 2MHz exclusion band is reserved for any two adjacent asynchronous OFDM channels [32]. The minimum bandwidth of OFDM in DOCSIS 3.1 downstream is 24MHz. Assume that there are 30 consecutive active downstream OFDM channels, then 60MHz out of 720MHz are reserved for guard band without carrying bits. Excessive guard bands have diminished the spectrum efficiency of conventional OFDM. However, the band gap can be reduced if the out-of-band leakage is suppressed. As illustrated in Figure 3.3, given the same allowed interference level, the waveform with lower out-of-band leakage can accommodate much more payload bandwidth, as the required guard band is much narrower.

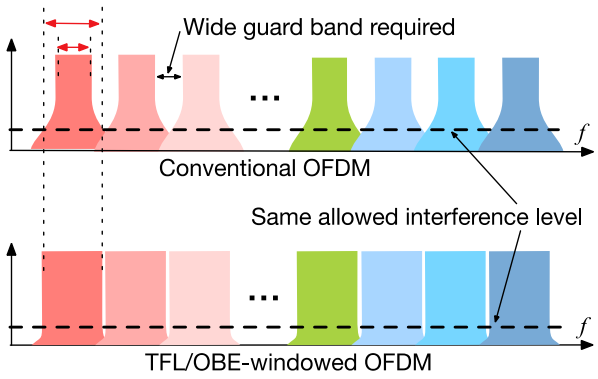


Figure 3.3 Spectrum availability of multiband signals with different out-of-band emission levels. © OSA 2018.

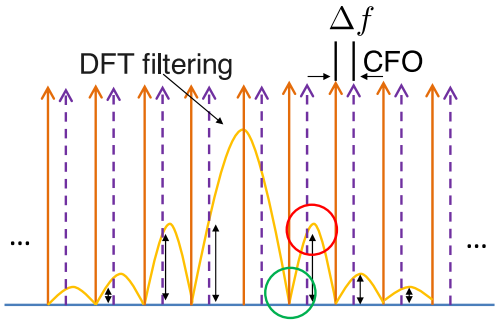


Figure 3.4 ICI generation. (Red/green circle: with or without CFO). © OSA 2018.

Another important advantage of windowed OFDM is the improved resistance to CFO. As a matter of fact, windowed OFDM can provides better ICI resistance owing to its lower side-lobe power compared to conventional CP OFDM. In the OFDM receiver, discrete Fourier transform (DFT) is used to demodulate the received signal $r(m)$ in the time domain to $R(k)$ carried by each subcarrier in the frequency domain. After the process, $R(k)$ is:

$$R(k) = \sum_{m=0}^{M-1} r(m) e^{\frac{-j2\pi mk}{M}} \tag{5}$$

To visualize the demodulation process, assume only one subcarrier at frequency $f_0$ carries a symbol with value *A* and the rest carry zero. Then the received signal is:

$$r(m) = Ae^{j2\pi f_0 m} \tag{6}$$

Substitute Equation (6) into Equation (5), we have:

$$\begin{aligned} R(k) &= \sum_{m=0}^{M-1} Ae^{j2\pi f_0 m} e^{\frac{-j2\pi mk}{M}} \\ &= \sum_{m=0}^{M-1} Ae^{j2\pi m(f_0 - \frac{k}{M})} \\ &= Ae^{j\pi(M-1)(f_0 - \frac{k}{M})} \times \frac{\sin \pi M(f_0 - \frac{k}{M})}{\sin \pi(f_0 - \frac{k}{M})}. \end{aligned} \tag{7}$$

From Equation (7), the DFT process at the OFDM receiver can be viewed as filtering by *sinc* pulse for each subcarrier [60]. When the carrier frequency in the receiver is perfectly aligned with the original carrier, where $f_0 = \frac{k}{M}$, the second term in Equation (7), reduces to 1 and the symbol value *A* is extracted correctly; for other *k* values, $R(k) = 0$, therefore no ICI exists, as shown in the green circle in Figure 3.4. But when there is slight CFO $\Delta f = f_0 - \frac{k}{M}$, the second *sinc* term in Equation (7) will shape and impair the symbol whose value is supposed to be *A*, deviating the extracted symbol incorrectly. In addition to that, $R(k) \neq 0$ for other *k* values, therefore the extracted symbol will be degraded by ICI terms from other subcarriers as well. Figure 3.4 visualizes the DFT filtering process. When there exists CFO, the sampling point will deviate from the zero crossings of other subcarriers, shown by the red circle. Therefore side-lobe power will leak into the desired symbol. In windowed OFDM as shown in Figure 3.1(b), both TFL and OBE presents lower power starting from first side lobe which is the most significant contributor of ICI terms.

As a result, windowed OFDM provides better ICI resistance compared to conventional OFDM.

One result of applying windowed OFDM is that it will increase the peak-to-average-power ratio (PAPR). From Figure 3.1(a), it can be observed that the OFDM symbol is shaped in both rising and falling edges during the windowing process, which decreases the average signal power. Whereas the maximum amplitude of the signal stays unchanged, therefore PAPR increases. The increase of PAPR would result in a slight shift of optimal received optical power [58]. The degree of PAPR variation changes with the ratio $\frac{\Delta}{N}$. When the window edges ($\Delta/2$) shrink, PAPR decreases. The trade-off exists between the increase of PAPR and the length of CP ($\Delta$). Windowed OFDM also requires more stringent synchronization, caused by the symbol reconstruction after the dual windowing in the receiver-side DSP.

### *3.1.2 Experimental Setup of the mmWave System*

In the section, windowed OFDM is demonstrated over a mmWave-RoF testbed to investigate the CFO performance. Figure 3.5(a) shows the experimental setup. In the experiment, conventional CP OFDM, TFL- and OBE-windowed OFDM, as well as WOLA OFDM are transmitted respectively over the mmWave-RoF mobile fronthaul link. In addition to basic OFDM DSP, there are windowing step in the transmitter, dual windowing with the same pulse and CP folding in the receiver of windowed OFDM and WOLA [58], The 4-band OFDM signal transmitted over the link is centered at 550MHz. Each band occupies 144MHz and the bandgap is 23MHz. The FFT size is *N* = 2048, 1200 of which is the payload carrying 16QAM symbols and the subcarrier spacing is $f_{subc} = 120MHz$.

The CP is 1/8 and RP of WOLA are 1/20 of the FFT size, respectively. CFO is introduced during the down-conversion process of the receiver. Here CFO is measured as the percentage of the subcarrier spacing: $\epsilon = \frac{\Delta f}{f_{subc}} \times 100\%$.

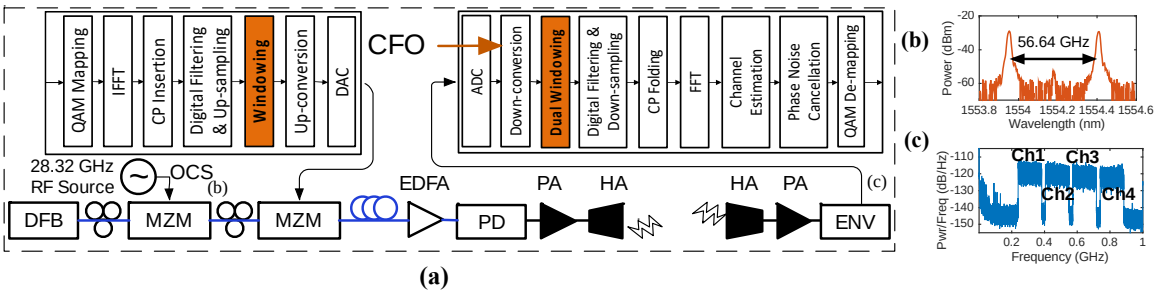


Figure 3.5 (a) Experimental setup and DSP steps; (b) Optical spectrum of OCS; (c) RF spectrum of the received signal. (ENV: Envelope detector.) © OSA 2018.

The mmWave is generated by optical carrier suppression (OCS) method in the experiment. A lightwave at 1550nm generated by a distributed feedback (DFB) laser is fed into an MZM biased at the null point. 28.32GHz microwave generated by the radio RF source is fed into the first MZM to obtain 56.64GHz separation with more than 25dB optical-carrier suppression, as depicted in the optical spectrum in Figure 3.5(b). OFDM signals generated by the arbitrary waveform generator is modulated to the optical carrier through the second MZM biased at the inflection point. The modulated optical signal is then transmitted through 15km dispersion shifted single-mode fiber (DSF), amplified by an EDFA, and detected by a PD, the output of which is the OFDM signal carried by mmWave carrier. The mmWave signal is amplified and then transmitted by a pair of 15dBi HA. The wireless link is 1m long. At the receiver, the mmWave signal is detected and down-convert to baseband by an envelope detector. Finally, the baseband signal is captured and sampled by a high-speed oscilloscope, and then goes through offline DSP. The experimental RF spectrum of the received 4-band OFDM signal is shown in Figure 3.5(c).

In the transmitter-side, the RF spectrum of the 4-band signals are shown in Figure 3.6, from which it can be seen that more than 20dB out-of-band leakage reductions can be observed for TFL windowed OFDM and WOLA.

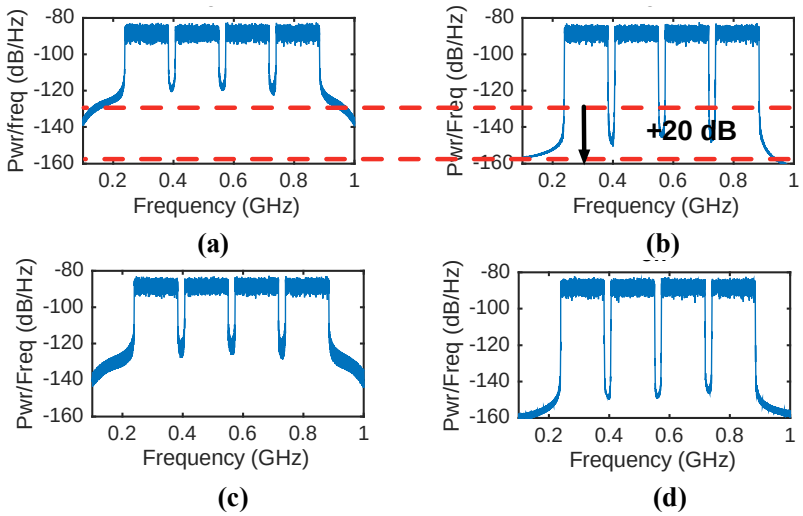


Figure 3.6 RF spectra of 4-band (a) conventional CP OFDM, (b) TFL-windowed, (c) OBE-windowed, and (d) WOLA OFDM. © OSA 2018.

### *3.1.3 Experimental Results of the mmWave System*

In experimental data analysis, it can be observed from Figure 3.7(a) that the performance of both TFL- and OBE-windowed OFDM is comparable to CP and WOLA OFDM when there is no CFO degradation. All four waveforms present similar ROP sensitivity, more than 5dB in B2B case and in transmission over 15km DSF. CFO sensitivity of different OFDM is first investigated. Figure 3.7(b) illustrates how EVM of Channel 1 (Ch1) varies with respect to $\varepsilon$, the ratio of CFO to the subcarrier spacing, in the B2B scenario with 0.5dBm ROP before the PD. It can be seen that in terms of CFO resistance OBE > TFL > WOLA > CP OFDM. In B2B transmission, at the 12.5% EVM threshold for 16QAM, the CFO tolerance of OBE-windowed OFDM is 6.8%, 1.5% (2.2dB) more than 5.3% of conventional CP OFDM, and 1.3% more than 5.5% of WOLA. Similar

results can be observed in Channel 3 (Ch3) as well, as shown in Figure 3.7(c). At CFO $\varepsilon$=6%, OBE-windowed OFDM exhibits 2.2% (1.5dB) EVM improvement compared to CP OFDM. Due to the limited bandwidth of the envelope detector, Ch3 experiences poorer channel SNR than Ch1.

TFL and OBE employ short perfect reconstruction window to fully utilize of the CP of OFDM signals [58]. CFO resistance of windowed OFDMs with respect to the CP length is investigated. Figure 3.7(d) depicts how variation of the CP length influences the CFO resistance of different OFDM signals in Ch1. Here the CFO is fixed at $\varepsilon$=6%, and the ROP before PD is 0.5 dBm. It can be seen that conventional CP OFDM remains the same CFO sensitivity despite the change of CP length. However, increasing CP length can significantly enhance CFO resistance for TFL- and OBE-windowed OFDM. With 1/4 CP

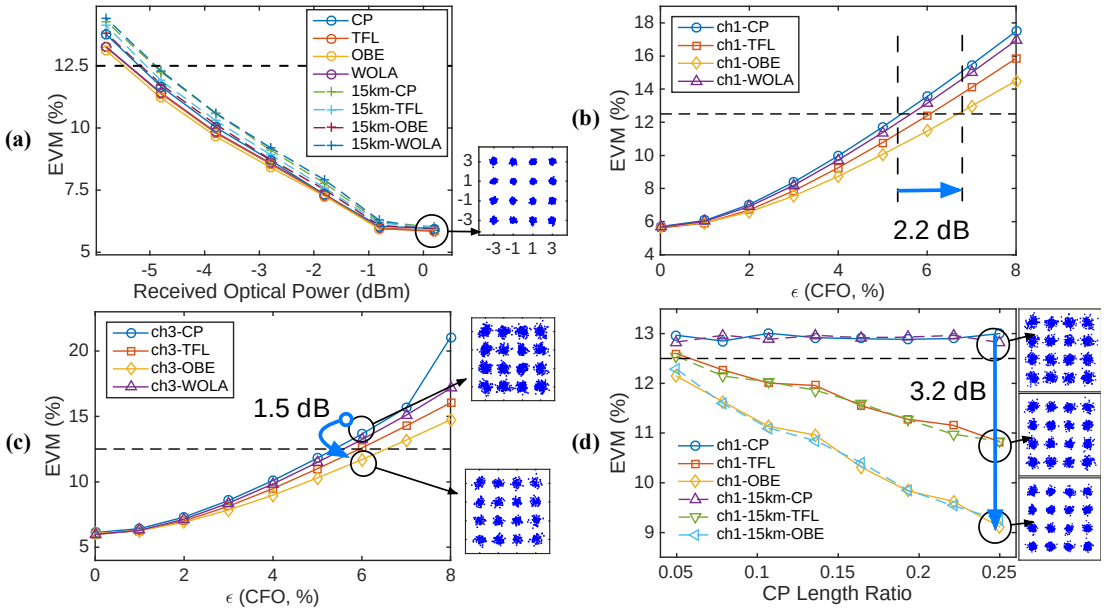


Figure 3.7 (a) EVM versus ROP of different OFDMs; EVM performance vs CFO of: (b) Ch1 and (c) Ch3 in B2B transmission. (d) EVM versus different CP-length ratio $\frac{\Delta}{N}$, with CFO $\epsilon = \frac{\Delta f}{f_{subc}} \times 100\% = 6\%$. © OSA 2018.

ratio, TFL- and OBE-windowed OFDM can achieve 9% and 11% EVM under 6% CFO, whereas the EVM of CP OFDM is 13%, beyond the required EVM threshold. With longer CP lengths, the CFO resistance of windowed OFDM system can be enhanced by 4% (3.2dB) EVM.

### *3.1.4 Experimental Setup of the Long-Distance Optical Access*

Besides the application in mmWave-RoF mobile fronthaul, windowed OFDM is also demonstrated over optical access, in which the requirements are different [56]. In PON, advanced waveforms help to provide large capacity and multi-user access which are expected by high-speed broadband access or PON backhauling for 5G. In HFC, bandwidth limitation of coax cable and long fiber access distance of 10-80 km require waveforms with high spectral efficiency and long-distance transmission capability.

The experimental setup for the proposed optical access with windowed OFDM is shown in Figure 3.8. A 14GHz class direct modulated laser (DML) is the low-cost transmitter and PIN receiver is the direct-detection receiver; cost-effective optical interleaver is used to achieve optical single side band (OSSB). OSSB is widely used to increase transmission distance [61]. In long-distance transmission, each sideband of double-sideband (DSB) signal experiences different phase changes due to chromatic dispersion (CD) over the wavelength span. When received at the PD, signals carried by two sidebands may beat destructively and cause severe power fading. In this work, Volterra algorithm is used for OSSB signal equalization of nonlinearity.

Most importantly, windowed OFDM is used to exploit the previously idled guard bands to enhance the spectrum utilization. Two experiments are conducted to validate the high-

performance optical access waveform. One is the single-band baseband OFDM (or discrete multi-tone, DMT) transmission. In this experiment, a 13.5GHz OFDM signal with or without windowing is transmitted over the optical link to investigate the transmission capability of windowed OFDM compared to conventional OFDM. The other experiment is the carrier-aggregation transmission with 12.6GHz bandwidth for 20 bands. The experiment is demonstrated to validate that guard band can be reduced by using windowed OFDM.

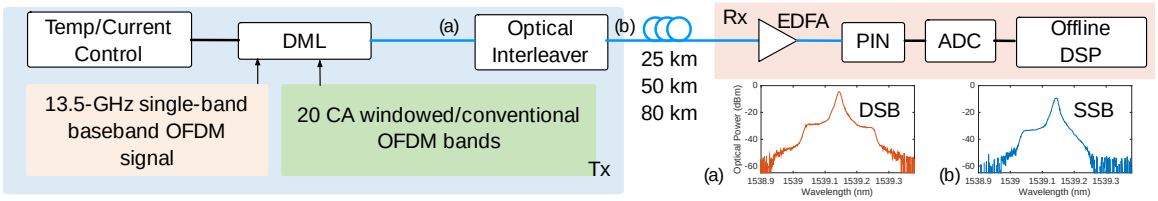


Figure 3.8 Experimental setup of both single-band and carrier-aggregation multiband OFDM transmissions.

The DML wavelength is 1539.15nm and is adjusted by the current and temperature control unit. After modulating the DML, the DSB optical signal is filtered by a 33/66GHz optical interleaver for OSSB. After long-distance SMF link, the OSSB signal is amplified by an EDFA, and directly detected by a PIN photodiode. The electrical signal is generated by an AWG and directly modulated to DML. At the receiver, the detected electrical signal is captured and collected by a high-speed oscilloscope and then goes through offline DSP.

For single-band OFDM signal, the FFT size is $M$ = 2048, 900 of which is the payload carrying 16QAM symbols with the subcarrier spacing $f_{subc} = 30MHz$. CP length is $\Delta = \frac{1}{16} \times M = 128$ and the symbol length is $N$ = 2176. Conventional rectangular window, TFL and OBE windows are generated and applied to the OFDM symbol according to

Equation (2), (3) and (4) given *M*, $\Delta$, and *N*. With 13.5GHz bandwidth and 16QAM modulation, the overall data rate is 54Gbps.

For carrier-aggregation signal, 20 bands are generated for multi-service and multi-user scenarios. The multiband signal spans 12.6GHz bandwidth. For each band, the FFT size is $M_m = 32$. The subcarrier has the spacing of $f_{subc} = 30MHz$ and CP $\Delta = \frac{1}{16} \times M_m$. The multi-band experiment is designed to investigate the performance of conventional and windowed OFDM with reduced band gap. For each band, the central frequency is fixed while the number of payload subcarriers varies, as shown in Figure 3.9(a). The number of payload subcarriers varies from 15 to 20, so each band can occupy up to 600MHz bandwidth. The rest of the subcarriers are set to zero as the guard band. In the experiments, the number of idle guard-band subcarriers varies from 11, 9, 7... to 1 to investigate the minimum band gap required for conventional OFDM, TFL- and OBE-windowed OFDM. It is expected that the waveform with suppressed out-of-band leakage would tolerate narrower guard band. Figure 3.9(b) and (c) gives the simulated interference level for multiband conventional and TFL-windowed OFDM, in which there are 20 bands, and the guard band consists of 5 idle subcarriers. From their PSD, it can be seen that conventional

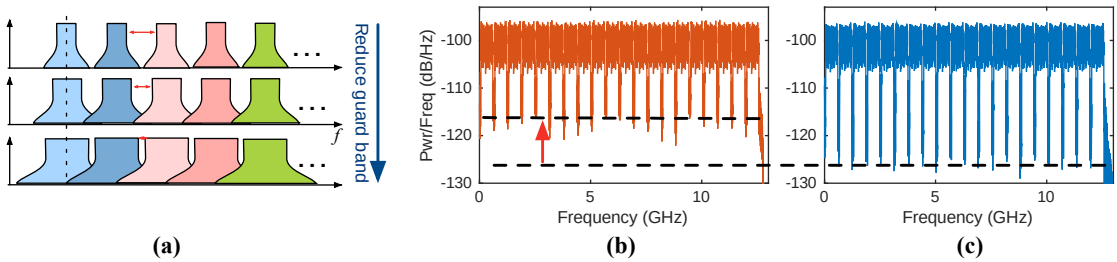


Figure 3.9 (a) Schematic diagram of the multiband signal with fixed center carrier frequency and reduced guard band. The PSD of 20-band (b) Conventional OFDM and (c) TFL-windowed OFDM with the guard band of 5 idle subcarriers. © OSA 2018.

OFDM exhibits much higher interference between bands compared to TFL-windowed OFDM.

### *3.1.5 Experimental Results of the Long-Distance Optical Access*

In the 13.5GHz single-band baseband experiment, the PSD of the OSSB and DSB windowed OFDM are depicted in Figure 3.10(a) and (b), respectively. It can be observed that the DSB signal has been severely corrupted by the power fading due to CD after 85km SMF transmission, while SSB signal just suffers from nonlinearity which can be corrected by the Volterra algorithm.

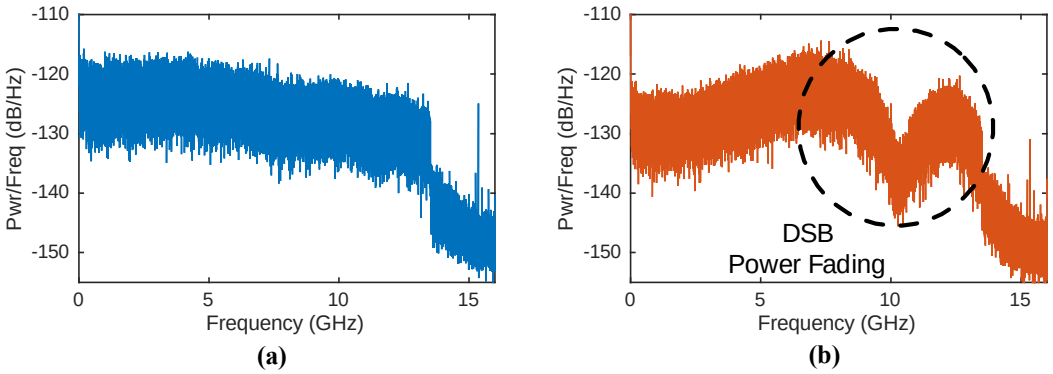


Figure 3.10 PSD of baseband signals after 85km SMF with (a) OSSB and (b) DSB transmission. © OSA 2018.

The BER performance with respect to the ROP in B2B, 25km and 50km transmission is shown in Figure 3.11(a). It can be observed that both TFL- and OBE-windowed OFDM present comparable transmission capability as conventional OFDM. As shown in Figure 3.11(b). BER below FEC threshold is achieved by windowed OFDM for over 85km SMF transmission, showing its ability to support high-speed and long-distance service with low-cost devices. Excluding the CP, the effective data rate of the high-performance optical access can achieve 50.6Gbps.

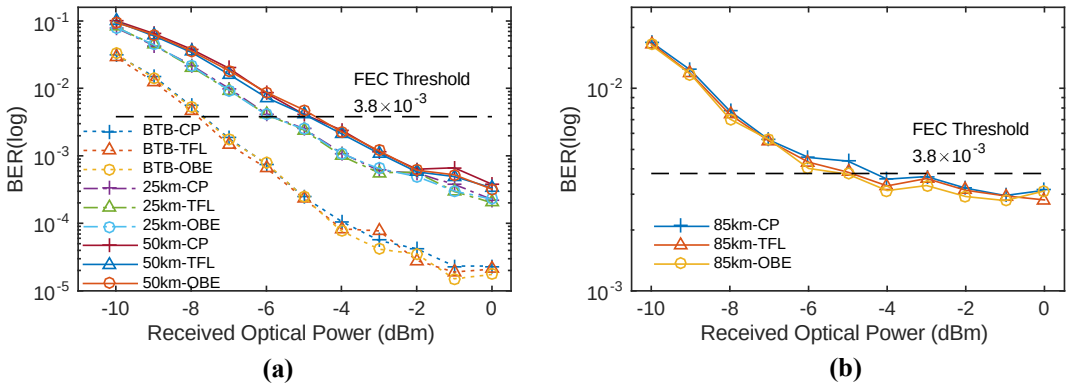


Figure 3.11 BER versus ROP of different baseband OFDM (a) in B2B, 25km and 50km SMF transmissions; (b) BER versus ROP of different baseband OFDM after 85km SMF. © OSA 2018.

As described in the experimental strategy of multiband transmission, 20 bands are transmitted for conventional and windowed OFDM. For each band, its central frequency is fixed while the number of idle subcarriers as the guard band is shrinking, resulting in higher inter-channel-interference. The RF spectrum of the multiband signal is shown in Figure 3.12. The signal is TFL-windowed OFDM with the guard band consisting of 7 idle subcarriers in B2B transmission. Due to the nonlinearity induced by OSSB transmission, fluctuation of BER exists across 20 bands.

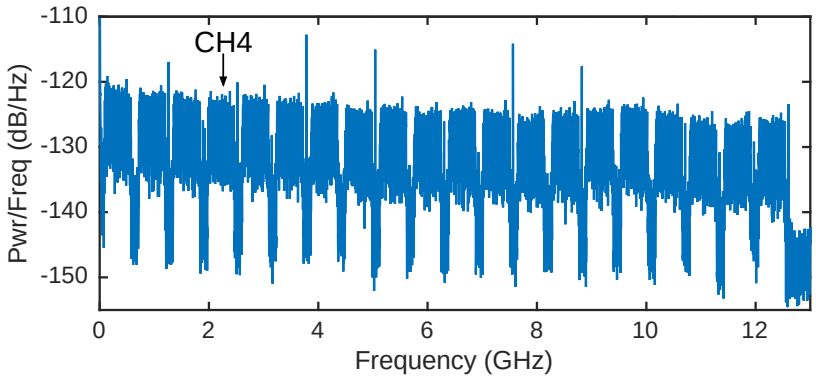


Figure 3.12 PSD of TFL-windowed OFDM in B2B transmission. © OSA 2018.

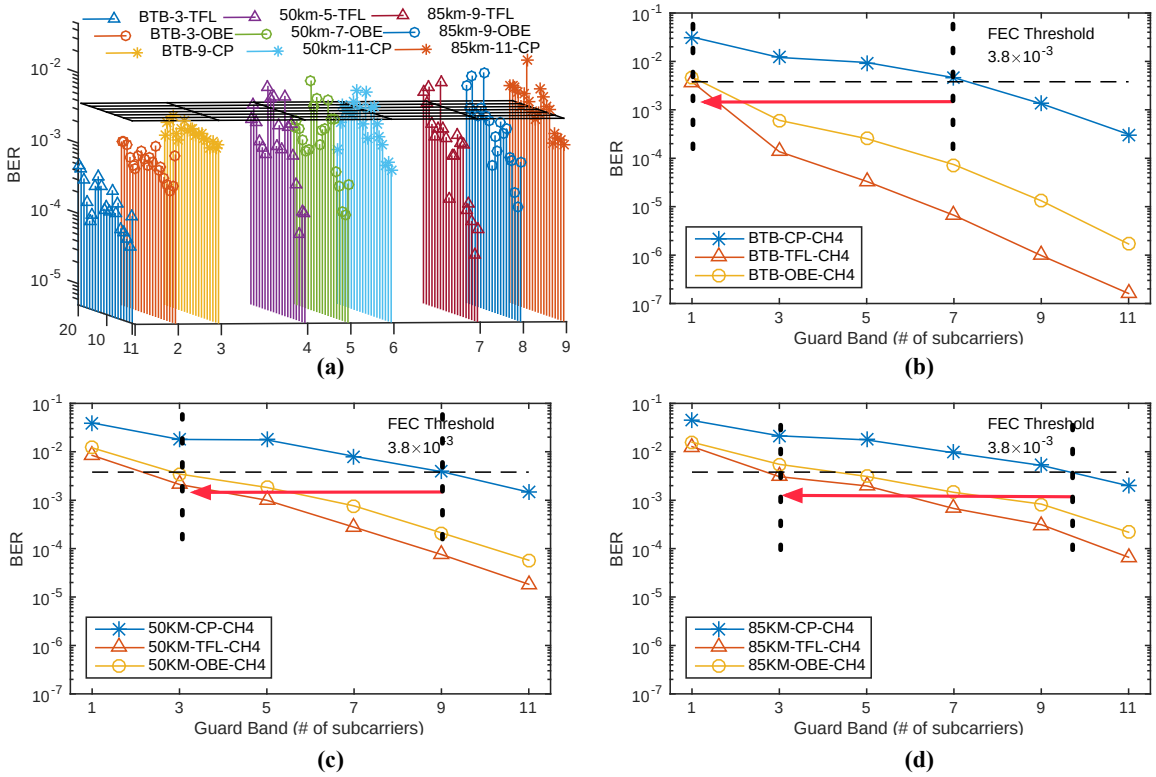


Figure 3.13 (a) The number of required idle subcarriers as the guard band. BER versus the number of idle subcarriers as the guard band. In 20-band signal for CH4 after (b) B2B, (c) 50km, and (d) 85km SMF transmissions. © OSA 2018.

The average BER performance of 20 channels with different band gap is scanned and shown in Figure 3.13(a), in which the number of idle subcarriers is the minimum value required for BER below FEC threshold in each transmission scenario. In B2B transmission, TFL-, OBE-windowed, and conventional OFDM require 1) 3-subcarrier, 2) 3-subcarrier, and 3) 9-subcarrier guard band, respectively. In 50km transmission: TFL-, OBE-windowed, and conventional OFDM require 4) 5-subcarrier, 5) 7-subcarrier, and 6) 11-subcarrier guard band, respectively. In 85km transmission: TFL-, OBE-windowed, and conventional OFDM require 7) 9-subcarrier, 8) 9-subcarrier, and 9) 11-subcarrier guard band, respectively. Among all the subbands, the BER of channel 4 (CH4, centered at 2.21GHz) is shown in Figure 3.13(b), (c), and (d). In B2B transmission, 7 idle subcarriers are required for conventional OFDM to achieve BER below FEC threshold, while it merely requires

one idle subcarrier as the guard band for TFL-windowed OFDM, achieving quasi-gapless performance. For 50km SMF link, TFL-windowed OFDM requires 3 idle subcarriers while conventional OFDM requires 9; for 85km SSMF, TFL-windowed OFDM needs 3-subcarrier guard band while conventional OFDM requires 10 subcarriers.

In B2B transmission, for only one channel (CH4), TFL-windowed OFDM can save $(7-1)\times 30\ MHz = 180\ MHz$ extra payload bandwidth compared to conventional OFDM. For all bands to achieve BER performance below FEC threshold, 3-idle-subcarrier guard band is required for windowed OFDM in B2B transmission, however, 9 idle subcarriers are required by conventional OFDM. As a result, windowed OFDM can save $(9-3)\times 30\ MHz \times 20\ (Bands) = 3.6\ GHz$ extra payload bandwidth. Compared to payload bandwidth of conventional OFDM with $12\times 30\ MHz \times 20\ (Bands) = 7.2\ GHz$ , windowed OFDM can achieve $(3.6\ GHz/7.2\ GHz + 1)\times 100\% = 150\%$ bandwidth gain. In 50km and 85km transmission, nonlinearity induced fluctuation is more severe. Therefore, those channels severely affected by nonlinearity are removed in the calculation of payload bandwidth and gain. 16 and 17 effective channels are included in 50km and 85km SMF transmission, respectively.

Table 3-1 Summary of payload bandwidth and bandwidth gain

| Type | B2B | | | 50 km | | | 85 km | | |
|---|---|---|---|---|---|---|---|---|---|
| | Subc# | BW($G$) | Gain | Subc# | BW($G$) | Gain | Subc# | BW($G$) | Gain |
| CP | 9 | 7.2 | 100% | 11 | 4.8 | 100% | 13 | 4.1 | 100% |
| TFL | 3 | 10.8 | 150% | 5 | 7.7 | 160% | 9 | 6.1 | 150% |
| OBE | 3 | 10.8 | 150% | 7 | 6.7 | 140% | 9 | 6.1 | 150% |

The payload bandwidth and bandwidth gain for conventional and windowed OFDM are summarized in Table 3-1. Figure 3.14 provides the BER scan of the effective channels of windowed OFDM used in Table 3-1. The channel BER of conventional OFDM with same guard-band width as OBE-windowed OFDM is also presented in Figure 3.14 as the benchmark. TFL-windowed OFDM needs much fewer idle subcarriers to achieve BER below FEC threshold than conventional OFDM. With significantly suppressed out-of-band leakage, TFL-windowed OFDM can bring about 160% and 150% bandwidth gain. In Table 3-1, it is worth noting that for 85km transmission, 11 idle subcarriers, which is the widest guard band option in the experiment, cannot guarantee BER below FEC threshold for conventional OFDM, as can be seen in in Figure 3.13(a), *y* axis = 9. Therefore, in the best case 13-subcarrier guard band is assumed for 85km transmission with conventional OFDM in Table 3-1, which is marked in gray. It can be seen that even provided with the best assumption, conventional OFDM presents poor transmission capability.

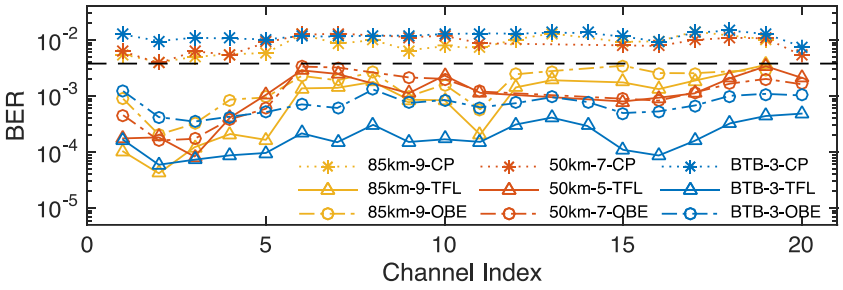


Figure 3.14 BER of the effective channels for windowed OFDM implemented with band gap and transmission distance in Table 3-1. © OSA 2018.

### *3.1.6 Summary*

In this work, windowed OFDM using short perfect reconstruction pulses is experimentally demonstrated for mmWave-RoF mobile fronthaul, providing effective out-of-band emission suppression and better CFO resistance requiring low-complexity DSP

and no additional overhead. 4-band OFDM signal with overall bandwidth 650MHz is well supported by the system. More than 20dB out-of-band leakage reduction and 2.2dB more CFO tolerance at the required EVM threshold is obtained for windowed OFDM. Moreover, increasing the CP length of the windowed OFDM enhances its CFO resistance. With only 1/4 CP ratio, the measured EVM has achieved 3.2dB improvement. The proposed windowed OFDM scheme enables efficient carrier aggregation and cell densification for 5G NR applications.

Moreover, low-cost and long-range optical access using windowed OFDM has been demonstrated with OSSB, direct modulation using 14GHz class DML and direct detection. The optical access can support over 50Gbps data rate after 85km SMF. In carrier-aggregation multiband transmission, the designed optical access based on windowed OFDM outperforms conventional OFDM. For various SMF distance, TFL- and OBE-windowed OFDM can achieve respective 160% (2.9GHz) and 150% (2GHz) payload bandwidth gain compared to conventional OFDM. Windowed OFDM extends the spectrum efficiency of OFDM-based waveforms with little additional DSP complexity and no extra overhead, strengthening its competitiveness when optical access networks urgently need more spectrum-efficient waveforms. High spectrum efficiency, high speed, low cost, and longer access range makes the optical access waveform based on windowed OFDM a promising candidate for advanced applications such as NGFI, HFC and PON access networks.

## 3.2 Pattern Division Multiple Access in mmWave-RoF RAN

Orthogonal multiple access (OMA) such as OFDMA has been the predominant access technology adopted by the current generation of mobile communication. Representing an evolutionary step in radio access networks, non-orthogonal multiple access (NOMA) is considered to be a promising technology to meet the goals of increased capacity, enhanced flexibility, and reduced latency. Pattern division multiple access (PDMA) is a NOMA scheme using resource-element mapping as the multiple-access signature in the symbol level. In this section, PDMA in a mmWave radio access system is studied with systematic experimental demonstration. One key advantage of PDMA is that it can facilitate advanced parallel interference cancellation (PIC) in the decoding process. A modified message passing algorithm (MPA) is developed and implemented to enhance the decoding performance of PDMA. A novel PDMA system integrated with MPA is experimentally demonstrated in a multi-user mmWave radio access system that uses RoF mobile fronthaul, achieving reduced sensitivity penalty and improved modulation spectral efficiency compared to conventional power-domain NOMA (PD-NOMA) with successive interference cancellation (SIC). Experimental results show that PDMA is capable of supporting disparate channel conditions, adapting to various patterns, and providing improved system flexibility. This work has been published in *Journal of Lightwave Technology* [62].

NOMA has been investigated for 5G and next-generation RANs to exploit under-utilized power resources and increase the number of UEs [39], [40]. Among various NOMA schemes, PDMA utilizes symbol-level UE-specific data signatures with sparse

resource-element (RE) mapping [42], which is capable of providing improved flexibility with different pattern variants and supporting grant-free uplinks [63].

In a 5G mmWave small-cell structure as shown in Figure 3.15, multiple users served by a RRU have to deal with different channel conditions. For example, there are users experiencing LoS links ($UE_1$, with channel 1, CH1), edge users which are far away from RRU experiencing low SNR and channel gain due to high path loss ($UE_2$ with CH2), or users suffering severe channel degradation ($UE_3$ with CH3) due to LoS blockage or antenna misalignment of the mmWave links. When managing multiple UEs with disparate reception qualities, RRUs employing conventional OFDMA have to trade off spectral efficiency to serve low-SNR users with low-order QAM modulation [41]. Recognizing these system limitations, NOMA is proposed to enhance capacity by exploiting power-domain multiplexing for multi-user access.

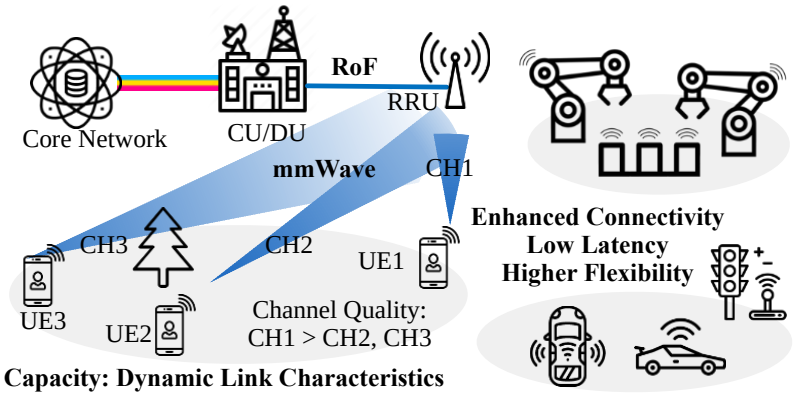


Figure 3.15 Challenges for next-generation service-oriented RANs employing mmWave links with various channel qualities. © OSA 2020.

One important advantage of PDMA is that it facilitates PIC in the DSP. As a comparison, SIC is used in conventional NOMA. SIC is susceptible to error propagation which makes the decoding of the received signal highly dependent on the error rate of

precedent users [64]. As one of the PIC schemes, MPA can be applied to enhance decoding accuracy for PDMA coded with sparse patterns. This is because MPA can approximate maximum *a posteriori* detection through algorithms based on factor graph, an equivalent representation of a pattern matrix. Owing to significantly enhanced decoding capability, PDMA with MPA will induce less interference on REs shared by multiple UEs, which can further support low-latency services with grant-free uplinks.

### *3.2.1 Fundamentals of PDMA and MPA*

PDMA is an OFDM-based NOMA scheme operating on the symbol level, combined with sparse RE mapping. For *K* users sharing *N* subcarriers (*K* > *N*), the key design element in PDMA is the pattern matrix. The pattern matrix defines how different users share the same resource block non-orthogonally. Three main functions of the pattern matrix are: 1) it provides the mathematical description and guidance for RE allocation; 2) the matrix can be tuned and optimized for interference control; 3) the symbol diversity in the matrix allows PIC. In this section, we will first introduce the basics of PDMA and its notations followed by the principles of MPA.

#### 3.2.1.1 Basics of PDMA

The pattern matrix is a binary matrix (containing only 1 and 0) that is defined as: $\mathbf{P}^{[N,K]} = [\mathbf{p}_1, \mathbf{p}_2, \ldots, \mathbf{p}_K]$, where $\mathbf{p}_k$ is an $N \times 1$ pattern vector that can be assigned to different streams/users [65]. The diversity order $D_k$ of a pattern vector is equal to the number of '1's in the vector. For *K* streams sharing the same resource block, there are *K* QAM symbols in the original symbol vector $\mathbf{x} = [x_1, x_2, \ldots, x_K]^T$. The transmitted symbol vector $\mathbf{s}_k$ of stream *k* is obtained by spreading $x_k$ according to pattern vector $\mathbf{p}_k$:

$\mathbf{s}_k = \mathbf{p}_m x_k$, where $\mathbf{s}_k$ is an $N \times 1$ vector. The amplitude and phase of each stream can be tuned to achieve the desired constellation for better interference control [42]. The scaling matrix is introduced for the scaling process: $\mathbf{A}^{[N,K]} = \mathbf{ia}$, where $\boldsymbol{a} = [a_1, a_2, \ldots a_K]$ is a $1 \times K$ vector with $a_k = \alpha_k e^{j\beta_k}$ comprising the amplitude ($\alpha_k$) and phase ($\beta_k$) and $\mathbf{i} = [1, 1, \ldots, 1]^T$ is an $N \times 1$ vector. In PDMA, one user can be assigned one or multiple streams. Therefore, the transmitted signal vector for each user is $\boldsymbol{t}_i = \sum_{k \in UE_i} a_k \boldsymbol{s}_k$, where $\boldsymbol{t}_i$ is an $N \times 1$ vector, and will be passed to next-stage OFDM processing. At the receiver, the corresponding channel response is: $\mathbf{H}^{[N,K]} = [\mathbf{h}_1, \mathbf{h}_2, \ldots, \mathbf{h}_K]$, where $\mathbf{h}_k$ is an $N \times 1$ vector, with many 0's in accordance to $\mathbf{p}_k$. As a result, the received signal vector in the frequency domain after preliminary OFDM processing will be: $\mathbf{r} = (\mathbf{H} \odot \mathbf{A} \odot \mathbf{P})\mathbf{x} + \boldsymbol{\nu}$. Here $\odot$ is the element-wise product and $\boldsymbol{\nu}$ is the additive white *Gaussian* noise (AWGN).

Pattern vectors can be assigned to users in different ways to meet the requirements of various applications. It is worth noting that the received constellation can be influenced by the stream amplitude/phase tuning at the Tx, modulation orders, and channel gain. In the experiments, streams are grouped and assigned to two users, given two sets of transmitters operating at mmWave frequency. Two examples are given in Figure 3.16 to illustrate stream-user assignment, stream tuning ($\boldsymbol{a}$), and QAM order assignment where *bpS* stands for bits per symbol, e.g. *bpS = 4* corresponds to 16QAM.

Shown in Figure 3.16(a) is case A where four subcarriers are shared by six streams assigned to two users, with $UE_1 = \{1, 4, 5\}$ and $UE_2 = \{2, 3, 6\}$. Case A is an example of grant-free uplinks supported by PDMA. In the basic upstream scheduling process in mobile

communications, users first request then wait for the grant distributed by the scheduler before payload data transmission [66]. In grant-based random access, resource blocks are selected and granted for a user at each time slot. In contrast, a user under grant-free access scheme is pre-assigned a unique user signature used for all time slots [63]. PDMA can skip the request-grant process by pre-assigning user-specific patterns for grant-free uplinks, therefore reducing latency. To achieve effective grant-free uplinks, methods such as joint

$$P_A^{[4,6]} = \left[\begin{array}{c|cc|cc|cc} \text{UE1} & \multicolumn{2}{c|}{\text{UE2}} & \multicolumn{2}{c|}{\text{UE1}} & \multicolumn{2}{c}{\text{UE2}} \\ s1 & s2 & s3 & s4 & s5 & s6 \\ \hline 1 & 0 & 1 & 0 & 0 & 0 \\ 0 & 1 & 0 & 1 & 0 & 0 \\ 0 & 1 & 0 & 0 & 1 & 0 \\ 1 & 0 & 0 & 0 & 0 & 1 \end{array}\right]$$

$$bpS = \left[\begin{array}{cccccc} 2 & 2 & 4 & 4 & 4 & 4 \end{array}\right]$$

$$\boldsymbol{a}_1 = \left[\begin{array}{cccccc} 0 & 0 & 7 & 7 & 7 & 7 \end{array}\right]$$

$$P_B^{[4,6]} = \left[\begin{array}{cc|cccc} \multicolumn{2}{c|}{\text{UE2}} & \multicolumn{4}{c}{\text{UE1}} \\ s1 & s2 & s3 & s4 & s5 & s6 \\ \hline 1 & 0 & 1 & 0 & 0 & 0 \\ 0 & 1 & 0 & 1 & 0 & 0 \\ 0 & 1 & 0 & 0 & 1 & 0 \\ 1 & 0 & 0 & 0 & 0 & 1 \end{array}\right]$$

$$bpS = \left[\begin{array}{cccccc} 2 & 2 & 2 & 2 & 2 & 2 \end{array}\right]$$

$$\boldsymbol{a}_2 = \left[\begin{array}{cccccc} 0 & 0 & 0 & 0 & 0 & 0 \end{array}\right] \quad (dB)$$

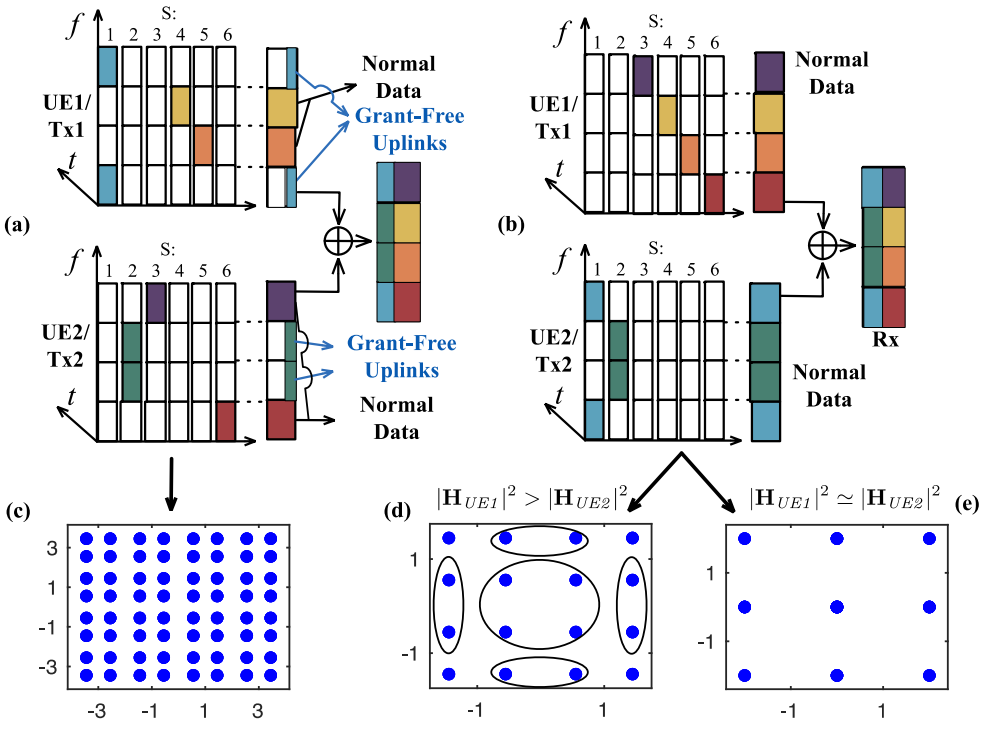


Figure 3.16 (a) Case A for grant-free uplinks; (b) Case B for data transmission with channel variations. Received constellation: (c) Case A; (d) Case B when channel gain of UE1 is larger than UE2; (e) Case B when both users experience similar channels (constellation ambiguity). © OSA 2020.

user activity and data detection should be employed and have been discussed in [67], [68]. For OMA, it is challenging to provide a sufficient number of orthogonal user signatures for pre-assigning, especially with the requirement of massive connectivity. Plus, time-frequency grids may be under-utilized in this case. While in PDMA, a pattern vector can be pre-assigned and reserved for a user as a third-dimension user signature on top of time and frequency dimensions. In this case, the cost of grant-free access is the interference among users sharing the same RE. Using PDMA integrated with MPA allows grant-free streams to co-exist with normal data streams, with a proper pattern design. Owing to the diversity of the symbol as well as the decoding capability of MPA, the required power level of the grant-free streams can be reduced to lower the interference on other streams sharing the same RE, without significantly sacrificing the performance.

The resource allocation process is visualized in Figure 3.16(a). The pattern of stream 1 (s1) is pre-assigned to $UE_1$ for grant-free uplinks, whereas s4 and s5 are allocated for normal data transmission. s1 has a much lower power level but higher diversity ( $D_{s1} = 2$) compared to s4 and s5 ($D_{s4,s5} = 1$), resulting in reduced interference on the other user that may be using the same REs. Given the corresponding stream amplitude tuning vector $\boldsymbol{a}_1$, QAM order assignment, and similar channel conditions experienced by both users, the received constellation is depicted in Figure 3.16(c).

In the case of data transmission with channel variations, case B, the same pattern matrix is used but with different stream-user assignment, modulation orders, and stream amplitude tuning, as shown in Figure 3.16(b). Both users utilize all four subcarriers. $UE_2$ is assigned two streams with higher diversity to cope with possible channel degradation. The received constellation under two different channel conditions are shown in Figure

3.16(d) and (e). When the channel gain of $UE_1$ is significantly higher than $UE_2$ (7dB in Figure 3.16(d)), the received constellation is similar to 16QAM due to the superposition of signals from two UEs. However, the received constellation will degenerate to that shown in Figure 3.16(e) when the channel gain of both users are on the same level, in which case one constellation point can represent multiple combinations of QAM symbols. In this case, constellation ambiguity occurs and should be considered in the decoding process.

#### 3.2.1.2 Message Passing Algorithm

Patterns used in PDMA bring diversity of the original symbols. In our demonstration, MPA is implemented in the receiver DSP to fully utilize this diversity. In MPA, the decoding process is based on information passing across the factor graph, which is determined by the pattern matrix. After several iterations of information exchanges and upon reaching convergence, MPA decodes all Tx symbols $\mathbf{x}$ simultaneously, in contrast to SIC where users are decoded successively.

At the receiver, the received symbol $r_n$ at RE *n* is:

$$r_n = \sum_{k=1}^{K} h_{n,k} a_k p_{n,k} x_k + \nu_n \triangleq \sum_{k=1}^{K} f_{n,k} x_k + \nu_n \tag{8}$$

Here $f_{n,k}$ is the effective signature element that includes channel distortion ($h_{n,k}$), stream amplitude/phase tuning ($a_k$), and the element of PDMA matrix ($p_{n,k}$). Let $\xi_n$ and $\zeta_k$ be the set of 1's positions in the $n_{th}$ row and the $k_{th}$ column of the pattern matrix, respectively. Then Equation (8) becomes:

$$r_n = \sum_{k \in \xi_n} f_{n,k} x_k + \nu_n = \mathbf{f}^{[n]T} \mathbf{x}^{[n]} + \nu_n \tag{9}$$

where $\mathbf{x}^{[n]}$ denotes the vector containing the symbols from streams participating in the $n_{th}$ row and $\mathbf{f}^{[n]}$ denotes the corresponding fraction of effective signature values.

The maximum *a posteriori* estimation for $\mathbf{x}$ is:

$$\hat{\mathbf{x}} = \arg \max_{\mathbf{x} \in \mathbb{X}^K} p(\mathbf{x}|\mathbf{r}) \tag{10}$$

From Bayes' rule, we have:

$$p(\mathbf{x}|\mathbf{r}) = \frac{p(\mathbf{r}|\mathbf{x})P(\mathbf{x})}{P(\mathbf{r})} \propto p(\mathbf{r}|\mathbf{x})P(\mathbf{x}) \tag{11}$$

in which $P(\mathbf{x}) = \prod_{k=1}^{K} p\left(x_k\right)$ is the joint *a prioroi* probability of the original symbol vector as the symbols are independent and identically distributed (i.i.d.) and $P(\mathbf{r}) = \sum_{\mathbf{x} \in \mathbb{X}^K} p(\mathbf{r}|\mathbf{x})P(\mathbf{x})$ is the probability of the received symbol vector. Furthermore, with the assumption that noise is i.i.d. and uncorrelated with the transmitted symbols, we have:

$$p(\mathbf{r}|\mathbf{x}) = \prod_{n=1}^{N} p\left(r_n|\mathbf{x}\right) = \prod_{n=1}^{N} p\left(r_n|\mathbf{x}^{[n]}\right) \tag{12}$$

Assume that the channel estimation is available at the receiver, under AWGN channel the probability of $r_n$ given $\mathbf{x}^{[n]}$ is:

$$p\left(r_n|\mathbf{x}^{[n]}\right) = \frac{1}{\sqrt{2\pi}\sigma}\exp\left(-\frac{1}{2\sigma^2}\left\|r_n - \mathbf{f}^{[n]T}\mathbf{x}^{[n]}\right\|^2\right) \tag{13}$$

Furthermore, combining Equation (10), (11), and (12), the estimation for $x_k$ can be obtained by maximizing the marginal probability:

$$\begin{aligned}\hat{x}_k &= \arg\max_{q\in\mathbb{X}_k}\sum_{\substack{\mathbf{x}\in\mathbb{X}^K\\ x_k=q}} p(\mathbf{x}|\mathbf{r}) \\ &= \arg\max_{q\in\mathbb{X}_k}\sum_{\substack{\mathbf{x}\in\mathbb{X}^K\\ x_k=q}} P(\mathbf{x})\prod_{n\in\zeta_k} p\left(r_n|\mathbf{x}^{[n]}\right)\end{aligned} \tag{14}$$

in which *q* is a symbol in constellation alphabet $\mathbb{X}_k$.

From Equation (10) to (14) the marginal probability $x_k$ is calculated instead of joint probability. In MPA, the decoding complexity is further reduced by approximating the marginal probability calculation iteratively over the underlying bipartite factor graph [69]. Figure 3.17 shows an example of a factor graph and the corresponding pattern matrix $P_C$. From the pattern matrix to the factor graph, each column ($x_k$) corresponds to a variable node (VN, $u_k$) and each row ($r_n$) corresponds to a function node (FN, $c_n$) Each edge $e_{n,k}$ in the factor graph means that the corresponding $p_{n,k} = 1$. In MPA process, messages containing the inference of $x_k$ are passed along the edges and updated in the FNs and VNs, using respective update functions. The MPA used in our demonstration is at the symbol level. When there are cycles in the factor graph, the iterative calculation will become an approximation of Equation (14).

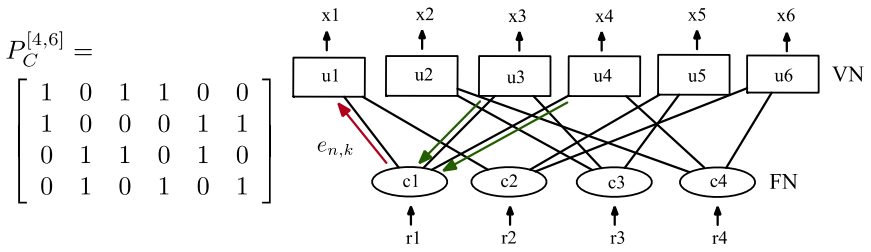


Figure 3.17 An example of a factor graph with the corresponding pattern matrix. © OSA 2020.

Provided that high-order QAM modulations are used, the message being exchanged along $e_{n,k}$ is a set with size $|\mathbb{X}_k|$, comprising the (inference) probability of symbols in $\mathbb{X}_k$. In each round of update, a node will collect messages from all of its connected nodes. It is worth noting that the message received by a node should be extrinsic, meaning that the message received from one edge cannot be used later to update the message to be transmitted onto that edge [69]. As shown in Figure 3.17, the message conveyed by the red arrow only contains the messages from the green arrows, despite the fact that $c_1$ has the access to the messages from all three nodes ($u_1, u_3, u_4$).

Let $\boldsymbol{\ell}_{c_n \to u_k}$ be the message set sent along $e_{n,k}$ from $c_n$ to $u_k$, then the message should only have extrinsic information:

$$\boldsymbol{\ell}_{c_n \to u_k} = \left\{ p(x_k = q | r_n, \mathbf{x}^{[n]} \backslash x_k), \forall q \in \mathbb{X}_k \right\} \tag{15}$$

Based on Equation (14), the message should include the product of the messages received from edges $e_{n,l}, \forall l \in \xi_n \backslash k$, and the observation at $c_n$ using local function $p\left(r_n | \mathbf{x}^{[n]}\right)$. In our demonstration, the message element takes the maximum value in Equation (14) instead of summation, for achieving better convergence efficiency. Therefore, the message element is:

$$\begin{aligned}
&\ell_{c_n \to u_k}(x_k = q) \triangleq p(x_k = q | r_n, \mathbf{x}^{[n]} \backslash x_k) \\
&= \max_{\substack{x_k = q \\ \mathbf{x}^{[n]} \in \mathbb{X}^{d_{c,n}}}} \left( \prod_{l \in \xi_n \backslash k} \ell_{c_n \leftarrow u_l}(x_l) \right) \cdot p\left( r_n | \mathbf{x}^{[n]} \right) \\
&p\left( r_n | \mathbf{x}^{[n]} \right) = \frac{1}{\sqrt{2\pi}\sigma} \exp\left( -\frac{1}{2\sigma^2} \left\| r_n - \mathbf{f}^{[n]T} \mathbf{x}^{[n]} \right\|^2 \right)
\end{aligned} \tag{16}$$

in which $d_{c,n}$ is the number of streams involved in $r_n$. Similarly, the message set sent from $u_k$ to $c_n$ will be the product of the messages received from edges $e_{m,k}, \forall m \in \zeta_k \backslash n$:

$$\boldsymbol{\ell}_{c_n \leftarrow u_k} = \left\{ \lambda_k \prod_{m \in \zeta_k \backslash n} \ell_{c_m \to u_k}(x_k = q), \forall q \in \mathbb{X}_k \right\} \tag{17}$$

in which $\lambda_k$ is chosen such that the sum of probabilities for all $q$ is 1. After the MPA converges or the number of iterations reaches a pre-set maximum, the probability of $x_k = q$ is:

$$p(x_k = q) = \lambda'_k \prod_{n \in \zeta_k} \ell_{c_n \to u_k}(x_k = q) \tag{18}$$

Finally, we have the estimation of $x_k$ as provided by the MPA:

$$\hat{x}_k = \arg\max_{q \in \mathbb{X}_k} p(x_k = q) \tag{19}$$

Let $d_C$ be the average number of superimposed streams in one RB, $|\mathbb{X}|$ be the average alphabet size, and $T_i$ be the number of iterations processed. Note that FN updates Equation (16) take the primary computation complexity, the complexity of MPA (the number of multiplication operations) is hence [42]:

$$O(T_i N d_C |\mathbb{X}|^{d_C}) \tag{20}$$

As a comparison, the complexity of SIC (the number of addition operation) is:

$$O(N|\mathbb{X}|^{d_C}) \tag{21}$$

MPA can achieve improved decoding efficiency with higher computational complexity. The complexity of MPA can be reduced by restricting the average number of superimposed streams at the same RB ($d_C$) or restricting the maximum number of iterations.

### *3.2.2 Experimental Setup*

The experimental setup is depicted in Figure 3.20. Two UEs access the RRU via mmWave uplinks and analog RoF mobile fronthaul. $K_i$ PDMA streams in $UE_i = \{s_{i,1}, s_{i,2}, \ldots, s_{i,K_i}\}$ are assigned to UEi. In the Tx-side DSP for each UEi, $K_i$ streams of bits are modulated to QAM symbols. Symbols within each stream use the same QAM order. QAM symbols are spread, scaled, and mapped to REs in accordance with the pattern matrix. Streams belonging to UEi are summed and go through conventional OFDM DSP. The subcarrier spacing is $2^7 \times 15kHz = 1.92MHz$ compliant with 5G standards. The FFT size is 2048, 420 out of which carry the payload. Subcarriers are partitioned and

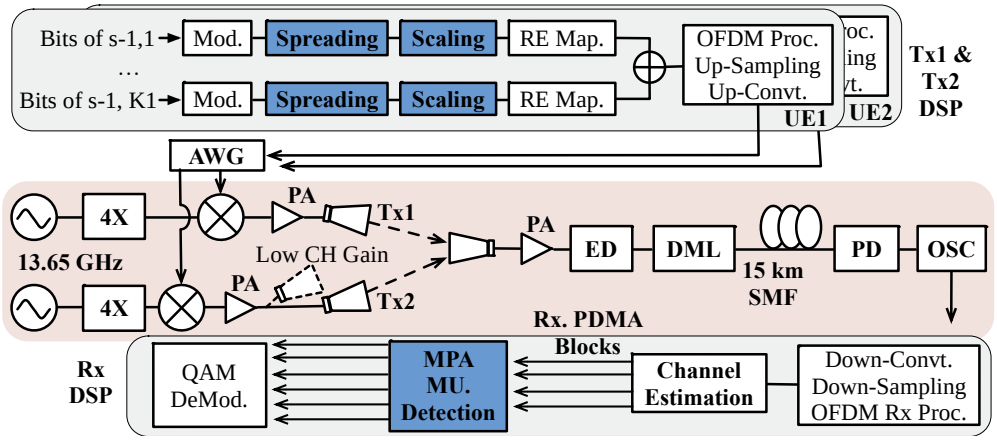


Figure 3.18 Experimental setup. © OSA 2020.

grouped in order to apply the pattern matrix. The intermediate frequency is 510MHz and the effective signal bandwidth is 806.4MHz.

The digital OFDM signal is converted to analog waveform via an AWG with sampling rate 15.7GSa/s. At each Tx, 54.59GHz carrier frequency is generated by a 13.65GHz RF source followed by a quadrupler. Each AWG output signal is upconverted to the RF carrier by a mixer. The synthesized mmWave signal is then each amplified a PA, transmitted by a horn antenna with 25dBi. The wireless transmission distance is 1.5m. At the Rx, another horn antenna captures both signals from the two UEs. The received signal is downconverted by an envelope detector (ED) (1GHz). The baseband electrical signal is then converted to the optical domain through a DML (2.5GHz). After transmission over 15km SMF, the signal is captured by a PD (2.5GHz) and input into an oscilloscope (5GSa/s) followed by offline DSP. At the Rx, the received signal goes through preliminary OFDM demodulation and channel estimation which is essential for MPA detection. Received symbols are re-organized into resource blocks in accordance with the pattern matrix. MPA is applied to every received block to recover $K_i$ streams of QAM symbols which are then decoded to $K_i$ bit streams for BER calculation. To investigate how PDMA can be tailored to support different application scenarios, the channel gain of Tx2 is varied during the experiments. In some experimental cases, $UE_2$ will experience low channel gain, controlled by the AWG output power of Tx2.

### *3.2.3 Experimental Results*

Four categories of experiments were carried out to verify the performance of PDMA with MPA: i) Comparison of MPA and SIC; ii) the flexibility of PDMA with

different pattern matrices and channel conditions; iii) PDMA for grant-free uplinks (case A); iv) PDMA for data transmission under channel degradation (case B). In the experiments, BER versus ROP at the PD was measured and analyzed.

### 3.2.3.1 Comparison of MPA and SIC

The PDMA parameters used in the experiment are the same as those in case A illustrated in section 3.2.1.1, Figure 3.16(a), in which $UE_1 = \{1, 4, 5\}$ and $UE_2 = \{2, 3, 6\}$. The channel gain for UE$_1$. and UE$_2$ is on the same level, i.e., $|\mathbf{H}_{UE1}|^2 \simeq |\mathbf{H}_{UE2}|^2$. In the experiment, SIC is evaluated and compared to MPA. In SIC, the stream with higher power level will be decoded first. For example, for the received symbol $r_1$, $\hat{x}_3$ will be decoded first and then subtracted for the decoding of $\hat{x}_1$. Figure 3.19(a) selects streams with the best (from streams with high power level) and worst (from streams with low power level) BER performance, both in B2B and after transmission over 15km SMF. Experimental results show that MPA detection can achieve an approximate 4dB Rx sensitivity improvement at 7% HD-FEC threshold compared to SIC, providing 1.9Gbp for each UE.

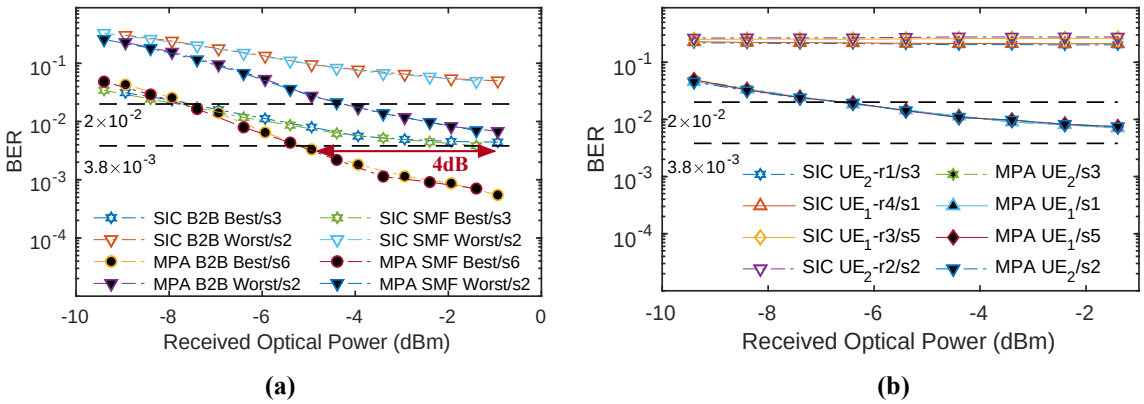


Figure 3.19 (a) Comparison of MPA and SIC. (b) Comparison of the BER of MPA and SIC when constellation ambiguity occurs. © OSA 2020.

At 20% soft-decision FEC (SD-FEC) threshold, the improvement of MPA for steams with the best BER performance is limited. In this region, the system is mainly restricted by bad SNR. MPA achieves enhanced decoding performance owing to information passed and verified over the factor graph, the accuracy of which is essentially built on the error rate of each node. At around the 20% SD-FEC limit, the error rate of each node is already high, resulting in the degraded performance of MPA.

The performance of MPA and SIC under constellation ambiguity is also evaluated. The pattern matrix and user-stream assignment is the same as those used in Figure 3.19(a). In the legend, '$r_1/s3$' corresponds to the measured BER in the presence of $s3$ in the received symbol $r_1$ during SIC detection. The modulation of all streams is QPSK, i.e., $bpS = [2\ 2\ 2\ 2\ 2\ 2]$, the stream amplitude tuning is $\boldsymbol{a} = [0\ 0\ 0\ 0\ 0\ 0]\ dB$, and the channel condition is $|\mathbf{H}_{UE1}|^2 \simeq |\mathbf{H}_{UE2}|^2$ . With such parameter setting, the constellation ambiguity will occur as indicated in Figure 3.16(e). It can be seen from Figure 3.19(b) that SIC is not able to differentiate ambiguous symbols with BER value all beyond 7% HD-FEC threshold, whereas MPA can achieve acceptable BER performance with high ROP.

#### 3.2.3.2 Flexibility Provided by PDMA

PDMA can be easily adapted to meet requirements of different bit rate, interference level, and reliability, owing to the tunability of the pattern matrix and stream amplitude/phase tuning. In this category of experiments, different pattern matrices are firstly investigated. Figure 3.20 shows two scenarios supported by different pattern matrices: $P_A$ (section 3.2.1.1, Figure 3.16(a)) and $P_C$ (section 3.2.1.2, Figure 3.17). In the legend, 'H'/'L' corresponds to the streams with high(H)/low(L) amplitudes. The user-stream

allocation, stream amplitudes, modulation order, and channel condition of Figure 3.20(a) are the same as case A. Whereas the parameters used in Figure 3.20(b) are: $UE_1 = \{1, 2, 3\}$ and $UE_2 = \{4, 5, 6\}$ , $\boldsymbol{a} = [7\ 7\ 0\ 7\ 7\ 0]\ dB$ , $bpS = [2\ 2\ 2\ 2\ 2\ 2]$ , and $|\mathbf{H}_{UE1}|^2 \simeq |\mathbf{H}_{UE2}|^2$. $P_C$ has the same matrix size as $P_A$ (4x6) but has higher average diversity. The symbol of every stream in $P_C$ is spread twice, resulting in better decoding reliability at the cost of reduced data rates of $s3$ to $s6$. Consequently, PC has better overall BER performance in comparison to $P_A$ as shown in Figure 3.20(b) and (a).

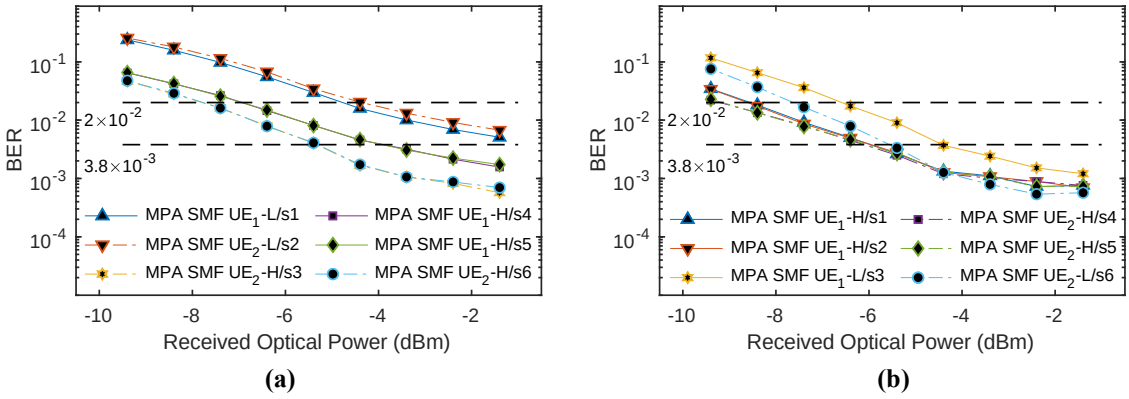


Figure 3.20 Comparison of two pattern matrices: (a) $P_A$ and (b) $P_C$. © OSA 2020.

We also investigate the capability of PDMA handling varied channel qualities. In the experiment, we use the same PDMA setting as case B in section 3.2.1.1, Figure 3.16(b), but with varied user channel qualities. In Figure 3.21(a), $|\mathbf{H}_{UE1}|^2 \simeq |\mathbf{H}_{UE2}|^2 + 7dB$; in Figure 3.21(b), $|\mathbf{H}_{UE1}|^2 \simeq |\mathbf{H}_{UE2}|^2$. From Figure 3.21(a) to (b), BER degradation can be observed due to the increased interference from $UE_2$ to $UE_1$ which causes it to approach constellation ambiguity. Owing to MPA, the UEs can maintain BER below threshold given channel gain varying over 7dB, without changing the PDMA Tx-side setting.

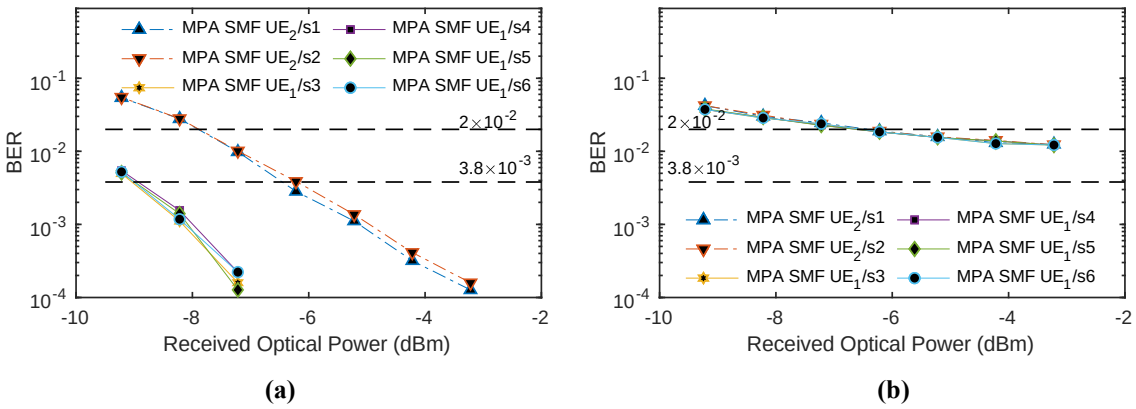


Figure 3.21 BER vs. ROP performance when $UE_1$ and $UE_2$ have the same Tx PDMA setting, with varied channels: (a) $|\mathbf{H}_{UE1}|^2 \simeq |\mathbf{H}_{UE2}|^2 + 7dB$; (b) $|\mathbf{H}_{UE1}|^2 \simeq |\mathbf{H}_{UE2}|^2$. © OSA 2020.

From the experimental results shown in Figure 3.19 to Figure 3.21, the BER performance of PDMA can be affected by stream amplitude/phase tuning and pattern matrix design, which provides more configuration flexibility, in addition to the improved system turbulence immunity provided by MPA.

Similar to other NOMA schemes, PDMA stacks multiple symbols in one RE. The decodability of the system is dependent on the signal to noise and interference ratio which is determined by system SNR and number of users. Provided with higher SNR, one RE can be shared by more users. On the other hand, the system can support more users if lower modulation order is applied. For example, the system SNR can support the co-transmission of a QPSK symbol and a 16QAM symbol from two users at one RE (Figure 3.19), as well as the co-transmission of three QPSK streams (Figure 3.20(b)) using pattern matrix $P_C$. In our demonstration, a two-user scenario is implemented given two sets of Tx available at mmWave frequencies, in which each user is assigned multiple streams. In applications without the device limitation, one stream can correspond to one user, which can support

increased number of users. The total number of users is dependent on achievable SNR, modulation order used, and the design of PDMA pattern matrix.

### 3.2.3.3 PDMA for Grant-Free Uplinks

As illustrated in case A, $UE_1 = \{1, 4, 5\}$, among which *s*1 with lower amplitude level is pre-assigned for grant-free uplinks and stacked onto normal data of *s*3 and *s*6 that are sharing the same REs. Figure 3.22(a) verifies that both grant-free uplinks and normal data transmission can be supported by PDMA with BER of all six streams below the FEC threshold when ROP > -4dBm. To investigate how interference from grant-free uplinks affects normal data transmission, the BER of PDMA-MPA, PD-NOMA-SIC, and interference-free OFDM were evaluated. As shown in Figure 3.22(b), the BER of the streams with high power for normal data transmission are compared with interference-free OFDM streams. It can be seen that at ROP = -4dBm, for $UE_1$ the BER of OFDM is around $10^{-4}$, the BER of PDMA stream degrades to approximately $10^{-3}$, whereas the BER of PD-NOMA-SIC drops to about $3.8\text{x}10^{-3}$. Owing to the improved decoding accuracy of MPA,

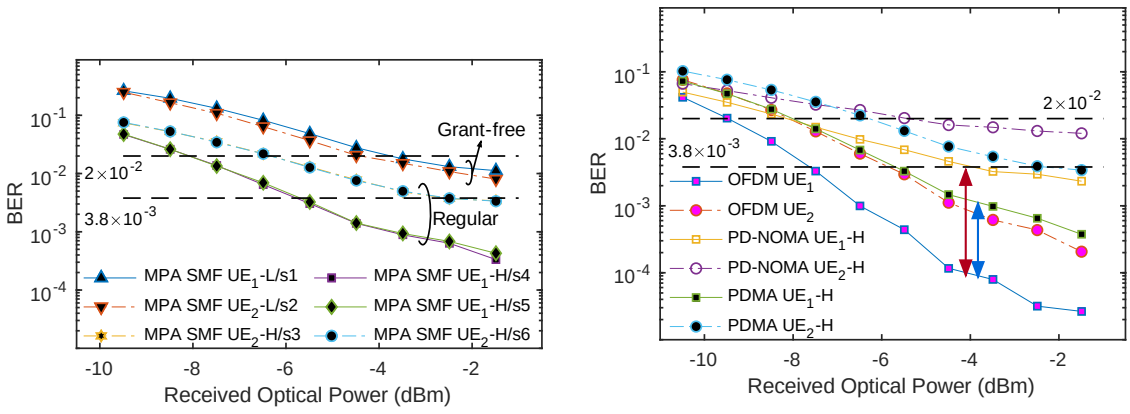


**(a)** **(b)**

Figure 3.22 Experimental results of case A: (a)BER vs. ROP; (b) Penalty of PDMA and PD-NOMA-SIC compared to interference-free OFDM. © OSA 2020.

the penalty from the grant-free uplinks supported by PDMA is mitigated compared to that of PD-NOMA-SIC.

#### 3.2.3.4 PDMA for Data Transmission under Channel Degradation

As mentioned in the introduction, OMA such as OFDMA has to trade off spectral efficiency when some of the users are experiencing low-SNR channels. In this experiment, the performance of PDMA, OFDM, and PD-NOMA under low-SNR channels is analyzed and compared. Throughout the experiment, the channel of $UE_1$ was fixed with good channel quality, while the channel of $UE_2$ was set such that $|\mathbf{H}_{UE1}|^2 \simeq |\mathbf{H}_{UE2}|^2 + 6dB$. The pattern matrix and user-stream allocation that were implemented are shown in Figure 3.23. The modulation order applied is the highest order that the corresponding access scheme can support such that BER is below the FEC threshold. 4x4 and 4x8 matrices are implemented for OFDM and PD-NOMA, respectively, as two special cases of pattern matrices.

The BER of OFDM, PD-NOMA-SIC, and PDMA-MPA is shown in Figure 3.23(a), (b), and (c), respectively. For OFDM, $UE_1$ with good SNR can transmit 64QAM, whereas $UE_2$ under channel degradation barely supports QPSK. The modulation spectral efficiency of OFDM is therefore $(6 \times 2 + 2 \times 2)/4 = 4\ bits/symbol$. For PD-NOMA with SIC, $UE_1$ and $UE_2$ share the same REs using QPSK, the signal strength of $UE_2$ is around 6dB less than $UE_1$ at the receiver. The average modulation spectral efficiency of PD-NOMA with SIC is: $(2 \times 4 + 2 \times 4)/4 = 4\ bits/symbol$, which is the same as OFDM in this case but with improved average BER of $UE_2$. In PDMA with MPA, 16QAM can be implemented for $UE_1$ due to the enhanced decoding accuracy. The average modulation spectral

efficiency is $(2 \times 2 + 4 \times 4)/4 = 5\ bits/symbol$, outperforming both OFDM and PD-NOMA. Figure 3.23(d) summarizes the experimental results of all three access schemes. It can be seen that PDMA can achieve higher modulation spectral efficiency with better BER performance compared to PD-NOMA-SIC when provided with ROP > -3dBm, validating the potential to support dynamic mmWave links in future-proof RANs.

$P_{OFDM}^{[4,4]} =$

| UE1 | | UE2 | |
|---|---|---|---|
| $s1$ | $s2$ | $s3$ | $s4$ |
| 1 | 0 | 0 | 0 |
| 0 | 1 | 0 | 0 |
| 0 | 0 | 1 | 0 |
| 0 | 0 | 0 | 1 |

$bpS =$ [ 6 6 2 2 ]

$P_{PD-NOMA}^{[4,8]} =$

| UE2 | | | | UE1 | | | |
|---|---|---|---|---|---|---|---|
| $s1$ | $s2$ | $s3$ | $s4$ | $s5$ | $s6$ | $s7$ | $s8$ |
| 1 | 0 | 0 | 0 | 1 | 0 | 0 | 0 |
| 0 | 1 | 0 | 0 | 0 | 1 | 0 | 0 |
| 0 | 0 | 1 | 0 | 0 | 0 | 1 | 0 |
| 0 | 0 | 0 | 1 | 0 | 0 | 0 | 1 |

$bpS =$ [ 2 2 2 2 2 2 2 2 ]

$P_{PDMA}^{[4,6]} =$

| UE2 | | | UE1 | | |
|---|---|---|---|---|---|
| $s1$ | $s2$ | $s3$ | $s4$ | $s5$ | $s6$ |
| 1 | 0 | 1 | 0 | 0 | 0 |
| 0 | 1 | 0 | 1 | 0 | 0 |
| 0 | 1 | 0 | 0 | 1 | 0 |
| 1 | 0 | 0 | 0 | 0 | 1 |

$bpS =$ [ 2 2 4 4 4 4 ]

$$|\mathbf{H}_{UE1}|^2 \simeq |\mathbf{H}_{UE2}|^2 + 6dB$$

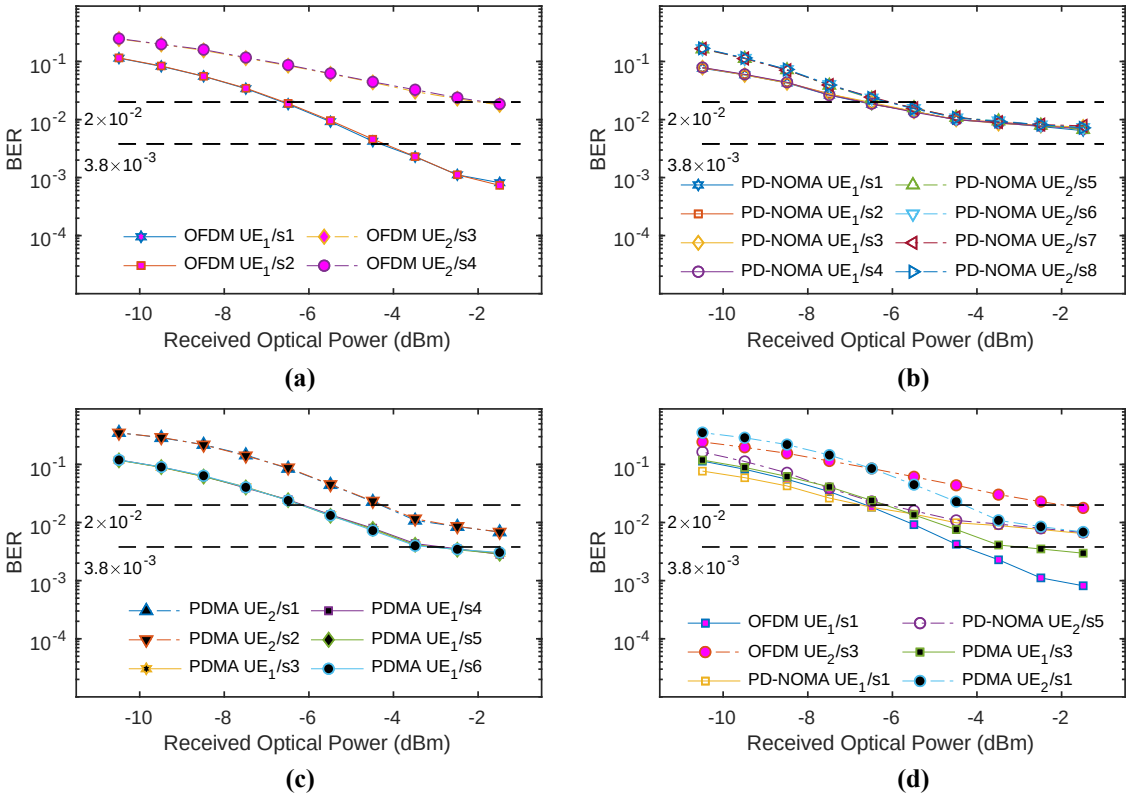


Figure 3.23 BER of case B when $|\mathbf{H}_{UE1}|^2 > |\mathbf{H}_{UE2}|^2$, supported by (a) OFDM; (b) PD-NOMA-SIC; (c) PDMA-MPA. (d) Comparison of (a), (b), and (c). © OSA 2020.

### *3.2.4 Summary*

The integration of PDMA with MPA has been proposed and applied to mmWave radio access systems using RoF mobile fronthaul. Through the selection and implementation of the pattern matrix, user-stream allocation, and stream amplitude/phase tuning, PDMA can provide improved access flexibility to cope with dynamic channel conditions of mmWave links. Moreover, PDMA stands out among conventional NOMA schemes with enhanced decoding accuracy provided by MPA. Using modified MPA process with improved convergence efficiency, our experimental demonstration of PDMA attained a 4dB sensitivity improvement and proved the capability of recovering ambiguous symbols, in comparison with PD-NOMA-SIC. It is verified that PDMA can provide configuration flexibility, by evaluating the performance of PDMA with different pattern matrices and channel qualities. Furthermore, the ability of PDMA to support grant-free uplinks has been experimentally demonstrated to provide reduced BER penalty at the receiver compared to PD-NOMA-SIC. It is also verified that PDMA is capable of providing higher modulation spectral efficiency when part of the users in the system are limited by low-SNR channel qualities. To summarize, PDMA integrated with MPA has been systematically demonstrated and it has shown the potential to support future-proof mmWave-based radio access networks.

# CHAPTER 4 DRL-BASED SCHEDULING OPTIMIZATION

In previous chapters, PHY layer technologies are introduced to optimize the performance of RoF-based fiber-wireless networks. In this chapter, we broaden the focus to cover the scheduling involving both PHY and MAC layers. This chapter presents the work to utilized DRL to optimize the scheduling and resource utilization in mmWave-RoF RANs. Specifically, a DRL-based resource allocation algorithm with channel condition and latency awareness is demonstrated. The proposed scheme aims to optimize the uplink scheduling for service-oriented multi-user mmWave RANs in 5G era. This chapter is organized as follows. Challenges of scheduling in mmWave-RoF RANs and the proposed solution are introduced in section 4.1. Section 4.2.1 introduces the framework and design of the DRL algorithm with illustration of the scheduling process. The system architecture is illustrated in section 4.2.2, with implementation details of the component modules. In particular, the mmWave channel demonstration is presented in section 4.2.2.3 as well. The evaluation of the DRL system and results are analyzed and discussed in section 4.2.3, which covers the DRL training process and the performance comparison with conventional schemes.

## 4.1 Challenges of Scheduling in mmWave-RoF RAN

The 5G NR RANs are envisioned to be service-oriented, supporting multiple users and various applications with different quality-of-service (QoS) requirements [8]. In addition to capacity and speed requirements, latency becomes an important performance benchmark, especially for time-sensitive data traffic. Applications such as video streaming, low-latency gaming, and real-time services including robotic control, intelligent factories,

tele-health will have different delay and reliability requirements [70]. As a result, for simple pre-scheduling or fixed radio resource allocation schemes used in legacy wireless communication networks, it will be challenging to manage the increased QoS complexity while providing operational flexibility and efficiency.

Currently, mmWave links are implemented for 5G RANs, which can result in dynamic channel conditions that add to the complexity of radio resource management (RRM) [71]. Although mmWave can provide wide bandwidth and high capacity, it is subject to less diffraction in beam propagation, high Friss path propagation loss and atmospheric absorption loss. In outdoor environments, such mmWave links can experience abrupt signal strength variations due to rain drops or moving pedestrians or vehicles [72]. Whereas inside a smart factory, mmWave links are susceptible to LoS blockages caused by moving robots or stock boxes. Considering both complex QoS objectives and dynamic channel conditions, the needs of agile and adaptive radio resource scheduling and allocation are urgently anticipated in 5G and beyond RANs.

To tackle the challenges, many results have been reported to develop intelligent radio resource allocation and scheduling. In [73], DRL is utilized to optimize resource block (RB) allocation in a mmWave mobile backhaul. In the work, capacity is the optimization objective and the DRL action is the direct RB allocation and user mapping, which can be extremely complicated if the RB space scales up. In [74], Markov decision process (MDP) is used to model the operations of a mobile edge computing (MEC) system. Considering random task arrivals and channel state variations, the method can optimize power consumption while meeting the latency requirements. However, only single user is considered in the work, which is not sufficient because multi-user contention and management are required to solve the scheduling problem. In [75], the authors implement deep deterministic policy gradient (DDPG) for radio resource scheduling in a 5G RAN, taking multiple users, varied channel conditions, and random traffic arrivals into account.

BER and delay are jointly considered. The limitation of the work is that only *Poisson* distribution is used to model the arrival patterns of UE, despite the diverse application arrival patterns in reality.

Figure 4.1 is the schematic diagram of the system. The system will consider multi-user multi-service scenarios with different QoS requirements, to jointly optimize BER and latency. Furthermore, the system takes channel dynamics into account by varying mmWave link conditions including LoS and NLoS blockages. Channel characteristics in this work are experimentally obtained via mmWave-RoF testbed and then implemented in the DRL system. Based on the provided state information which includes service queue status, application request patterns and priority levels, as well as channel quality indicators, the DRL-based scheduler will make the decision action to choose the optimal scheduling and resource allocation rule.

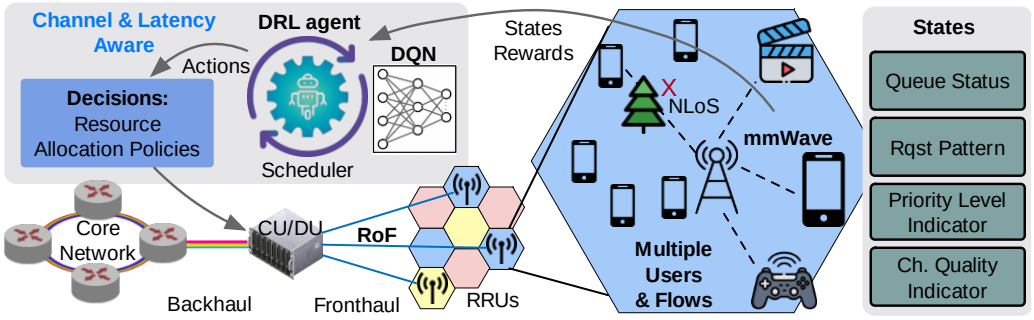


Figure 4.1 System architecture in a 5G environment. © OSA 2021.

The main contributions of the work are summarized as follows. Firstly, we establish a DRL framework for joint BER and latency optimization for time-sensitive traffic in a service-oriented 5G system subject to dynamic mmWave channel conditions. Different statistical models are implemented for the arrival intervals and packet sizes of diverse applications. Conventional request-grant cycles of the uplink scheduling process are implemented, taking into account possible congestion and queuing delay under heavy

traffic load. We design and formulate the state and reward of the DRL scheduler such that it will reflect queue status, channel variation, and service-customized latency performance based on 3GPP QoS requirements. Secondly, in our preliminary work [12], direct RB allocation mapping to UE is implemented as DRL actions. Through our investigation, we find that such straightforward action design can cause extreme complexity and require huge computational resource if used in a multi-user wideband mmWave RAN. Therefore, re-design of the action is required to improve convergence efficiency. The action of the proposed DRL-based scheduler is to select the optimal resource allocation rule for the current TTI. A similar scheme is also adopted in [75]. Thirdly, in contrast to most of the previous DRL-related works with only simulation results, the mmWave channel characteristics utilized in the proposed system are experimentally obtained and verified via a mmWave testbed with RoF-enabled mobile fronthaul. In this work, photonic-assisted mmWave generation is implemented to achieve wide-bandwidth transmission and experimentally verified channel variations. To realize the dynamic channel conditions of mmWave links such as reflection, blockage, and reduced transmission power, channel variation is introduced in the scheduling process. This work has been accepted by *Optical Fiber Conference (OFC) 2021* [76].

## 4.2 DRL-Based Channel and Latency Aware Radio Resource Allocation

### *4.2.1 Scheduling Process and DRL System Design*

We consider the uplink transmission of a mmWave remote RRU supported by RoF mobile fronthaul as shown in Figure 4.1. The system is flow-oriented and involves multiple

UEs that are using applications with different QoS requirements and experiencing different channel conditions. One UE can have multiple active services/flows simultaneously.

The scheduling process follows the request-grant cycles that are widely implemented in mobile communication networks, which is depicted in Figure 4.2. A general introduction of the process is presented in section 1.2.4. In this system, upon receiving the uplink data the scheduler will check the pre-forward-error-correction (pre-FEC) BER of the received data which determines whether re-transmission (Re-Tran) is required as illustrated in Figure 4.2. In a real system, the scheduler may send HARQ or NACK accordingly. For simplicity, the queuing delay is considered only for the original data transmission, while not for the re-transmission, i.e., guaranteed resources for re-transmissions are assumed in the system.

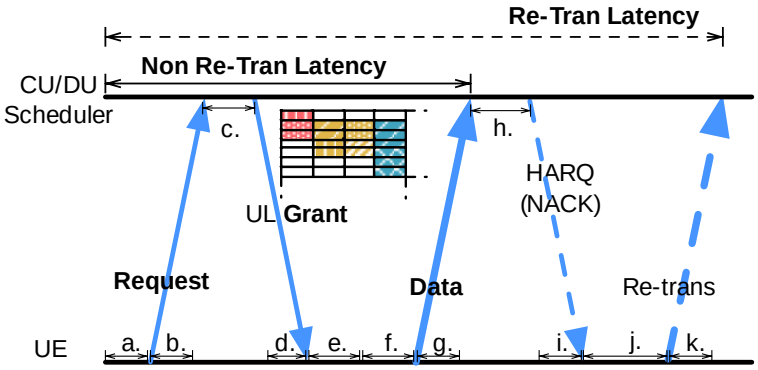


Figure 4.2 Uplink scheduling process: request-grant cycle in a RAN. © OSA 2021.

Let $\mathcal{U} = \{1, 2, \ldots, U\}$ denotes the set of UEs and $\mathcal{F} = \{1, 2, \ldots, F\}$ denotes the set of flows. *F* is the total number of flows and *U* is the total number of UEs. One UE can have multiple active flows. If a flow $f \in \mathcal{F}$ belongs to a UE $u \in \mathcal{U}$ then $v(f) = u$, indicating the corresponding UE *u* of flow *f*. $\mathcal{B} = \{1, 2, \ldots, B\}$ is the set of resource groups (RG) for allocation. RG is grouped RBs sharing the same modulation order, the design of which will

be explained in section 4.2.2.3. The total number of RGs is *B*. At TTI *t*, the capacity of the RG $b \in \mathcal{B}$ corresponding to flow *f* is $C_{f,b}(t)$, as different UEs have different channel conditions. Actually, $C_{f,b}(t)$ is determined by $C_{u,b}(t)$ given the flow to UE mapping. Similarly, $E_{f,b}(t)$ denotes the BER of the RG *b* corresponding to *f*, which will be calculated from the experimentally measured EVM.

In the flow-oriented system, different flows will have different packet sizes and arrival intervals. At TTI *t*, the requested data size of flow *f* is $Y_f(t)$. The requested packets will be stored in the corresponding queue. At TTI *t*, the queue length of flow *f* is $Q_f(t)$, which is determined by the queue length of the last TTI (*t-1*), the new arrival of requests $Y_f(t)$, and the granted data size $G_f(t)$ at this TTI:

$$Q_f(t) = Q_f(t-1) + Y_f(t) - G_f(t) \tag{22}$$

in which $G_f(t) \leq (Q_f(t-1) + Y_f(t))$. The granted data size of each flow is determined by the resource allocation scheme, which can be calculated by:

$$G_f(t) = \sum_{b=1}^{B} x_{f,b}(t) \cdot C_{f,b}(t) \tag{23}$$

where $x_{f,b}(t)$ is the allocation indicator. $x_{f,b}(t) = 1$ if flow *f* is assigned with RG *b* at TTI *t*, otherwise $x_{f,b}(t) = 0$. The unit of $C_{f,b}(t)$, $Q_f(t)$, $Y_f(t)$, and $G_f(t)$ is the unit RG capacity.

Let $N_f(t)$ denote the number of packets of flow *f* that has been requested from *t*=1 to *t*. $N_f$ denotes the total number of requested packets of flow *f*. $E_f(j)$ denotes the received pre-FEC BER of packet *j* from flow *f*. The pre-FEC BER threshold of flow *f* is $ET_f$.

Packets with $E_f(j) > ET_f$ will be re-transmitted, which will cause extra delay. $m_f(t)$ is the number of latency-satisfied packets from flow *f* at TTI *t*, which are scheduled packets with the overall latency satisfying the delay budget requirement $D_f$. Therefore, the total number of latency-satisfied packets of flow *f* will be $M_f = \sum_{t=1}^{T} m_f(t)$.

#### 4.2.1.1 Problem Formulation

The objective of the system is to optimize the mmWave resource allocation and scheduling so that the average ratio of latency-satisfied packets ($\frac{M_f}{N_f}$) will be maximized. To facilitate the DRL reward design which will be discussed in section 4.2.1.3, here the harmonic mean $\mathcal{H}(\frac{M_f}{N_f})$ is considered. Different from the arithmetic mean widely used, the harmonic mean tends to emphasize the impact of small outliers [77], which is desired in a scheduling problem as we want to avoid flows with very low ratio of latency-satisfied packets.

We formulate the problem as follows:

$$\max_{x_{f,b}(t)} \mathcal{H}(\frac{M_f}{N_f}) = (\frac{1}{F}\sum_{f=1}^{F}(\frac{M_f}{N_f})^{-1})^{-1} \tag{24}$$

$$s.t. \quad x_{f,b}(t) \in \{0,1\}, \forall f, b, t \tag{25}$$

$$\sum_{f=1}^{F} x_{f,b}(t) \leq 1, \forall b, t \tag{26}$$

where Equation (25) shows that RG assignment variables are binary, and Equation (26) suggests that each RG can only be assigned to one flow. The solution of Equation (24) aims

to find the best resource allocation at each TTI for all flows and RGs. This problem is difficult for the following reasons: i) constraints Equation (25) and (26) makes the problem combinatorial; ii) the number of RGs and the number of flows can be very large, which makes the optimization problem more challenging; iii) the objective does not have closed form expressions in terms of $x_{f,b}(t)$. A direct optimization is difficult. To solve ii) and iii), instead of directly deciding $x_{f,b}(t)$, the action of the proposed DRL-based scheduler is modified to select the optimal scheduling and resource allocation rule for each TTI, which will determine $x_{f,b}(t)$ with different scheduling objectives. Let $\mathcal{P} = \{p_1, p_2, \ldots, p_y\}$ denote the set of candidate rules. At TTI *t*, the selected rule is $P(t) \in \mathcal{P}$. The problem becomes:

$$\max_{P(t)} \left(\frac{1}{F}\sum_{f=1}^{F}\left(\frac{M_f}{N_f}\right)^{-1}\right)^{-1} \tag{27}$$

with $P(t)$ satisfies constraints Equation (25) and (26).

#### 4.2.1.2 DRL Framework

In (22), the queue length of flow *f* at TTI *t* is determined by the queue length of the last TTI $Q_f(t-1)$, the requested data $Y_f(t)$, and the granted data size $G_f(t)$. The scheduler will make the decision based on observation of channel conditions, queue status, and request patterns to meet QoS requirements. The decision making is partly random due to the arrival request patterns and partly dependent on the available resource allocation rules in the scheduler. Therefore, the queue state (22) can be modeled as a Markov decision process (MDP) [12]. We use Q-learning algorithm, the most widely used reinforcement learning method, to solve the MDP problem. Considering the large number of RGs and

flows, dynamic optimization environment and targets, a deep neural network (DNN) is used in the proposed system instead of conventional Q-table. The deep Q network (DQN) will be trained to reflect the mapping between the state and action spaces during the DRL process.

In the proposed DRL-based scheduling algorithm, we define the period of time in which the interaction between the agent and the environment takes place as an episode, and each TTI *t* corresponds to a step of an episode. The state space of flow *f* at TTI *t* includes the head-of-line (HoL) latency of the top packet in the queue, denoted by $s_{f,1}(t)$; the requested data size $s_{f,2}(t) = Y_f(t)$; the flow priority indicator $s_{f,3}$ and the capacity (spectral efficiency) of all RGs $\mathbf{s}_{f,4}(t) = \{C_{f,b}(t), \forall b\}$. The state at *t* can be expressed as:

$$\mathbf{s}(t) = \{\mathbf{s}_1(t), \mathbf{s}_2(t), \ldots, \mathbf{s}_F(t)\} \tag{28}$$

where $\mathbf{s}_f(t)$ is the observed state of flow *f*:

$$\mathbf{s}_f(t) = \{s_{f,1}(t), s_{f,2}(t), s_{f,3}, \mathbf{s}_{f,4}(t)\} \tag{29}$$

From Equation (28) and (29), the size of $\mathbf{s}(t)$ will be *3F + BF*. Or if we consider one UE may have multiple flows, the size of $\mathbf{s}(t)$ will be *3F + BU*. The state size is dependent on the number of RGs and UEs, from which is can be seen the computational complexity increases with available bandwidth resources and the number of users.

In our previous work of DRL scheduler which aims to optimize delay with a small RB space) [12], the action is defined as the choice of $x_{f,b}(t)$. In this case, the size of action space will be $|\mathcal{A}| = F^B$ which will be extremely large in a multi-flow wideband system. As analyzed in section 4.2.1.1, to cope with the large RG space and the service-oriented

QoS requirements in 5G, the action space $\mathcal{A}$ in the proposed scheduler consists of resource allocation rules that have been widely investigated and implemented by network designers with different scheduling targets, i.e., $\mathcal{A} = \mathcal{P}$. The size of the action space reduces to $|\mathcal{A}| = |\mathcal{P}|$, which are independent of *B* and *F*, therefore improving the convergence efficiency.

In the learning process, the DQN agent will maintain a critic NN $Q(s, a)$, which takes observation of state $\mathbf{s}(t)$ and action $a(t)$ as inputs and returns the corresponding expectation of the long-term reward:

$$Q(\mathbf{s}(t), a(t) \mid \theta_Q) = \mathbb{E}\left[\sum_{i=0}^{\infty} \gamma^i r(t+i) \mid \mathbf{s}(t), a(t)\right] \tag{30}$$

where $r(t+i)$ is the instantaneous reward, $\gamma$ is the discount factor, and $\theta_Q$ represents the parameter values of the DQN. The long-term reward is:

$$R(t) = \sum_{i=0}^{\infty} \gamma^i \cdot r(t+i) \tag{31}$$

The training and testing algorithm is illustrated in algorithm 1. $Q(s, a)$ is initialized with random parameters $\theta_Q$ and will periodically update over the training process as it interacts with the environment. At each step or TTI *t*, with probability $\epsilon$ which updates with decay rate *d*, the system will randomly generate an action, otherwise it will observe the current state and select the action with the greatest Q-value:

$$a(t) = \underset{a(t) \in \mathcal{A}}{\arg\max}\ Q\left(\mathbf{s}(t), a(t) \mid \theta_Q\right) \tag{32}$$

After taking a certain action, the system calculates the instantaneous reward $r(t)$ and observes the next state $\mathbf{s}'$. The transition experience $(\mathbf{s}(t), a(t), r(t), \mathbf{s}')$ will be stored in a replay memory $\mathcal{K}$. After that, a random minibatch of $K$ experiences will be selected for the optimization and update of $\theta_Q$.

**Algorithm 1** BER and delay aware scheduling algorithm based on DRL

**if** training **then**
    Initialize environment and generate traffic patterns
    Initialize the time, states, action and replay buffer $\mathcal{K}$
    **for** each episode **do**
        **for** each TTI $t$ **do**
            Load the status of the RGs
            Observe state $\mathbf{s}(t)$ as shown in (28)
            $\epsilon = \max(\epsilon \cdot d, \epsilon_{\min})$
            Sample $r \sim \mathcal{U}(0,1)$
            **if** $r \leq \epsilon$ **then**
                select an action $a(t) \in \mathcal{A}$ randomly
            **else**
                Select an action $a(t)$ using (32)
            **end if**
            Compute the reward $r(t)$
            Observe the next state $\mathbf{s}'$
            Store the experience $(\mathbf{s}(t), a(t), r(t), \mathbf{s}')$ in $\mathcal{K}$
            From $\mathcal{K}$, sample a random minibatch of $K$ experiences: $\{e_k \equiv (\mathbf{s}_k, a_k, r_k, \mathbf{s}'_k)\}$.
            Set $y_k = r_k + \gamma \max_{a'} Q(\mathbf{s}'_k, a' \mid \theta_Q), \forall k$
            Perform the gradient optimization on loss $L = \frac{1}{K}\sum_{k=1}^{K}(y_k - Q(\mathbf{s}_k, a_k \mid \theta_Q))^2$ to get the optimal $\theta_Q^*$
            Update $\theta_Q$ from $\theta_Q^*$, with the target method
            $t = t + 1$
            $\mathbf{s}(t) = \mathbf{s}'$
        **end for**
    **end for**
    save $\theta_Q$ and the agent
**else**
    Load the agent
    Observe the state and output the action using (32)
**end if**

#### 4.2.1.3 Reward Design

One key step of DRL design is to customize the reward function for the desired target. In this work, the problem is to optimize Equation (27) with restrictions Equation (25) and (26). The reward of the DRL system is designed as follows. At each TTI *t* for each flow *f*, all packets that have been requested will be categorized to four types as depicted in Figure 4.3. For flow *f* at TTI *t*, the total number of requested packets is $N_f(t)$; for those packets that have been scheduled, the total number of scheduled packets whose latency satisfies the service latency requirement $D_f$ is $M_f(t)$, the total number of packets whose latency exceeds $D_f$ is $L_f(t)$; for the packets in the queue waiting to be scheduled, the total number of packets whose queuing time already exceeds delay budget $D_f$ is $W_f(t)$. The reward of flow *f* at TTI *t* is defined as:

$$r_f(t) = 1 - \frac{L_f(t)}{M_f(t)} - \frac{2W_f(t)}{M_f(t)} \tag{33}$$

In Equation (33), the second term $-\frac{L_f(t)}{M_f(t)}$ reflects negative feedback if the current scheduling method has resulted in too much latency, whereas the third term $-\frac{2W_f(t)}{M_f(t)}$ with the weight factor 2 indicates more significant negative feedback to prevent latency-failure packets from queuing up and leading to large queuing delay. In Equation (33), $M_f(t)$ rather than $N_f(t)$ is used for the denominator to reduce the influence of random packet arrival, therefore the reward can better reflect the scheduling efficiency. mmWave channel conditions can influence the reward as poor BER will lead to re-transmissions which will

cause extra latency. The overall reward of TTI *t* is the weighted sum of $r_f$:

$$r(t) = \frac{1}{F}\sum_{f=1}^{F} r_f(t) \tag{34}$$

At the end of the scheduling process, the third term in Equation (33) will vanish as all packets are processed ($W_f = 0$):

$$r = \frac{1}{F}\sum_{f=1}^{F} r_f = \frac{1}{F}\sum_{f=1}^{F}(1 - \frac{L_f}{M_f}) \tag{35}$$

With all packets scheduled, we have $L_f = N_f - M_f$, then Equation (35) is equal to:

$$\begin{aligned} r &= \frac{1}{F}\sum_{f=1}^{F}(1 - \frac{N_f - M_f}{M_f}) \\ &= \frac{1}{F}\sum_{f=1}^{F}(2 - \frac{N_f}{M_f}) \\ &= 2 - \frac{1}{F}\sum_{f=1}^{F}(\frac{M_f}{N_f})^{-1} \end{aligned} \tag{36}$$

When Equation (36) is maximized, Equation (27) is maximized accordingly, which complies with the optimization objective.

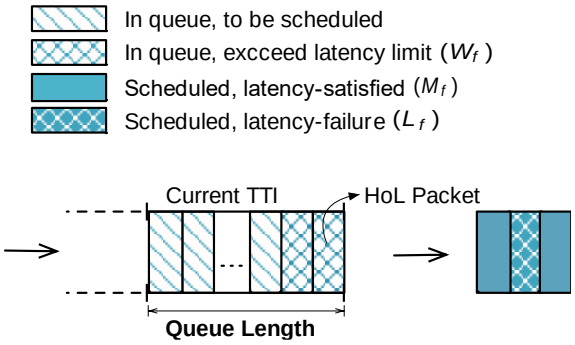


Figure 4.3 Illustration of packet and queue status. © OSA 2021.

### *4.2.2 Operation Implementation*

The mmWave radio access network testbed with DRL-based scheduler consists of several key function modules as shown in Figure 4.4. The directions of arrows in Figure 4.4 indicate the processing flow in an episode that follows the request-grant cycle. The delays of different stages in the scheduling process indicated in Figure 4.2 are summarized in Table 4-1. The delay parameters are based on [80], in which 2km standard SMF and 50m wireless distance is assumed.

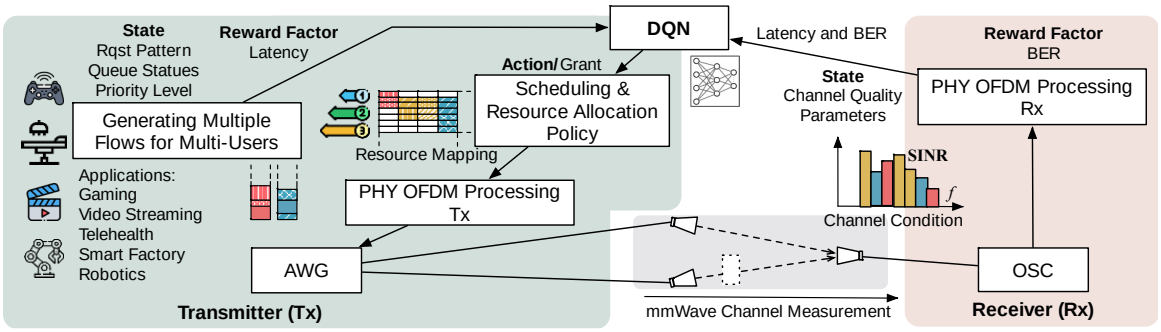


Figure 4.4 The modules and processing architecture of the mmWave RAN testbed with DRL-based scheduler.

Table 4-1 Delay components

| | | |
|---|---|---|
| Propagation Delay | 70.86μs | b, d, g, i, k |
| UE Processing | 0.32ms | a, e, j |
| Scheduler Processing | 62.98μs (14 sym.) | c |
| Re-tran Procssing | 0.21ms | h |
| Queuing Delay | Traffic-based | f |

In the system, the flow generation module will generate packets based on different application types. The DRL agent will make the action decision provided with the state information from the flow generation module and the mmWave channel module. In this work, mmWave channel information is obtained through experimental measurement of multi-user mmWave-RoF testbed instead of channel simulation. The mmWave channel

module consists of PHY OFDM processing module in the transmitter and receiver side (Tx and Rx). An AWG and a real-time oscilloscope are used in the experiment to generate analog OFDM waveforms and to capture the received waveforms for channel information extraction. The detailed implementation of each module will be illustrated in the following subsections.

#### 4.2.2.1 Flow Generation Module

The DRL system involves multiple users that are using applications with different QoS requirements. One UE can have multiple active flows simultaneously. For the flows implemented in the system, the packet arrival pattern, QoS priority, delay budget, and other key flow-specific parameters are summarized in Table 4-2. There are four types of flows in the system. The priority indicators listed in Table 4-2 are based on 3GPP QoS specification [79]. A service with smaller priority value has higher priority in the scheduling process. The priority value is a component ($s_{f,3}$) of the DRL state input. Among the applications, the flow for robotics control (*f1*) has critical latency requirement (1ms) and high data rate [70]; the flow for conventional video streaming or Web file transfer protocol (FTP) transmission (*f2*) can tolerate more latency; the flow for serious gaming or smart factory application (*f3*) also has critical latency requirement but can be supported

Table 4-2 Flow parameters

| Service Type | Priority | UE | Pkt Size | Pkt Interval | Speed (Mbps) | Delay Bdgt. |
|---|---|---|---|---|---|---|
| Robotics | 30 | 1(*f*1) | Rand | Cont. | 300-350 | 1ms |
| Video Streaming | 56 | 1(*f*2) | Log Norm. | Poisson | 10 | 5ms |
| Gaming/Factory | 30 | 2(*f*3) | Gaussian | Fixed | 3 | 1ms |
| Health Care | 56 | 2(*f*4) | Poisson | Cont. | 300 | 2ms |

with moderate data rate; the flow for tele-health (*f4*) such as tele-diagnosis and surgery may require latency on the order of 1-10ms with data rate around 100Mbps [70].

Different statistical models are employed for packet sizes and arrival intervals to mimic flow behaviors in reality. For time-sensitive traffic such as robotic control, the packet arrival processes follow *Bernoulli* processes [80]. In the DRL system, the probability of packet arrival is 0.8 for each TTI at the data rate of randomly generated 300-350Mbps to simulate control signaling. The video streaming is abstracted from FTP models with the file size using Log-normal variable ($\mu = 11, \sigma = 0.1$, leading to an average file size of 0.1Mb) [7].The FTP file arrival interval follows *Poisson* distribution with $\lambda = 100$ and packets are generated from each file accordingly. Flows following live streaming video model can cause significant queuing delay in upstream transmissions due to the influx of FTP file packets. For real-time gaming flows or smart factory signaling, normally distributed packet arrival intervals ($\mu = 320\mu s, \sigma = 65\mu s$) and normally distributed packet sizes ($\mu = 110b, \sigma = 40b$) are implemented [7]. The packets of real-time gaming usually have small packet sizes and sparse arrival intervals. To model tele-health traffic, the packet size follows *Poisson* distribution at the rate of 300Mpbs and packets will occur at every TTI.

#### 4.2.2.2 Scheduling and Resource Allocation Policies

The action of the DRL-based scheduler is to select the optimal resource allocation rule for the current TTI. The candidate rules are summarized in Table 4-3. Different rules have different scheduling objectives [81], [82]. In Table 4-3, the first rule targets to maximize the signal to interference and noise ratio (SINR) based on UE channel conditions. The proportional fair (PF) rule considers the trade-off between fairness and spectral efficiency, and it is aware of the channel condition and transmission history of

UEs. The exponential (EXP) rule uses an exponential function to take into account channel condition, spectral efficiency, HoL latency, and QoS requirements. Similarly, the LOG rule utilizes a logarithmic function to evaluate these factors. In both EXP and LOG rules, flows are prioritized when their HoL delays are approaching the delay deadline. The implementation details can be found [82]. In the proposed DRL algorithm, the action at each TTI is optimized with respect to different traffic and channel conditions. For example, max-SINR rule may be favored over LOG rule when the channel condition suddenly deteriorates.

Table 4-3 Resource allocation rules (action space)

| Rule | Feature | Objective |
|---|---|---|
| Max-SINR | Channel | Best BER |
| Propotional Fair (PF) | Channel & Speed Aware | Fairness & Throughput |
| LOG Rule (LOG) | Channel-Speed-Delay Aware | Fairness & Bounded Delay |
| Exponential Rule (EXP) | Channel-Speed-Delay Aware | Fairness & Bounded Delay |

#### 4.2.2.3 Experimentally Verified mmWave Channels

The experimental testbed setup to obtain the mmWave channel information is depicted in Figure 4.5, in which two UEs are accessing one RRU through RoF-mmWave uplinks consisting of 1m wireless link and 15km SMF. Due to the devices available in the lab, there are two UEs and four flows tested in the system without loss of generality. In reality, more UEs can be implemented when needed. The UE-flow mapping is indicated in Table 4-1. For each UE, the EVM of each RB will be measured and converted to SINR as channel quality parameter for the scheduling processing [83]. For more efficient processing, RBs are grouped to a RG when being allocated. Subcarriers and symbols in one RG have the same QAM modulation. The OFDM numerology and frame design are

based on 3GPP 5G specification [84]. The OFDM and RG numerology are summarized in Table 4-4.

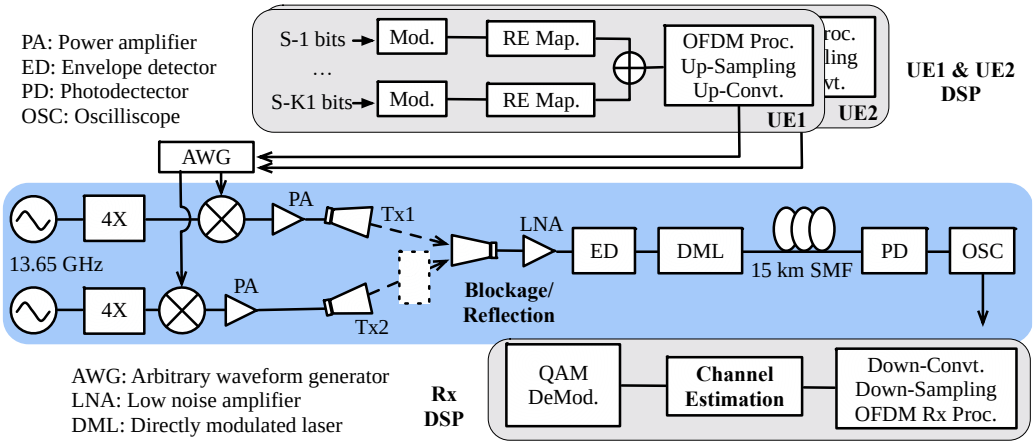


Figure 4.5 Experimental testbed for mmWave channel measurement. © OSA 2021.

Table 4-4 OFDM and RG numerologies

| Numerology, $\mu$ | 4 | TTI duration | 35.4μs |
|---|---|---|---|
| Subcarrier spacing | 240kHz | RB size | 12 subcarriers |
| Effective number of subcarriers | 840 (/2048) | RG size in frequency | 5RB/60 subarriers |
| Effective bandwidth | 201.6MHz | RG size in time | 2 symbol duration |
| Number of symbols per TTI | 8 | Modulation | QPSK/16QAM |

In the experiment, the operating mmWave frequency is 54GHz, generated by quadrupled 13.65GHz RF sources. OFDM waveforms synthesized by the AWG will be modulated to the mmWave carriers through electrical mixers. The mmWave signals are then amplified and radiated by horn antennas. At the receiver side, a horn antenna will capture the signals, followed by an envelope detector that down-converts the signal to baseband. For RoF mobile fronthaul transmission, the signal is converted to the optical domain through a direct modulated laser (DML) and converted back to the electrical domain by PD after fiber transmission. Finally, the received signal will be collected by an oscilloscope for DSP.

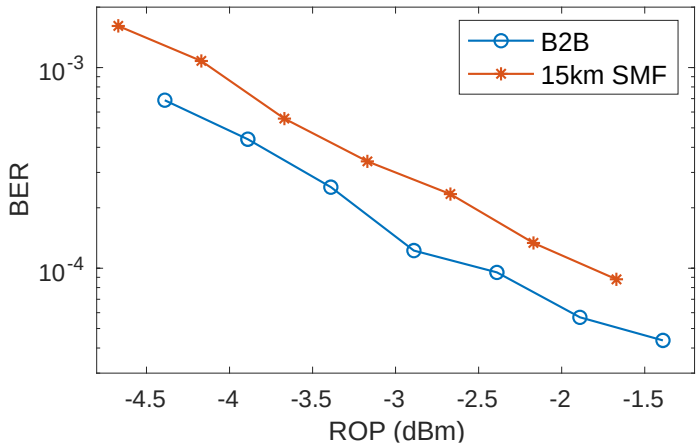


Figure 4.6 BER performance versus ROP in B2B and fiber transmission scenarios. © OSA 2021.

The BER versus ROP performance of the testbed is shown in Figure 4.6. For the channel measurement, the testbed is set at the optimal operating condition in which ROP = -1.5dBm. To realize the dynamic channel conditions of mmWave links such as reflection, blockage, and reduced transmission power, channel variation is introduced for UE2. The channel of UE2 is measured with three conditions: i) LoS link; ii) the link is 1/4 blocked (slightly blocked); iii) the link is 1/2 blocked (severely blocked), while UE1 always has an LoS link. The experimentally obtained channel SINR is shown in Figure 4.7, which is calculated from experimentally obtained EVM [83]. In the scheduling process, each channel condition will last for 50 TTIs and randomly switch to the next condition. Different channel conditions and rule selection will lead to different flow BER performance. Upon decoding the received signals, the scheduler will check the packet BER per flow. If the BER exceeds the pre-set threshold $ET_f$ (in this paper, $ET_f = 6.9 \times 10^{-4}, \forall f$, considering forward error correction [85]), re-transmission will be triggered and the overall packet latency will hence become longer.

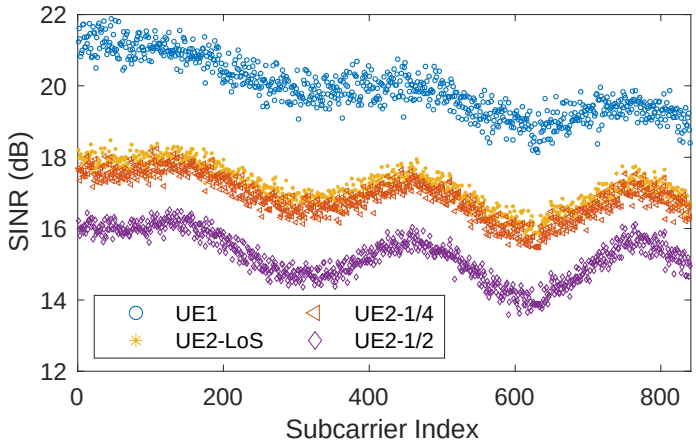


Figure 4.7 SINR per subcarrier of both UEs using 16QAM in different scenarios. © OSA 2021.

### *4.2.3 Evaluation and Discussion*

We create a DQN agent with recurrent neural network (RNN). There are three hidden layers between the input layer and the output layer: two dense layers and one long short-term memory (LSTM) layer, which have 30, 20, 16 neurons, respectively. The hyper-parameters of the DQN are summarized in Table 4-5. The convergence plot of the training process is presented in Figure 4.8. It can be seen that after around 600-episode training, the reward starts to converge. The fluctuation of the converged reward is caused by the randomness of the traffic patterns as indicated in Table 4-2 Flow parameters. Generally, the maximum average reward (1000) per episode can be achieved if the traffic load is light. However, in that case the DRL agent can randomly choose any action to fulfill the latency requirements. Therefore, the traffic load in the paper is set to a heavier case to exploit the advantages of DRL.

Table 4-5 DRL hyper-parameters

| | | | |
|---|---|---|---|
| Number of episodes | 1000 | Experience replay length | $10^6$ |
| Number of steps per episode | 1000 | Discount factor | 0.99 |
| Batch size | 64 | $\epsilon$ decay $d$ | $10^{-4}$ |
| Sequence length | 20 | Learning rate | $10^{-4}$ |

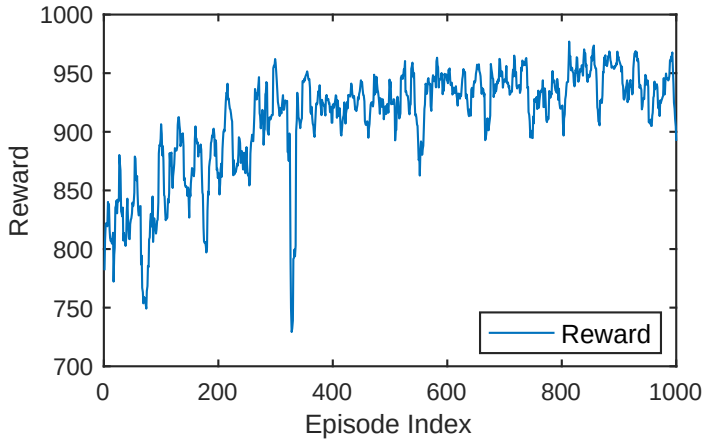


Figure 4.8 Reward convergence of the training process. © OSA 2021.

We define a test run as the scheduling over 1000 TTIs with randomly generated request patterns based on Table 4-2. The DRL agent is tested for 100 test runs, and the performance is evaluated and compared to the four single-target resource allocation rules listed in Table 4-3. The case of randomly selecting rules TTI-by-TTI is also presented as a reference ('Rand'). A higher reward value indicates lower percentages of latency-failure packets, as indicated in Equation (35). Figure 4.9 presents the average reward of 100 test runs using different scheduling and resource allocation schemes. It can be seen that the proposed DRL algorithm can achieve an average reward of $r$ = 0.91. If we assume all the packets as from an effective 'flow', the effective number of packets $\bar{M}$ and $\bar{L}$ can be used to calculate reward as $r \equiv 1 - \frac{\bar{L}}{\bar{M}}$, and the effective ratio of latency-satisfied packets will be $\frac{M}{\bar{N}} = \frac{M}{\bar{L}+\bar{M}} = \frac{1}{\frac{\bar{L}}{\bar{M}}+1} = \frac{1}{(1-0.91)+1} = 92\%$. However, among single-rule cases, LOG rule can achieve the best reward of 0.81. The proposed DRL algorithm can achieve 12%

average reward improvement in comparison. Figure 4.9 shows the number of times for each scheme to achieve the highest reward. Compared to other single-target schemes, the proposed DRL algorithm predominantly achieves the highest reward for 93 times out of 100 test runs.

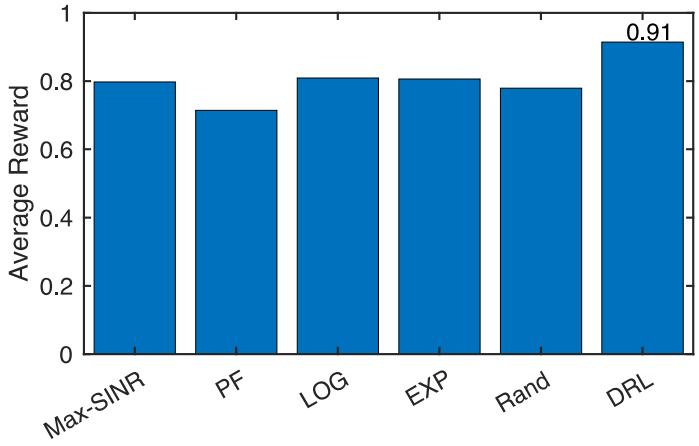


Figure 4.9 Average reward of 100 test runs for different rules.

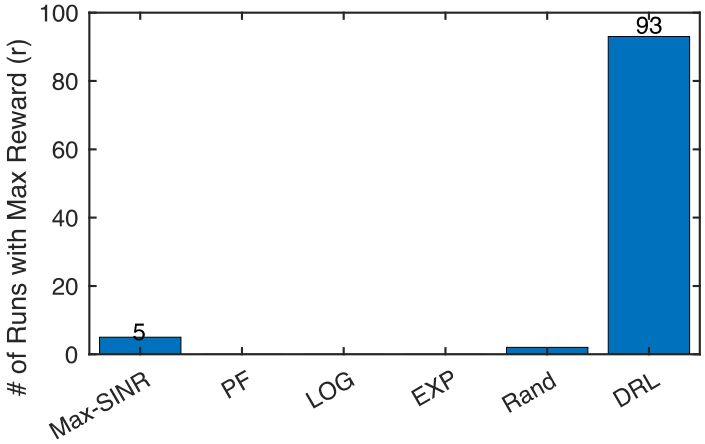


Figure 4.10 The number of times to achieve the maximum reward per rule.

We also investigate the BER and latency performance of the DRL-based scheduling. We select one test from the 100 test runs for result visualization. Figure 4.11 shows the average BER of all packets for each resource allocation scheme, the proposed DRL scheme can achieve the second best BER performance, only worse than the max-SINR scheme

whose target is to minimize BER. Figure 4.12 shows the ratio of QoS latency-satisfied packets per flow $\frac{M_f}{N_f}$ for all schemes. Compared to latency-aware LOG and EXP rules, the DRL algorithm is able to improve $\frac{M_f}{N_f}$ of *f3* and *f4* (from UE2 with channel variation, for UE-flow mapping, see Table 4-2), without sacrificing the performance of *f1* and *f2* (from UE1 with stable LoS links). Overall, the proposed DRL algorithm can jointly optimize BER and latency performance.

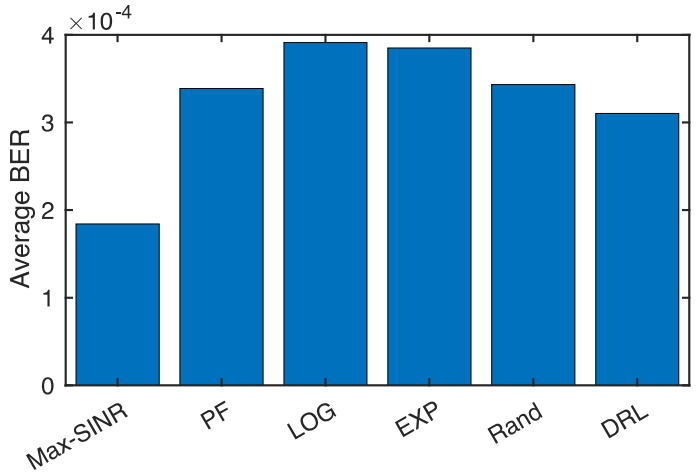


Figure 4.11 Average BER of each rule.

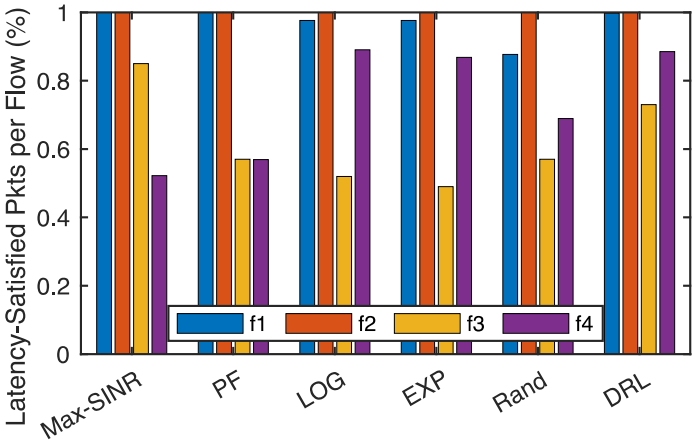


Figure 4.12 $\frac{M_f}{N_f}$ per flow for different rules.

Figure 4.13 presents the rule selection per TTI with respect to the channel variation of UE2. The blue curve indicates the SINR fluctuation of UE2, from which it is shown that each channel state lasts for 50 TTIs. As the rule selection can be jointly affected by the channel variations and flow request patterns, it can be seen that the pattern of rule selection synchronizes well with the channel SINR variation. The results show that the DRL system can react adaptively with channel condition variations.

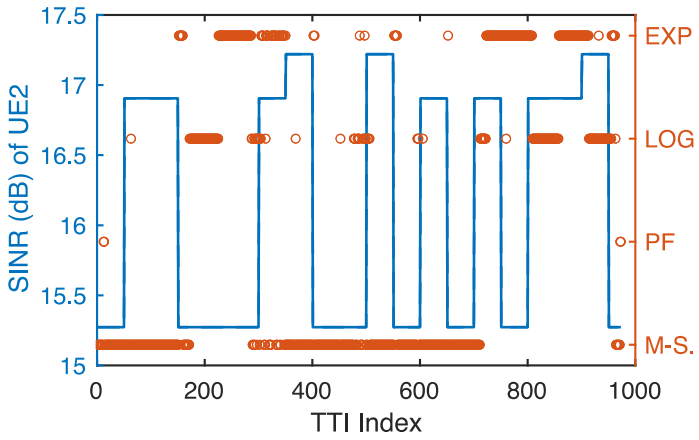


Figure 4.13 UE2 SINR variation and the corresponding rule selection per TTI. © OSA 2021.

### *4.2.4 Summary*

A DRL-based scheduler operating with both latency and channel condition awareness is proposed and verified for service-oriented multi-user mmWave RANs. The operation of the DRL scheduler is verified with experimental validation of mmWave-RoF channel conditions and variations, as well as various service flows with different QoS requirements. Among all the test runs, the DRL algorithm predominantly achieves the highest reward, providing at least 12% average reward improvement compared to other single-target schemes. Results also show that the proposed DRL system can operate adaptively with channel variations and jointly optimize BER and latency performance simultaneously. The

proposed DRL system has been demonstrated as a promising AI/ML-based technique that is applicable to post-5G RANs.

# CHAPTER 5 CONCLUSIONS

## 5.1 Technical Contributions

This dissertation studies and demonstrates the RoF-based access technologies to improve the performance of fiber-wireless networks, including multiplexing schemes to establish wireless overlay over fixed access networks for fixed-mobile convergence, advanced waveforms and access schemes for enhancement in the PHY layer, as well as DRL-based intelligent scheduling across PHY and MAC layers for latency and reliability improvements. The technical contributions of each research thrust are summarized.

### *5.1.1 RoF-Supported Wireless Overlay over Fixed Access Networks*

In the study of RoF-supported wireless overlay over fixed access networks, two schemes based on photonic-assisted mmWave generation techniques are proposed and demonstrated. The schemes fall into the category of fixed-mobile convergence, which aims to utilize the existing fiber resources of fixed access networks to provide next-generation mobile services. The two schemes exploit resource dimensions that were previously left unused to provide wireless overlay: one scheme is to utilize the idle LO laser via FDM, the other scheme utilizes the additional orthogonal optical polarization, achieving tracking-free PDM.

In the work of data-carrying remote LO, we have theoretically analyzed that there is the inherent frequency difference between the IM-DD architecture widely used for fixed access networks, which operates in the baseband, and the PH-based architecture for photonic-assisted mmWave generation, which operates in the mmWave bands. We develop

the method to modulate baseband data to the originally idle remote LO in a photonic-assisted mmWave generation setup so that co-transmission of mmWave wireless signals and baseband digital signals can be achieved requiring no extra devices. The system is experimentally demonstrated to support the co-delivery of a high-speed W-band OFDM signal and a baseband OOK signal. The interference performance of the system is also analyzed theoretically and experimentally, showing low sensitivity penalty caused by the interference and the tolerance of optical power fluctuation.

In the work of polarization-tracking-free PDM, we propose and demonstrate a PDM scheme to achieve the co-delivery of digital and analog signals for fixed and wireless RoF services, respectively. This is achieved by removing the unwanted optical carrier in each polarization, therefore the proposed system can resolve the polarization-tracking issue in conventional PDM. In comparison with regular non-PDM systems, the additional devices needed to implement the proposed PDM system are mainly passive devices, yet successfully bypassing the complicated polarization-tracking DSP. These devices are added in the central office and remote nodes requiring no changes in the fiber access networks, avoiding the high cost to pull extra fiber. The interference control due to the guard band setting as well as the crosstalk investigation is also analyzed theoretically and experimentally, showing low crosstalk between two polarizations and stable operation of the co-transmission system. We show that the proposed PDM system is spectrum-efficient and WDM-compatible.

In both works, we demonstrate co-delivery of fixed and mobile services using the proposed architectures with minimum alterations to the existing fiber networks. Comprehensive interference analysis is also studied theoretically and experimentally. Both

schemes can provide potential solutions for enhancing fiber and spectrum utilization, to achieve fixed-mobile convergence.

### *5.1.2 Advanced Access Technologies for Performance Optimization*

Windowed OFDM and PDMA, two OFDM-based access schemes are investigated in response to challenges in both radio and fixed access networks such as carrier aggregation, interference control, spectral efficiency, and advanced decoding algorithms, etc.

In the work of windowed OFDM, we accomplish the comprehensive study of windowed OFDM in both radio and fiber access networks. Theoretically and experimentally, windowed OFDM is quantitatively compared with other OFDM-based advanced waveforms in terms of spectral efficiency, DSP complexity, and CFO resistance. We show that windowed OFDM can improve spectral efficiency and CFO resistance through the analysis of the DFT filtering effect in the OFDM DSP. Windowed OFDM is demonstrated and evaluated in both V-band wireless access and long-range optical transmission. We show that windowed OFDM can provide suppressed out-of-band leakage and improved CFO-resistance by applying low-complexity short perfect reconstruction windows, enabling spectrum-efficient carrier-aggregation.

We also investigate PDMA in a mmWave radio access system with systematic experimental demonstration. The mathematical basics of PDMA and MPA algorithm to enhance the decoding performance are presented. A modified MPA algorithm is developed for better convergence efficiency. A PDMA system integrated with MPA is experimentally demonstrated in a multi-user mmWave radio access system that uses RoF mobile fronthaul, showing improved decoding performance compared to conventional PD-NOMA with SIC.

The applications of PDMA in the system are also experimentally evaluated. It is verified that PDMA can provide configuration flexibility, by evaluating the performance of PDMA with different pattern matrices and channel qualities. Furthermore, the ability of PDMA to support grant-free uplinks has been experimentally demonstrated, providing reduced BER penalty at the receiver compared to PD-NOMA using SIC. It is also verified that PDMA is capable of providing higher modulation spectral efficiency when part of the users in the system are subject to low-SNR channel qualities. We show that PDMA integrated with MPA has the potential to support future-proof mmWave-based radio access networks.

### *5.1.3 DRL-Based Scheduling Optimization of mmWave RAN*

A DRL-based scheduler operating with both latency and channel condition awareness is proposed and verified for service-oriented multi-user mmWave RANs. The main contributions of the work are summarized as follows:

1) We establish a DRL framework for joint BER and latency optimization for time-sensitive traffic in a service-oriented 5G system subject to dynamic mmWave channel conditions. Different statistical models are implemented for the arrival intervals and packet sizes of diverse applications. Conventional request-grant cycles of the uplink scheduling are implemented, considering possible congestion and queuing delay under heavy traffic load. In addition, we design and formulate the state and reward of the DRL scheduler such that it will reflect queue status, channel variation, and service-customized latency performance based on 3GPP QoS requirements.
2) In many previous research works, direct RB allocation mapping to UE is implemented as DRL actions. Through the investigation, we find that such straightforward action

design can cause extreme complexity and require huge computational resources if used in a multi-user wideband mmWave RAN. Therefore, we re-design the action of the DRL system to accelerate convergence.

3) In contrast to most of the previous DRL-related works with only simulation results, the mmWave channel characteristics utilized in the proposed system are experimentally collected and verified via a mmWave testbed with RoF-enabled mobile fronthaul. In this work, wide-bandwidth transmission and experimentally verified channel variations are achieved. To realize the dynamic channel conditions of mmWave links such as reflection, blockage, and reduced transmission power, channel variations are introduced in the scheduling process.

Results also show that the proposed DRL system can operate adaptively with channel variations and jointly optimize BER and latency performance simultaneously. The proposed DRL system can provide a promising AI-based technique that are applicable to post-5G RANs.

## 5.2 Future Research Topics

We have proposed RoF-based wireless overlay over fixed networks to support fixed-mobile convergence. Another way to tackle this task is to directly use fixed access networks to serve as the mobile x-haul. The advantage of the method is that we can use the existing network setting and it requires no architecture re-design. The challenge exists in the interface design between the radio and fixed access networks, especially in the scheduling latency and compatibility. Previous research includes low-latency DOCSIS and PON [5], [86]. Particularly, modified scheduling strategies are intensively investigated to improve

the interface efficiency and latency performance [5], [87], and [88]. Exploring the efficient ways to directly utilize fixed access networks as mobile x-haul will be an important task of fixed-mobile convergence, complementing the study of RoF-based wireless overlay over fixed access networks.

In the work of PDMA, we introduce the concept of PIC, which has better decoding accuracy compared to SIC used in conventional NOMA schemes. Interference cancellation is an important issue not only in NOMA, but also in a broader horizon wherever there is interference or resource duplexing. In the dissertation, we implement MPA to achieve PIC. Considering the powerful capability of AI and ML technologies, realizing PIC using AI or ML is a promising research direction, especially when the systems are subject to complex issues such as nonlinearity mitigation and self-interference cancellation.

The work of DRL-based intelligent scheduling establishes a basic DRL framework prototype for joint BER and latency optimization for time-sensitive traffic in a service-oriented 5G system. The framework can be improved in several aspects. The number of users and services involved in the system can be increased. The scheduling complexity is dependent on the number of active users. To design and evaluate a system that can support a large number of users will be challenging yet highly desirable, in which advanced and efficient computation architecture design is required. The reward of the DRL scheduler proposed in our work is designed such that it reflects the queue status, channel variation, and service-customized latency performance. With increasingly diversified and customized QoS requirements of various applications, the reward design should be updated as well. The reward design is a challenging task and would require extensive investigation, to reflect the QoS requirements and for the intelligent decision network to be responsive to

the reward changes. The most challenging task of intelligent scheduling is to set up a real-time testbed with hardware implementation of the system, especially the intelligent scheduler. It will be a good future topic to establish a real-time platform employing advanced intelligent scheduling schemes, so that performance indicators such as end-to-end latency, congestion performance, reliability, computing efficiency can be evaluated for real-world implementation.

# REFERENCES


[1] C. E. Shannon, “A mathematical theory of communication,” *The Bell System Technical Journal*, vol. 27, no. 3, pp. 379–423, 1948.

[2] A. G. Bell, “Improvement in telegraphy,” U.S. Patent 174465, Mar. 7, 1876. [Online]. Available: https://www.google.com/patents/US174465.

[3] Cisco, “Cisco Visual Networking Index: Forecast and Trends, 2017–2022,” Cisco, 2018. [Online]. Available: https://networking.report/Resources/Whitepapers/08d1985b-0247-42f2-ab7f-2c3e6e322821white-paper-c11-741490.pdf

[4] The COMBO project. “Deliverable D3.6: Final Architectural Recommendations for FMC Networks,” V1.0. Sept. 2016. [Online]. Available: http://www.ict-combo.eu/data/uploads/deliverables/combo_d3.6_wp3_30september2016_v1.0.pdf

[5] J. T. Chapman, J. Andreoli-Fang, M. Chauvin, E. C. Reyes, Z. Lu, D. Liu, J. Padden, and A. Bernstein, “Low latency techniques for mobile backhaul over docsis,” in *2018 IEEE Wireless Communications and Networking Conference (WCNC)*, 2018, pp. 1–6.

[6] 3GPP, “Study on Scenarios and Requirements for Next Generation Access Technologies,” 3GPP, TR 38.913, 2018, V15.0.0.

[7] G. White, K. Sundaresan, and B. Briscoe, "Low Latency DOCSIS: Technology Overview," CableLabs, DOCSIS Research and Development, Feb. 2019. [Online]. Available: https://www.cablelabs.com/technologies/low-latency-docsis.

[8] Y. Alfadhli, M. Xu, S. Liu, F. Lu, P.-C. Peng, and G.-K. Chang, "Real-Time Demonstration of Adaptive Functional Split in 5G Flexible Mobile Fronthaul Networks," in *Optical Fiber Communication Conference*. Optical Society of America, 2018. p. Th2A.48.

[9] Y. Cui, M. Zhang, D. Wang, S. Liu, Z. Li, and G.-K. Chang, "Bit-based support vector machine nonlinear detector for millimeter-wave radio-over-fiber mobile fronthaul systems," *Optical Express*, vol. 25, no. 21, pp. 26186-26197. Oct. 2017.

[10] S. Liu, M. Xu, J. Wang, F. Lu, W. Zhang, H. Tian, and G.-K. Chang "A Multilevel Artificial Neural Network Nonlinear Equalizer for Millimeter-Wave Mobile Fronthaul Systems," *Journal of Lightwave Technology*. vol. 35, no. 20, pp. 4406–4417, 2017.

[11] Q. Zhou, Y.-W. Chen, S. Shen, Y. Kong, M. Xu, J. Zhang, and G.-K. Chang, "Proactive Real-Time Interference Avoidance In a 5G Millimeter-Wave over Fiber Mobile Fronthaul Using SARSA Reinforcement Learning," *Optics Letters*., vol. 44, no. 17, pp. 4347–4350, Sept. 2019.

[12] T. Zhang, S. Shen, S. Mao and G. -K. Chang, "Delay-aware Cellular Traffic Scheduling with Deep Reinforcement Learning," in *GLOBECOM 2020 - 2020 IEEE Global Communications Conference*, Taipei, Taiwan, 2020, pp. 1-6.

[13] M. Feng and S. Mao, "Dealing with Limited Backhaul Capacity in Millimeter-Wave Systems: A Deep Reinforcement Learning Approach," *IEEE Communications Magazine*, vol. 57, no. 3, pp. 50-55, Mar. 2019.

[14] B. Zong, C. Fan, X. Wang, X. Duan, B. Wang and J. Wang, "6G Technologies: Key Drivers, Core Requirements, System Architectures, and Enabling Technologies," in *IEEE Vehicular Technology Magazine*, vol. 14, no. 3, pp. 18-27, Sept. 2019.

[15] G.-K. Chang and P.-C. Peng, "Grand challenges of fiber wireless convergence for 5G mobile data communications (Invited)," in *Proc. 23rd Opto-Electron. Commun. Conf. (OECC)*, Jul. 2018, p. 5A4-1.

[16] NGMN, "Overview on 5G RAN Functional Decomposition", Next Generation Mobile Networks (NGMN) Alliance, Feb. 2018, Version 1.0.

[17] ITU, "Setting the Scene for 5G: Opportunities and Challenges," International Telecommunication Union Radiocommunication Sector (ITU-R), 2018. [Online]. Available: http://handle.itu.int/11.1002/pub/811d7a5f-en

[18] CPRI Specification, "Common Public Radio Interface (CPRI); Interface Specification", Ericsson AB, Huawei Technologies Co. Ltd, NEC Corporation, Alcatel Lucent, and Nokia Networks, Interface specification, Oct. 2015, V7.0.

[19] 3GPP, "NR; User Equipment (UE) radio transmission and reception; Part 1: Range 1 Standalone," 3GPP, TS. 38.101-1, Apr. 2020, V16.3.0.

[20] 3GPP, "NR; User Equipment (UE) radio transmission and reception; Part 2: Range 2 Standalone," TS 38.101-2, Apr. 2020, V16.3.1.

[21] J. Wang, Z. Jia, L. A. Campos, L. Cheng, C. Knittle, and G. Chang, "Delta-Sigma Digitization and Optical Coherent Transmission of DOCSIS 3.1 Signals in Hybrid Fiber Coax Networks", *Journal of Lightwave Technology*, vol. 36, no. 2, pp. 568-579, 2018.

[22] Cable Labs, "Cable: 5G Wireless Enabler," CableLabs, Winter 2017. [Online]. Available: https://www.cablelabs.com/insights/cable-5g-wireless-enabler

[23] ITU-T, "5G wireless fronthaul requirements in a passive optical network context," Supplement 66 to ITU-T G-series Recommendations, Jul. 2019.

[24] X. Li, J. Yu, L. Zhao, K. Wang, C. Wang, M. Zhao, W. Zhou, and J. Xiao, "1-Tb/s millimeter-wave signal wireless delivery at D-band," *Journal of Lightwave Technology*, vol. 37, no. 1, pp. 196–204, Jan 2019.

[25] 3GPP, "Study on requirements for NR beyond 52.6 GHz," 3GPP, TR 38.807. Sept. 2019. V16.0.0.

[26] H. Zhang, Y. Dong, J. Cheng, M. J. Hossain, and V. C. M. Leung., "Fronthauling for 5G LTE-U Ultra Dense Cloud Small Cell Networks," *IEEE Wireless Communications*, vol. 23, no. 6, pp. 48-53, Dec 2016.

[27] X. Li, J. Yu and J. Xiao, "Demonstration of Ultra-Capacity Wireless Signal Delivery at W-Band," in Journal of Lightwave Technology, vol. 34, no. 1, pp. 180-187, 1 Jan.1, 2016.

[28] F. Lu, M. Xu, S. Shen, Y. M. Alfadhli, H. J. Cho and G. Chang, "Demonstration of Inter-Dimensional Adaptive Diversity Combining and Repetition Coding in Converged MMW/FSO Links for 5G and beyond Mobile Fronthaul," in *Optical Fiber Communication Conference*. Optical Society of America, 2018. p. M3K.4.

[29] F. Lu, L. Cheng, M. Xu, J. Wang, S. Shen and G. Chang, "Orthogonal and Sparse Chirp Division Multiplexing for MMW Fiber-Wireless Integrated Systems," in *IEEE Photonics Technology Letters*, vol. 29, no. 16, pp. 1316-1319, 15 Aug.15, 2017.

[30] X. Li, J. Yu, K. Wang, Y. Xu, L. Chen, L. Zhao, and W. Zhou, "Bidirectional delivery of 54-Gbps 8 QAM W-band signal and 32-Gbps 16 QAM K-band signal over 20-km SMF-28 and 2500-m wireless distance," in *Optical Fiber Communication Conference (Postdeadline Papers)*, Optical Society of America, 2017, p. Th5A.7.

[31] D. Zibar, R. Sambaraju, A. Caballero, J. Herrera, U. Westergren, A. Wal-ber, J. B. Jensen, J. Marti, and I. T. Monroy. "High-Capacity Wireless Signal Generation and Demodulation in 75- to 110-GHz Band Employing All-Optical OFDM," in *IEEE Photonics Technology Letters*, vol. 23, no. 12, pp. 810-812, Jun. 2011.

[32] CableLabs, "Data-over-Cable Service Interface Specifications (DOCSIS 3.1): Physical Layer Specification," Cable Television Laboratories, Inc. (CableLabs) Std., May 2017. CM-SP-PHYv3.1-I16-190121.

[33] D. Lopez-Perez, I. Guvenc, G. de la Roche, M. Kountouris, T. Q. S. Quek and J. Zhang, "Enhanced intercell interference coordination challenges in heterogeneous networks," in *IEEE Wireless Communications*, vol. 18, no. 3, pp. 22-30, June 2011.

[34] J. Zhang, J. S. Wey, J. Shi, J. Yu, Z. Tu, B. Yang, W. Yang, Y. Guo, X. Huang, and Z. Ma, "Experimental Demonstration of Unequally Spaced PAM-4 Signal to Improve Receiver Sensitivity for 50-Gbps PON with Power-Dependent Noise Distribution, " in *Optical Fiber Communication Conference*. Optical Society of America, 2018. p. M2B.3.

[35] J. Zhang, M. Xu, J. Wang, F. Lu, L. Cheng, H. Cho, K. Ying,J. Yu, and G.-K. Chang, "Full-Duplex Quasi-Gapless Carrier Aggregation Using FBMC in Centralized Radio-over-Fiber Heterogeneous Networks," in *Journal of Lightwave Technology*, vol. 35, no. 4, pp. 989-996, Feb 2017.

[36] S.-M. Kang, C.-H. Kim, and S.-K. Han, "Universal Filtered Multi-Carrier System for Asynchronous Uplink Transmission in Optical Access Network," in *Broadband Access Communication Technologies X*, B. B. Dingeland K. Tsukamoto, Eds., vol. 9772, International Society for Optic sand Photonics. SPIE, 2016, pp. 207 – 214.

[37] Qualcomm, “Making 5G NR a reality,” Qualcomm Technologies, White Paper, Sept. 2016. [Online]. Available: https://www.qualcomm.com/media/documents/files/whitepaper-making-5g-nr-a-reality.pdf

[38] F. Lu, M. Xu, L. Cheng, J. Wang, and G.-K. Chang, ”Power-Division Non-Orthogonal Multiple Access (NOMA) in Flexible Optical Access With Synchronized Downlink/Asynchronous Uplink,” in *Journal of Lightwave Technology*, vol. 35, no. 19, pp. 4145-4152, Oct 2017.

[39] Y. Saito, Y. Kishiyama, A. Benjebbour, T. Nakamura, A. Li and K. Higuchi, "Non-Orthogonal Multiple Access (NOMA) for Cellular Future Radio Access," *2013 IEEE 77th Vehicular Technology Conference (VTC Spring)*, Dresden, Germany, 2013, pp. 1-5.

[40] LG Electronics, “Initial LLS evaluation for NCMA,” 3GPP, TDocs (written contributions), R1-1804576, 2018.

[41] F. Lu, M. Xu, L. Cheng, J. Wang, J. Zhang and G. Chang, "Non-Orthogonal Multiple Access with Successive Interference Cancellation in Millimeter-Wave Radio-Over-Fiber Systems," in *Journal of Lightwave Technology*, vol. 34, no. 17, pp. 4179-4186, Sept 2016.

[42] S. Chen, B. Ren, Q. Gao, S. Kang, S. Sun and K. Niu, "Pattern Division Multiple Access—A Novel Nonorthogonal Multiple Access for Fifth-Generation Radio Networks," in IEEE Transactions on Vehicular Technology, vol. 66, no. 4, pp. 3185-3196, April 2017.

[43] 3GPP, “Study on Non-Orthogonal Multiple Access (NOMA) for NR,” 3GPP, TR 38.812, Dec 2018. V16.0.0.

[44] Huawei, HiSilicon, “Discussion on the design of NoMA receiver,” 3GPP, TDocs (written contributions) R1-1808386, Aug. 2018. TSG RAN WG1.

[45] Y. Alfadhli, S. Yao, M. S. Omar, S. Su, S. Shen, R. Zhang, Y. Chen, P. Peng, and G. Chang, "Design of Flexible Fronthaul Featuring Per-UE Granularity and RU-level Puncturing for URLLC Applications," in *Optical Fiber Communication Conference*. Optical Society of America, 2020. p. T4A.3.

[46] 3GPP, "NR Physical channels and modulation.," 3GPP, TS 38.211., 2020, V.16.2.0.

[47] M. Xu, X. Liu, N. Chand, F. Effenberger, and G. Chang, "Flex-Frame Timing-Critical Passive Optical Networks for Delay Sensitive Mobile and Fixed Access Services," in *Optical Fiber Communication Conference*. Optical Society of America, 2017. p. Th4B.6.

[48] Q. Zhou, J. Zhu, J. Zhang, Z. Jia, B. Huberman and G. -K. Chang, "Intelligent Bandwidth Allocation for Latency Management in NG-EPON using Reinforcement Learning Method," *2020 Conference on Lasers and Electro-Optics (CLEO)*, San Jose, CA, USA, 2020, pp. 1-2.

[49] Jun Shan Wey, "The Outlook for PON Standardization: A Tutorial," in *Journal of Lightwave Technology*, vol. 38, no. 1, pp. 31-42, Jan 2020.

[50] S. Shen, Q. Zhou, Y. Chen, S. Yao, R. Zhang, Y. Alfadhli, S. Su,J. Finkelstein, and G. Chang, "Hybrid W-Band/Baseband Transmission for Fixed-Mobile Convergence Supported by Heterodyne Detection with Data-Carrying Local Oscillator," in *Optical Fiber Communication Conference*. Optical Society of America, 2020. p. M2H.6.

[51] G.-K. Chang and L. Cheng, "The benefits of convergence," Phil. Trans. R. Soc., A 374: 20140442, Jan. 2016. [Online]. Available: http://dx.doi.org/10.1098/rsta. 2014.0442

[52] S. Gosselin, A. Pizzinat, X. Grall, D. Breuer, E. Bogenfeld, S. Krauß,J. A. T. Gij´on, A. Hamidian, N. Fonseca, and B. Skubic, "Fixed and Mobile Convergence: Which Role for Optical Networks?" *Journal of Optical Communications and Networking*, vol. 7, no. 11, pp. 1075-1083, Nov. 2015.

[53] S. Shen, J. Yan, P. Peng, C. Hsu, Q. Zhou, S. Liu, S. Yao, R. Zhang,K. Feng, J. Finkelstein, and G. Chang, "Polarization-Tracking-Free PDM Supporting Hybrid Digital-Analog Transport for Fixed-Mobile Systems," in *IEEE Photonics Technology Letters*, vol. 31, no. 1, pp. 54-57, Jan. 2019.

[54] R. Matsumoto, T. Kodama, S. Shimizu, R. Nomura, K. Omichi,N. Wada, and K.-I. Kitayama, "40G-OCDMA-PON System With an Asymmetric Structure Using a Single Multi-Port and Sampled SSFBG Encoder/Decoders," *Journal of Lightwave Technology*, vol. 32, no. 6, pp. 1132-1143, Mar. 2014.

[55] F. Lu, L. Cheng, M. Zhu, J. Wang, M. Xu, X. Ma, and G. Chang,, "Generalized Frequency Division Multiplexing for Photonic-Assisted Millimeter-Wave Carrier Aggregation," in *Optical Fiber Communication Conference*. Optical Society of America, 2015, p. M3E.3.

[56] S. Shen, T. Kanesan, P. Peng, F. Lu, M. Xu, S. Liu, C. Hsu, Q. Zhou, Y. M. Alfadhli, H. J. Cho, S. M. Mitani, J. Finkelstein, and G. Chang, "Spectrum-efficient 50-Gbps Long-Range Optical Access over 85-km SSMF via DML Using Windowed OFDM Supporting Quasi-Gapless Asynchronous Multiband Transmission," in *Optical Fiber Communication Conference*. Optical Society of America, 2018. p. M2B.5.

[57] S. Shen, T. Kanesan, F. Lu, M. Xu, L. Cheng, J. Wang, Y. M. Alfadhli, H. J. Cho, S. M. Mitani, and G. Chang, "Efficient Mobile Fronthaul Using Windowed OFDM Exhibiting High CFO Tolerance and Strong OOB-leakage Suppression with Low DSP Complexity," in *Optical Fiber Communication Conference*. Optical Society of America, 2018. p. Th3G.7.

[58] T. Kanesan, S. T. Le, D. Roque, and A. D. Ellis, "Non-rectangular perfect reconstruction pulse shaping based ICI reduction in CO-OFDM," *Optics Express*, vol. 22, no. 2, pp. 1749-1759, Jan. 2014.

[59] D. Pinchon and P. Siohan, "Closed-Form Expressions of Optimal Short PR FMT Prototype Filters," *2011 IEEE Global Telecommunications Conference - GLOBECOM 2011*, Houston, TX, USA, 2011, pp. 1-5.

[60] L. Tao, J. Yu, J. Zhang, Y. Shao and N. Chi, "Reduction of Intercarrier Interference Based on Window Shaping in OFDM RoF Systems," in *IEEE Photonics Technology Letters*, vol. 25, no. 9, pp. 851-854, May 2013.

[61] J. Zhang, J. Yu, F. Li, N. Chi, Z. Dong, and X. L, "11 x 5 x 9.3Gb/s WDM-CAP-PON based on optical single-side band multi-level multi-band carrier-less amplitude and phase modulation with direct detection," *Optics Express*, vol. 21, no. 16, pp. 18842-18848, Aug 2013.

[62] S. Shen, Y. -W. Chen, Q. Zhou, J. Finkelstein and G. -K. Chang, "Demonstration of Pattern Division Multiple Access With Message Passing Algorithm for Multi-

Channel mmWave Uplinks via RoF Mobile Fronthaul," in *Journal of Lightwave Technology*, vol. 38, no. 21, pp. 5908-5915, Nov 2020.

[63] L. Liu, E. G. Larsson, W. Yu, P. Popovski, C. Stefanovic, and E. de Carvalho, “Sparse signal processing for grant-free massive connectivity: A future paradigm for random access protocols in the internet of things,” *IEEE Signal Processing Magazine*, vol. 35, no. 5, pp. 88–99, 2018.

[64] Q. Zhou, S. Yao, S. Shen, Y. Chen, J. He, and G. Chang, “Efficient power-division NOMA for intelligent optical access network enabled by deep learning,” *Proc. IEEE Photon. Soc. Summer Topical Meeting Ser. (SUM)*, 2019, pp. 1–2.

[65] X. Dai, Z. Zhang, B. Bai, S. Chen, and S. Sun, “Pattern division multiple access: A new multiple access technology for 5G,” in *Proc. IEEE Wireless Commun.*, vol. 25, no. 2, pp. 54–60, 2018

[66] Y. Alfadhli, Y.-W. Chen, S. Liu, S. Shen, S. Yao, D. Guidotti, S. Mitani, and G.-K. Chang, “Latency performance analysis of low layers function split for URLLC applications in 5G networks,” *Computer Networks*, vol. 162, Art. no. 106865, 2019.

[67] C. Wei, H. Liu, Z. Zhang, J. Dang, and L. Wu, “Approximate message passing-based joint user activity and data detection for NOMA,” *in IEEE Communications Letters*, vol. 21, no. 3, pp. 640-643, Mar. 2017.

[68] B. Wang, L. Dai, Y. Zhang, T. Mir and J. Li, "Dynamic Compressive Sensing-Based Multi-User Detection for Uplink Grant-Free NOMA," in *IEEE Communications Letters*, vol. 20, no. 11, pp. 2320-2323, Nov. 2016.

[69] R. Hoshyar, F. P. Wathan and R. Tafazolli, "Novel Low-Density Signature for Synchronous CDMA Systems Over AWGN Channel," in *IEEE Transactions on Signal Processing*, vol. 56, no. 4, pp. 1616-1626, Apr. 2008.

[70] I. Parvez, A. Rahmati, I. Guvenc, A. I. Sarwat and H. Dai, "A Survey on Low Latency Towards 5G: RAN, Core Network and Caching Solutions," in *IEEE Communications Surveys & Tutorials*, vol. 20, no. 4, pp. 3098-3130, Fourthquarter 2018.

[71] Q. Hu, Y. Liu, Y. Yan, and D. M. Blough, "End-to-end Simulation of mmWave Out-of-band Backhaul Networks in ns-3." in *Proceedings of the 2019 Workshop on Next-Generation Wireless with ns-3 (WNGW 2019)*. Association for Computing Machinery, pp. 1–4.

[72] R. Zhang, F. Lu, M. Xu, S. Liu, P. Peng, S. Shen, J. He, H. J. Cho, Q. Zhou, S. Yao, and G. Chang, "An Ultra-Reliable MMW/FSO A-RoF System Based on Coordinated Mapping and Combining Technique for 5G and Beyond Mobile Fronthaul," *Journal of Lightwave Technology*, vol. 36,no. 20, pp. 4952–4959, 2018.

[73] M. Feng and S. Mao, "Dealing with Limited Backhaul Capacity in Millimeter-Wave Systems: A Deep Reinforcement Learning Approach," in *IEEE Communications Magazine*, vol. 57, no. 3, pp. 50-55, Mar. 2019.

[74] D. Han, W. Chen and Y. Fang, "Joint Channel and Queue Aware Scheduling for Latency Sensitive Mobile Edge Computing With Power Constraints," in *IEEE Transactions on Wireless Communications*, vol. 19, no. 6, pp. 3938-3951, June 2020.

[75] S. Tseng, Z. Liu, Y. Chou and C. Huang, "Radio Resource Scheduling for 5G NR via Deep Deterministic Policy Gradient," *2019 IEEE International Conference on Communications Workshops (ICC Workshops)*, Shanghai, China, 2019, pp. 1-6.

[76] S. Shen, T. Zhang, S. Mao, and G.-K. Chang, "DRL-Based Channel and Latency Aware Scheduling and Resource Allocation for Multi-User Millimeter-Wave RAN in *Optical Fiber Communication Conference*. Optical Society of America, 2021. p. F4I.3.

[77] Komic, J. "Harmonic Mean," In *Lovric M. (eds) International Encyclopedia of Statistical Science*. Springer, Berlin, Heidelberg. 2011. pp. 622-624.

[78] E. Dahlman, et al., (Ericsson), "Scheduling," in *5G NR: the next generation wireless access technology*, 1st ed., Academic Press, 2018, pp. 275-299.

[79] 3GPP, "System Architecture for the 5G System (5GS)," 3GPP, TS 23.501., 2019, V16.2.0.

[80] 3GPP, “Study on scenarios and requirements for next generation access technologies,” 3GPP, TR 38.913, 2017, v14.2.0.

[81] F. Capozzi, G. Piro, L. A. Grieco, G. Boggia and P. Camarda, "Downlink Packet Scheduling in LTE Cellular Networks: Key Design Issues and a Survey," in *IEEE Communications Surveys & Tutorials*, vol. 15, no. 2, pp. 678-700, Second Quarter 2013.

[82] A.Ahmad, M. T. Beg and S. N. Ahmad, "Resource allocation algorithms in LTE: A comparative analysis," *2015 Annual IEEE India Conference (INDICON)*, New Delhi, India, 2015, pp. 1-6.

[83] R. A. Shafik, M. S. Rahman, and A. R. Islam, “On the Extended Relationships Among EVM, BER and SNR as Performance Metrics,” in *2006 International Conference on Electrical and Computer Engineering*, 2006, pp. 408–411.

[84] 3GPP, "NR Physical channels and modulation.," 3GPP, TS 38.211., 2020, V.16.2.0.

[85] Juniper, "Forward Error Correction (FEC) and Bit Error Rate (BER),", Juniper, Dec. 2020. [Online]. Available: https://www.juniper.net/documentation/en_US/junos/topics/topic-map/fec-ber-otn-interfaces.html

[86] S. Bidkar, J. Galaro and T. Pfeiffer, "First Demonstration of an Ultra-Low-Latency Fronthaul Transport Over a Commercial TDM-PON Platform," in *Optical Fiber Communication Conference*. Optical Society of America, 2018. p. Tu2K.3.

[87] S. Zhou, X. Liu, F. Effenberger, and J. Chao, “Low-Latency High-Efficiency Mobile Fronthaul with TDM-PON (Mobile-PON),” *Journal of Optical Communications and Networking*, vol. 10, no. 1, pp. A20–A26, Jan 2018.

[88] T. Tashiro, S. Kuwano, J. Terada, T. Kawamura, N. Tanaka, S. Shigematsu, and N. Yoshimoto, "A novel DBA scheme for TDM-PON based mobile fronthaul," in *Optical Fiber Communication Conference*. Optical Society of America, 2014. p. Tu3F.3.

# VITA

Shuyi Shen was born in 1992 in Liancheng, Fujian province, China. She received B.S. degree in Electrical and Electronics Engineering from the School of Electronic Information and Electrical Engineering, Shanghai Jiao Tong University, Shanghai, China, in 2015. Currently, she is working toward her Ph.D. degree at the School of Electrical and Computer Engineering of Georgia Institute of Technology, Atlanta, GA, USA.

She joined Georgia Tech since fall 2015 and has worked on several projects for the National Science Foundation (NSF) Center on Fiber-Wireless Integration and Networking (FiWIN). In 2018, she was an engineer intern at CableLabs, Louisville, CO; in 2019, she was a product research and development intern at Semtech Corporation, San Jose, CA. Her research mainly focuses on the system design and signal processing techniques for resource allocation and performance optimization in fiber-wireless access networks.

She has authored and co-authored more than 50 peer-reviewed journal articles and international conference papers. She also serves as an active reviewer for IEEE Access, IEEE Communications Magazine, Journal of Lightwave Technology, Photonics Technology Letters, Photonics Journal, Optics Express, Optical Engineering, and IEEE Vehicular Technology Conference.